12-2018

Experimentation and Modeling of the Effects of Along-Wind Dispersion on Cloud Characteristics of Finite-Duration Contaminant Releases in the Atmosphere

Jessica M. Morris
University of Arkansas, Fayetteville

Recommended Citation

Morris, Jessica M., "Experimentation and Modeling of the Effects of Along-Wind Dispersion on Cloud Characteristics of Finite-Duration Contaminant Releases in the Atmosphere" (2018). *Theses and Dissertations*. 3088.
https://scholarworks.uark.edu/etd/3088

Experimentation and Modeling of the Effects of Along-Wind Dispersion on Cloud Characteristics of Finite-Duration Contaminant Releases in the Atmosphere

A dissertation submitted in partial fulfillment
of the requirements for the degree of
Doctor of Philosophy in Chemical Engineering

by

Jessica M. Morris
University of Minnesota
Bachelor of Science in Chemical Engineering, 2014

December 2018
University of Arkansas

This dissertation is approved for recommendation to the Graduate Council

Tom O. Spicer III, Ph.D., P.E.
Dissertation Director

Jerry Havens, Ph.D. Committee Member	Heather Walker, Ph.D. Committee Member
Larry Roe, Ph.D. Committee Member	David Ford, Ph.D. Committee Member

Abstract

Along-wind dispersion, or stretching of the cloud in the direction of the wind, plays an important role in the concentration and modeling of contaminant releases in the atmosphere. Theoretical and empirical derivations were compared for appropriate parameterization of along-wind dispersion. Available field data were analyzed to evaluate and improve previous parameterizations of the along-wind dispersion coefficient, σ_x. An experimental test program was developed and executed in an ultra-low speed wind tunnel at the Chemical Hazards Research Center to determine the effects of the time distribution coefficient on true finite-duration releases from an original area source. Multiple wind speeds, release durations, and downwind distances were investigated with ensemble averages for improved quality of the cloud characteristics for each set of test conditions. An overall relationship between the time of peak arrival (TOPa) and the time distribution coefficient $\sigma_t = 0.23 * TOPa$ was demonstrated across all parameters. From this relationship, the along-wind dispersion coefficient can be accurately predicted and scaled appropriately. Additional relationships for the leading and trailing edges of the cloud are appropriately modeled.

Project Overview

Continued worldwide industrial development has brought the widespread use of industrial chemicals, many of which are hazardous. Whether released accidentally or intentionally, air born hazardous chemicals can affect large populations quickly as evidenced by several industrial chemical accidents (e.g., Bhopal[1], Flixborough[2], Seveso[3], etc.). Understanding and modeling hazardous chemical releases are vital to protecting the public. The ability to predict the potential impact of hazardous gas releases in the atmosphere is imperative to properly determine the transport, storage, and use of such chemicals. In the case of an actual loss of containment, understanding where air born chemicals can travel is important to determine the proper response to an emergency.

Researchers have worked to assess these hazards through instantaneous, continuous, and time-limiting experimental releases to develop computational models such as PHAST, HEGADAS, and SLAB. Although instantaneous and continuous models are sufficient for many release scenarios, many real-world problems involve finite-duration releases. Advanced computational fluid dynamics (CFD) models can theoretically handle these complexities, but these models still need data for validation and have the disadvantage of being relatively expensive and difficult to use on a daily basis. Simpler (screening) models are needed to determine which cases require more careful studies with CFD models.

At present, very few data sets (field or wind tunnel) exist to validate finite-duration dispersion models. Sheesley[4] and King[5] analyzed finite-duration releases performed at the Nevada Test Site. Finite-duration release data is needed for validation of current models. Large-scale field experimental programs are important for understanding the relevant physics but are very expensive. Wind tunnel experimental work fills an important role in providing data for validation at a reduced cost.

While models exist to address issues such as release duration or dispersion, established theories regarding along-wind dispersion often show results which are not realistic when compared with existing experimental data. It is crucial to develop experiments to improve models of finite-duration hazardous gas releases which illustrate the importance of the effects of along-wind dispersion, particularly the elongation of the cloud in the along-wind direction. Supported and validated by new wind tunnel experimental data, the development of models will lead to better assessment of the hazards that can accompany industrial development. Experimental data and improved models developed in this Ph.D. project will influence the way toxic and flammable gases are modeled in the future.

This research will provide needed experimental data on finite-duration releases to study the effects of along-wind dispersion to improve existing atmospheric dispersion modeling. Improved modeling of along-wind dispersion will be accomplished through the three main aims listed below.

Aim 1: Compare the theoretical basis for modeling of the effects of along-wind dispersion.

Aim 2: Analyze available field data to parameterize the along-wind dispersion coefficient. Available field data will be analyzed to determine an appropriate parameterization of along-wind dispersion.

Aim 3: Develop physical modeling of finite-duration releases. Experimental data will be planned and executed at an ultra-low speed wind tunnel facility to obtain finite-duration releases in a controlled environment.

Table of Contents

Introduction

Since the industrial revolution in the late 1700s, there has been an increased use of industrial chemicals. Many of these chemicals are toxic, flammable, or both. When stored or transported in large quantities, these hazardous chemicals can be dangerous if released into the atmosphere. The devastating effects of hazardous chemicals in the atmosphere is detrimental with Bhopal[1] in 1984 killing thousands of sleeping people from methyl isocyanate gas released in the middle of the night, the Flixborough accident[6] in 1974 killing dozens of workers and damaging more than 1,000 homes in the area after a reactor exploded, and Seveso[3] in 1976 with an accidental release of TCDD killing thousands of animals and exposing thousands of residents. Mitigating these negative effects through safe transportation, storage, and processing can prevent these catastrophic situations. While preventative management can suppress some accidents, no method can contain 100% of a containment in an accident. Therefore the modeling of these of air born chemicals when released is vital for appropriate emergency response methods.

Many researchers have spent their lives developing models to assess the impact of these hazardous releases in the atmosphere. Such numerical models like PHAST, HEGADAS, and SLAB are some of the leading computational tools used in industry and research today. Advanced computational fluid dynamic (CFD) models can predict atmospheric complexities at a more sophisticated level but are time-consuming and as only as good as the data they have for validation. Both numerical and CFD models require quality data for validation. Finite-duration releases are important due to the dispersion of the cloud falling in between an instantaneous and continuous release. These in-between durations increases complexities for appropriate modeling. Along-wind dispersion, the elongation of the cloud in the direction of the wind, has a major impact on finite-duration releases.

While along-wind dispersion is theoretically established by a handful of scientists and mathematicians, no overarching equation is well-accepted. Validation of theory with new wind tunnel experimental data will lead to better assessment of the hazards that can accompany industrial development through improved modeling of along-wind dispersion. Experimental data and improved models developed in this Ph.D. project will influence the way hazardous gases are modeled in the future.

Turbulence in the Atmosphere

Once contaminants are released into the atmosphere, contaminants are in the atmosphere. Unlike liquid chemicals on a lab bench that are spilled, additional chemicals cannot be added to the atmosphere to "neutralize" the negative effect of the chemical release. This inability to be neutralized or contained makes air born hazardous chemicals even more dangerous. The only way contaminants are reduced to non-hazardous levels in the atmosphere is through dilution. Dilution of contaminants in the atmosphere occurs through the mixing of contaminants with the surrounding air, decreasing the concentration of the hazardous material. This mixing occurs through turbulence. Turbulence is achieved in the atmosphere through objects in the flow, surface roughness, air entrainment, gravity stratification, wind speed, and stability classes. An example of a bluff body effect increasing the downwind mixing behind the body is shown below in Figure 1.

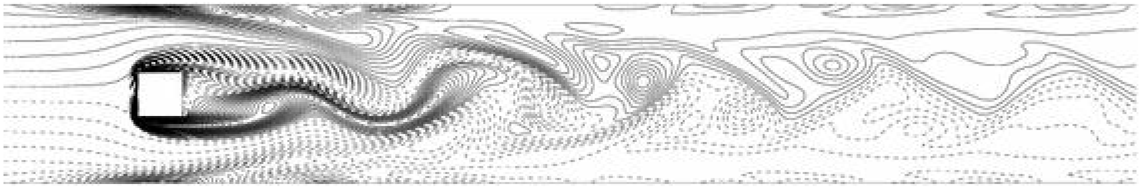

Figure 1. Increased turbulence is shown behind a bluff body in fluid flow[7], similar to the effects of surface roughness

One of the notable methods to increase turbulence in the atmosphere is through surface roughness. This method will be used and discussed in a later section related to turbulence achieved in the wind tunnel to simulate the atmospheric boundary layer.

Pasquill Stability Classes

There are two main ways to classify the mixing achieved in the atmosphere: Pasquill stability classes and Monin-Obukhov length. Pasquill stability classes are the most common method to classifying the atmosphere and is shown below in Figure 2.

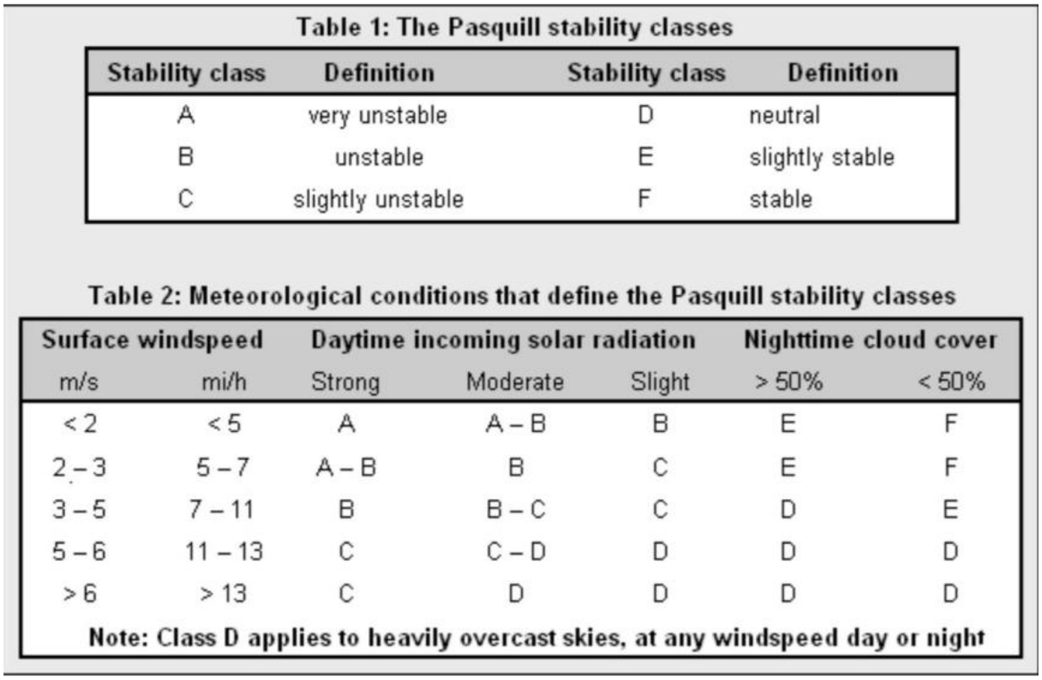

Table 1: The Pasquill stability classes

Stability class	Definition	Stability class	Definition
A	very unstable	D	neutral
B	unstable	E	slightly stable
C	slightly unstable	F	stable

Table 2: Meteorological conditions that define the Pasquill stability classes

Surface windspeed		Daytime incoming solar radiation			Nighttime cloud cover	
m/s	mi/h	Strong	Moderate	Slight	> 50%	< 50%
< 2	< 5	A	A – B	B	E	F
2 – 3	5 – 7	A – B	B	C	E	F
3 – 5	7 – 11	B	B – C	C	D	E
5 – 6	11 – 13	C	C – D	D	D	D
> 6	> 13	C	D	D	D	D

Note: Class D applies to heavily overcast skies, at any windspeed day or night

Figure 2. Pasuill Stability classes with the class (Table 1) and the Meteorological conditions for each class (Table 2)

Pasquill classifies the atmosphere into six stability classes shown above: A-C are unstable, D is neutral, and E-F (sometimes G) are stable. How these classes are quantified is shown at the bottom half of the figure due to wind speed and solar insolation, or radiation. When the sun is shining, it heats the earth. The earth will then heat the air above it increasing the mixing causing the atmosphere to be unstable. Mixing from heat dominates the turbulence compared to wind speed during the day making stability class A the most unstable due to greatest mixing. Stability class D occurs an hour before and after sunset and sunrise. Stability class D also occurs when there are overcast skies resulting in no solar insolation. Stable stability classes occur at night when there is no sun and decreased mixing. Stable conditions are the most dangerous for hazard chemicals due to the decrease of mixing and therefore decrease of dilution of hazardous chemicals into the atmosphere.

Where Pasquill classifies the atmosphere into six separate classes, more continuous methods are desired. This desire for a more continuous and accurate quantification of turbulence in the atmosphere is achieved through Monin-Obukhov Length. Determination of Monin-Obukhov length is shown below in equation (1)

$$\boldsymbol{\lambda = \frac{u_*{}^3\overline{\theta_v}}{kg(\overline{w'\theta_v{}'})_s}} \qquad \textbf{(1)}$$

where λ is the Monin-Obukhov length, u_* is the friction velocity, θ_v is the mean potential temperature of the air, k is the von Karman constant, g is gravity, and $(\overline{w'\theta_v{}'})_s$ is the temperature flux of the surface. This method provides a continuous numerical value in units of length (m) quantifying the turbulence and mixing in the atmosphere. Similar to Pasquill stability classes, the Monin-Obukhov length is able to classify neutral, stable, and unstable atmospheric conditions. $\lambda < 0$ quantifies unstable conditions occurring during the day, $\lambda > 0$ quantifies stable conditions occurring during the nighttime, and $\lambda = 0$ quantifies neutral conditions occurring during overcast and the hour before or after dusk and dawn.

Contaminant Releases in the Atmosphere

Contaminant releases into the atmosphere are commonly quantified into four types of releases based on their release duration and release rate: instantaneous, continuous, finite-duration, and time-varying. Once released into the atmosphere, the cloud will disperse in three directions (3D): vertical (z), crosswind (y), and along-wind (x). An example of the 3D dispersion from an elevated instantaneous release is shown below in Figure 3.

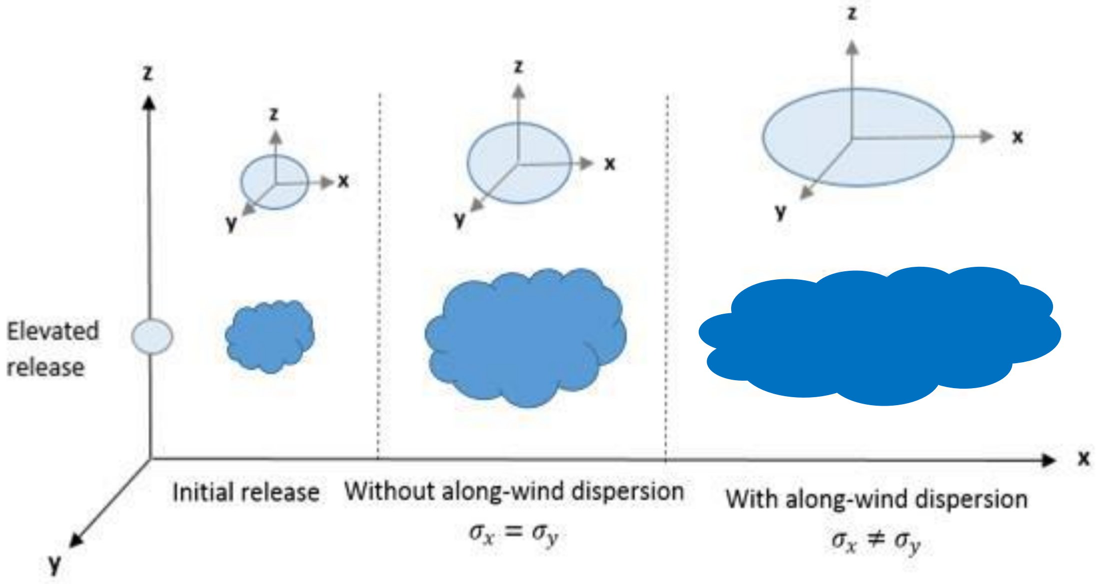

Figure 3. Cloud geometry for dispersion of an elevated instantaneous release with dispersion in all directions

The initial release (left) shows a spherical cloud simulating an elevated instantaneous release. The cloud disperses equally in the x-, y-, and z-directions upon initial release. In the following frames are 3D dispersion both with (right) and without (middle) along-wind dispersion. Dispersion in the vertical, σ_z, and crosswind, σ_y, directions have well-established and accepted relationships. Dispersion in the along-wind direction, σ_x, has no well-established or accepted relationship. A common assumption used in modeling is that the dispersion in the crosswind and along-wind direction are equivalent. This assumption is shown in the middle frame with $\sigma_x = \sigma_y$. While this creates a spherical cloud that is easy to model, this method is inaccurate. Realistically, along-wind dispersion should be taken into account due to the stretching of the cloud in the along-wind direction which can alter the predicted time of arrival and maximum concentration of hazardous materials in the atmosphere. The effects of along-wind dispersion are shown in the right-most frame of Figure 3.

Finite-Duration Releases

The duration of the release will impact the concentration measurements downwind. Concentration sensors placed downwind of a cloud release can measure concentration-time histories to determine the concentration as a function of time at the specified distance. For an instantaneous release, a puff will pass through a concentration sensor for a short period. When the center of the cloud is located over the concentration sensor, the maximum concentration is observed. The concentration will decrease to zero as the puff continues downwind from the sensor. For a continuous release, the plume will be stationed over the concentration sensor for a longer period of time due to the increased cloud duration. For a finite-duration release, it is believed that the leading and trailing edges of the cloud behave differently than either a puff (instantaneous release) or a plume (continuous release), and the concentration as a function of time is a combination of the two behaviors. Hypothetical leading and trailing edges are typically considered to have a Gaussian distribution. This Gaussian distribution is shown in Figure 4 with concentration-time histories.

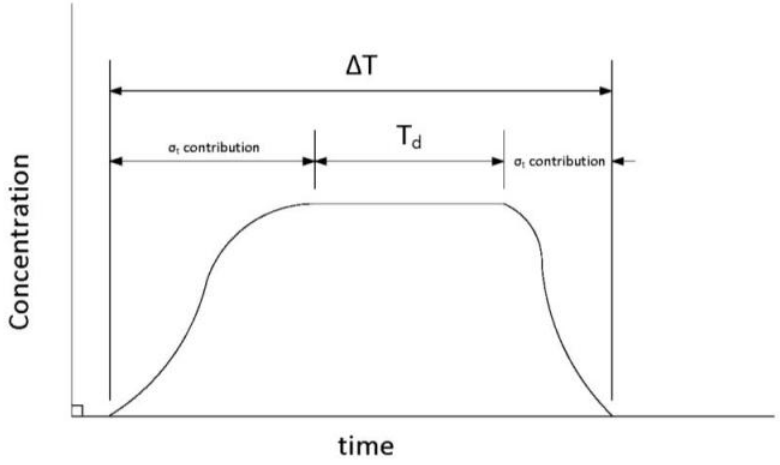

(a) Hypothetical concentration time history if concentration is uniform for T_d as analyzed by Hanna and Chang

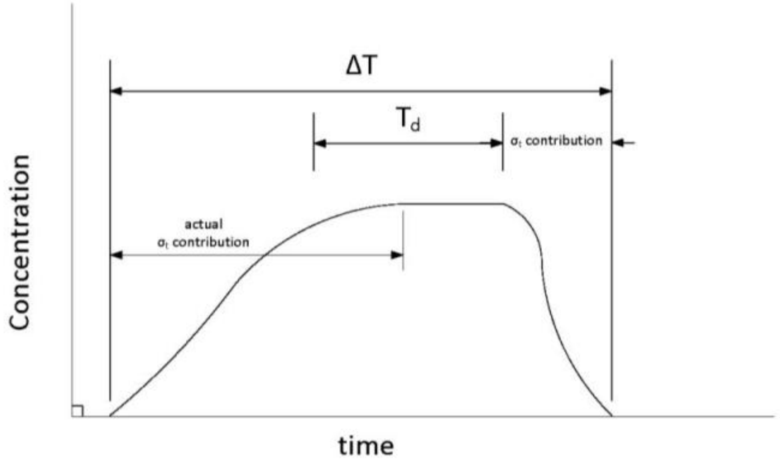

(b) Expected concentration time history if concentration is uniform for $t<T_d$.

Figure 4. Concentration-time histories of finite-duration releases showing the impact of σ_t[8]

The hypothetical concentration leading and trailing edges by Hanna are derived from the distribution coefficient, σ_t, total cloud duration, ΔT, and the release duration, T_d. The commonly used relationship to describe the time distribution coefficient is $\sigma_t = \frac{\Delta T - T_d}{4.3}$. This relationship gives the Gaussian distribution shown in Figure 4a with the leading and trailing edges being equivalent. Expected concentration- time histories by Petersen[9] show concentration-time histories for finite-duration releases in Figure 4b. The expected concentration-time histories show a larger impact of along-wind dispersion on the leading edge of the cloud and a decreased impact of along-wind dispersion on the trailing-edge of the cloud. This shows that σ_t is underrepresented from the previous Gaussian relationship in Figure 4a. True finite-duration releases will to be performed to determine adequate effects of along-wind dispersion and improve current models.

1 Theoretical Framework and Experimental Derivations

1.1 Introduction

Within the planetary boundary layer, shear caused by along-wind dispersion is much larger than directional shear. This along-wind dispersion causes clouds to elongate in the x-direction more so than the y- and z-directions. Along-wind dispersion is more complex than vertical and crosswind dispersion with the direct relationship between advection cloud speeds. Along-wind dispersion plays a crucial role in the leading edge of the cloud, where the contaminant in the cloud mixes with the uncontaminated fluid and determines the maximum concentration of a release. Along-wind dispersion can be measured by the along-wind dispersion coefficient, σ_x, which is the total variance of the concentration distribution in the direction of the wind.

The continuity equation can be applied to the dispersion of a cloud in the atmosphere. The cloud is assumed to be instantaneous and released at ground level, where z = 0. Turbulent transport is assumed to be described using eddy diffusivities: K_x, K_y, and K_z. Mean wind in the x- and y-directions are assumed to have horizontal axes and parallel to the ground with components U(z) and V(z) respectively. Under these assumptions, the continuity equation is obtained:

$$\frac{\partial c}{\partial t} + U\frac{\partial c}{\partial x} + V\frac{\partial c}{\partial y} = \frac{\partial}{\partial x}\left(K_x\frac{\partial c}{\partial x}\right) + \frac{\partial}{\partial y}\left(K_y\frac{\partial c}{\partial y}\right) + \frac{\partial}{\partial z}(K_z\frac{\partial c}{\partial z}) \qquad \textbf{(2)}$$

Integrated forms of this continuity equation can be solved using moments. Moments are calculated from the mass of the cloud. The zeroth moment is the total mass of the cloud, the first moment is the total mass at the center of mass in a specific direction, and the second moment is the rotational inertia. The integral for moments of concentration at height *z*, is shown below, as given by Saffman[12],

$$\boldsymbol{\theta_{nm}(z,t)} = \iint_{-\infty}^{\infty} \boldsymbol{x^n y^m\, c\, dx\, dy}, \quad (\boldsymbol{n \geq 0, m \geq 0}) \tag{3}$$

where c is the concentration of the diffusing material. Moments are able to describe the variance and cross-correlation of the mass of a cloud with respect to all directions. Equations solving for the dispersion of a cloud in a specific direction all apply the normalized concentration equation to a cloud given by Saffman[14] as

$$\int_0^h \theta_{00} dz = \int_{-\infty}^{\infty} \int_{-\infty}^{\infty} \int_0^h c\; dx\; dy\; dz = 1 \tag{4}$$

where $c\;dx\;dy\;dz$ is the probability of a marker fluid particle in the volume of size $dx\;dy\;dz$ surrounding (x,y,z) for time and θ_{00} is the average concentration over the plane of height z. The variance in the along-wind direction is shown below as

$$\sigma_x{}^2 = \frac{\theta_{20}}{\theta_{00}} - (\frac{\theta_{10}}{\theta_{00}})^2 \tag{5}$$

where θ_{20} is the second moment of c, θ_{10} is the first moment of c, and θ_{00} is the zeroth moment of c. Integrating the first moment with respect to the height from 0 to h, the height gives the x-coordinate of the centroid of all the mass as shown below.

$$\Theta_{10} = \int_0^h \theta_{10}\;\; dz. \tag{6}$$

$$\Theta_{20} = \int_0^h \theta_{20}\;\; dz \tag{7}$$

Combining these equation gives equation (8) when $\Theta_{00} = 1$.

$$\sigma_x{}^2 = \Theta_{20} - \Theta_{10}{}^2 \tag{8}$$

Equation (8) is a generalized mathematical equation for the expression of the variance in the along-wind direction. Along-wind dispersion has been shown to be affected by both the mean wind shear and turbulence in pipes by Taylor (1953)[10]. Csanady (1969)[11] extended this approach to dispersion in the atmosphere with the definitions of moments in the along-wind direction to get the overall relationship of:

$$\sigma_x{}^2 = \sigma_{xt}{}^2 + \sigma_{xs}{}^2 \qquad \textbf{(9)}$$

where σ_{xt} is the effect of turbulence, and σ_{xs} is the effect of wind shear in the vertical direction, similar to Saffman.

Although wind shear and turbulence have a large effect on along-wind dispersion, many other factors determine the overall along-wind dispersion coefficient. As a cloud is moving through the atmosphere, the effective wind speed can increase which causes the along-wind dispersion coefficient to increase. The function of velocity depends on the friction velocity, u_*, and the travel time, t. Height affects these statistical properties of motion. It is well known that wind speed increases as a function height. From this relationship, the advection velocity will be increased as the depth of the cloud increases. The release height and cloud centroid height have an effect on velocity due to this relationship. Many theoretical derivations for the along-wind dispersion coefficient make the assumption of the release height, *z*, being equal to 0 for simplification. Along with release height and stability class, surface roughness plays a large role in predicting the along-wind dispersion coefficient in an instantaneous passive release. This report presents the specific derivations for the along-wind dispersion coefficient as a function of different assumptions and conditions.

1.2 Theoretical Framework

The along-wind dispersion coefficient can be calculated under many different conditions and assumptions. The overarching relationship for the along-wind dispersion coefficient involves the effects of wind shear and turbulence shown above in equation (9) by Csanady[11]. This equation is generally accepted as the overarching relationship for the along-wind dispersion coefficient, as a function of the effects of wind shear and turbulence. Note that the effect of along-wind dispersion is most important for ground level releases which are the focus of this research.

Theoretical approaches for parameterizing along-wind dispersion by σ_x can be based on travel time t (as proposed by Chatwin and van Ulden) or travel distance x (as proposed by Wilson and Ermak). This distinction is important when implemented in a dispersion model. Of the time dependent functions, in neutral conditions, σ_x is shown as a function of t. The constant(s) in all derivations are dependent on the stability class used, how derivations are performed, and the assumptions that are made. The following subsections summarize the most prominent theoretical descriptions with their assumptions from Saffman, Batchelor, Chatwin, Csanady (above), Wilson, Ermak, and Van Ulden.

1.2.1 Saffman (1962)

The first effects of along-wind diffusion were seen in a pipe with the laminar flow of liquid as a result of velocity shear and lateral diffusion. This sparked the notion of diffusion in the along-wind direction in fluids by Taylor (1953)[10]. Along-wind diffusion was further analyzed by the idea of lateral transport described as eddy diffusivities. Qualitative results were obtained and had good agreement with experimental results under the assumptions of Reynold's analogy relating the eddy diffusivity and eddy viscosity[10]. While along-wind diffusion can be measured in a tube with finite boundaries, the atmosphere is considered an unbounded system with no finite height. Applying the previous theories to atmospheric dispersion is done under two conditions by Saffman (1962)[12] with a bounded and unbounded atmospheric boundary layer. Although an unbounded boundary layer, with the ability of a material to diffuse to any height, is more complicated, Saffman is able to solve for the along-wind dispersion coefficient in both bounded and unbounded boundary conditions using moments, discussed above. Since Saffman's bounded and unbounded derivations, all following derivations for the along-wind dispersion coefficient are performed with no restriction on the overall height. Expanding on the continuity equation with moments and eddy diffusivities under neutral conditions, ground release height and an unbounded boundary layer, the equation for along-wind dispersion derived by Saffman is

$$\boldsymbol{\sigma_x}^{\mathbf{2}} = \boldsymbol{\alpha^2 t^2 (k_z t)^{\frac{2a}{2-c}} f(\rho) + k_x t (k_z t)^{\frac{d}{2-c}} f(\rho)} \tag{10}$$

where $\alpha, a, b, c, k_x,$ and k_z are all constants, t is the travel time, and $f(\rho)$ is a function of ρ, where $\rho = z/(2Kt)$.

1.2.2 Batchelor (1964)

Batchelor (1964)[13] developed the Lagrangian Similarity Hypothesis. This hypothesis relates to Eulerian and Lagrangian quantities when deriving theoretical solutions based on established relationships. Applying known properties of fluid flow to the atmosphere, Batchelor was able to establish a generalized description of σ_x under neutral stability conditions, with no restraints on maximum height, for center line (maximum) concentration at ground level accounting for wind speed dependence with height. Batchelor derived one main relationship that serves as the foundation for modern theoretical approaches known as Batchelor's Lagrangian similarity theory. This relationship between turbulence in a constant stress region in a boundary layer is a function of the friction velocity, u_*, and time, t. This relationship is commonly seen in other author's derivations for along-wind dispersion.

1.2.3 Chatwin (1968)

Chatwin (1968)[14] was the first mathematician to theoretically derive a full equation with numerical values to predict the along-wind dispersion coefficient and shear stress contribution. Chatwin used Batchelor's Lagrangian similarity theory along with a description of atmospheric turbulence using an eddy diffusivity model to solve for σ_x. His solution is restricted to ground level releases in a neutral stability unbounded boundary layer. The generalized equations for the overall along-wind dispersion, σ_x , and wind shear, σ_{xs} , according to Chatwin are

$$\sigma_x = 0.803\frac{u_* t}{\kappa} \tag{11}$$

$$\sigma_{xs} = 0.596\frac{u_* t}{\kappa} \tag{12}$$

where u_* is the friction velocity, t is time, and κ is the van Karman's constant taken to be 0.41.

1.2.4 Wilson (1981)

Under the assumptions of a neutral stability class and an unbounded boundary layer, Wilson (1981)[15] made the distinction that the shear component dominates the majority of the equation. Under this distinction, the turbulence component can be estimated as

$$\sigma_{xt} \simeq \left(\frac{u'}{w'}\right)\sigma_z \tag{13}$$

with u' as the turbulent velocity in the x-direction, w' as the turbulent velocity in the z-direction, and σ_z as the vertical dispersion in meters. Using Smith's[16] equation for the wind shear,

$$\sigma_{xs}{}^2 = \frac{1}{12}\left(\frac{dU}{dz}\grave{t}\right)^2 \sigma_z{}^2 \tag{14}$$

where U is the wind speed, z is the height, and $\grave{t}$ is the travel time of an instantaneous puff (also given by x/U_c), Wilson derives the along-wind dispersion equation for both ground and elevated releases. For ground releases, the rate of change is dependent on the position of the puff centroid using the logarithmic velocity profile.

$$\frac{d\bar{x}}{d\grave{t}} = \frac{u_*}{\kappa}\ln(\frac{\bar{z}\exp(-0.577)}{z_o}) \tag{15}$$

where $\bar{z} = bu_*\grave{t}$ is the vertical height of the ensemble averaged centroid. Integrating from 0 to $\grave{t}$, and substituting different relationships into the turbulent shear equations, Wilson gets an along-wind dispersion coefficient for a ground release to be

$$\sigma_x = [0.09\left(\frac{x}{z_r\ln(z_c/z_o)}\right)^2 + \left(\frac{\sigma_{xt}}{\sigma_z}\right)^2]^{0.5}\sigma_z \tag{16}$$

with z_r as the reference height and z_c as the height where the wind speed equals the mean convection speed. For an elevated release, the power law profile applies.

$$\frac{U}{U_r} = (\frac{z}{z_r})^n \tag{17}$$

Where n is an empirically derived coefficient that is dependent on the stability class. Using the power law relationship, Wilson is able to derive an equation for the along-wind dispersion coefficient from an elevated release

$$\sigma_x = [0.09\left(\frac{nx}{z_r}(\frac{z_r}{z_c})^n\right)^2 + \left(\frac{\sigma_{xt}}{\sigma_z}\right)^2]^{0.5}\sigma_z \tag{18}$$

with $z_c = n + 0.17\sigma_z$. Wilson derives σ_x as a function of distance, where most derivations of σ_x are believed to be a function of time.

1.2.5 Ermak (1986)

Ermak (1986)[17] developed an algorithm to determine the center-line concentration at ground level for a finite-duration ground level release, as a function of distance. The along-wind dispersion coefficient calculated by Ermak uses a similar function to Csanady's incorporating σ_{xs} and σ_{xt}, but as a function of distance.

$$\sigma_x(x) = \sqrt{{\sigma_{xs}}^2(x) + {\sigma_{xt}}^2(x)} \tag{19}$$

The shear and turbulent components of the equation are solved for and substituted into equation (20). The equation for the shear component is given as

$$\sigma_{xs}(x) = a_{xs}x \, , with \; a_{xs} = 0.6 \, p \, [\frac{0.48}{\gamma}]^p \tag{20}$$

where $\boldsymbol{p}$ is a constant and $\boldsymbol{\gamma}$ is shown as

$$\gamma = \sqrt{2}\left[\frac{(1 - pd)\Gamma(\frac{1}{2}p + \frac{1}{2})}{\sqrt{\pi}}\right]^{1/p} \tag{21}$$

where $d = d_{sc} + d_{zo}$. Constants d_{sc} and d_{zo} are determined from stability class and surface roughness by McMullen. McMullen (1975)[18] developed an equation for the cross-wind dispersion coefficient which is used to describe the turbulence spread coefficient in the x-direction, $\sigma_{xt}(x)$,

$$\sigma_{xt}(x) = \sigma_{ya}(x) = \left(\frac{t_{av}}{600}\right)^{0.2} e^{I+J(\ln\left(\frac{x}{1000}\right)+K[\ln\left(\frac{x}{1000}\right)]^2}, \qquad x > L \tag{22}$$

$$\sigma_{ya}(x) = \frac{x}{L}\sigma_{ya}(L) \, , \qquad x < L$$

where x is distance, and I, J, K and L are all constants determined as a function of stability class.

1.2.6 Van Ulden (1992)

Van Ulden (1992)[19] derived an equation under slightly different conditions in comparison to Chatwin. Van Ulden made the distinction between absolute and relative dispersion. Chatwin was able to authenticate his equation with the assumption of a hypothetical atmosphere: where no large horizontal eddies exist. Taking into consideration this distinction between absolute and relative dispersion, van Ulden derived a new equation for σ_x, the total variance of the concentration distribution in the wind direction

$$\sigma_x{}^2 = \sigma_c{}^2 + \sigma_d{}^2 \tag{23}$$

where σ_c is the deterministic part (or centroid variance), and σ_d is the random part (or diffusive variance). The total longitudinal variance, σ_x, is dependent on three separate quantities: centroid variance, diffusive variance due to shear effects, and direct diffusion. These three variables are solved for shear, centroid, and diffusive effects respectively as a function of friction velocity and time.

$$\sigma_s = 0.5\frac{u_* t}{\kappa} \tag{24}$$

$$\sigma_c \simeq 0.54\frac{u_* t}{\kappa} \tag{25}$$

$$\sigma_d = 0.67\frac{u_* t}{\kappa}. \tag{26}$$

Under the assumption that $\sigma_c \simeq \sigma_s = 0.5\frac{u_* t}{\kappa}$, these variables can be substituted into equation (23) to get the total longitudinal variance. An exact equation for σ_x is obtained.

$$\sigma_x = 0.84\frac{u_* t}{\kappa} \tag{27}$$

In addition to an along-wind dispersion equation in neutral conditions, Van Ulden derived an along-wind dispersion equation for ground releases in an unbounded boundary layer for very stable conditions. Under very stable conditions, the wind speed profile and eddy diffusivities change. When applying the new constraints for wind speed and eddy diffusivities in a different stability class, the total variance of concentration distribution in the wind direction is shown to be:

$$\sigma_x = \{(\frac{3}{4} - \frac{16}{9\pi})\frac{5u_*{}^3 t^3}{k\boldsymbol{\lambda}}\}^{1/2} \simeq 0.43(\frac{5u_*{}^3 t^3}{k\boldsymbol{\lambda}})^{1/2}. \tag{28}$$

where λ is the Monin-Obukhov length reflecting the stability class.

1.2.7 Summary of Theoretical Framework

All theoretical framework is a function of the assumptions made during the derivations. The majority of the authors use neutral stability class and generalize the equations as functions of parameters with constants. The following chart summarized the prominent theoretical framework by what differentiates the author's derivation from other derivations for along-wind dispersion in chronological order.

Table 1. Summary of Theoretical Framework

Batchelor (1964)	• $\sigma_x = f\,(t, u_*)$ • Lagrangian Similarity Theory Solely a function of time and friction velocity
Chatwin (1968)	• $\sigma_x = 0.803\frac{u_* t}{\kappa}$ $\sigma_{xs} = 0.596\frac{u_* t}{\kappa}$ • Eddy diffusivity turbulence with respect to height
Csanady (1969)	• ${\sigma_x}^2 = {\sigma_{xt}}^2 + {\sigma_{xs}}^2$ • Independent variances can be added to get a total variance Along-wind dispersion is comprised of shear and turbulent components
Ermak (1986)	• ${\sigma_x}^2 = {\sigma_{xt}}^2 + {\sigma_{xs}}^2$ • Function of distance Turbulent and shear components determined mathematically
Van Ulden (1992)	• $\sigma_x = 0.84\frac{u_* t}{\kappa}$ $\sigma_x = 0.43\left(\frac{5{u_*}^3 t^3}{kL}\right)^{1/2}$ • Absolute and Relative Diffusion Take into account unstable atmospheric conditions

Not all derivations were included if the results were essentially equivalent. If two methods were similar in derivation and parameterization, the most inclusive method or method that occurred first was included in the chart. From the chart, the five key players are shown: Batchelor with $\sigma_x = f\,(t, u_*)$ and the Lagrangian Similarity theory, Chatwin with numerical derivations and σ_{xs}, Csanady with along-wind dispersion as a function of shear and turbulent components, Ermak with along-wind dispersion as a function of distance, and van Ulden taking into account stability classes.

1.3 Empirical Derivations

While there are many theoretical derivations for the along-wind dispersion coefficient, there are not many experimental data sets available. Data is critical for validating potential theoretical models. The experimental data that has been previously collected supports some theoretical derivations and provided new equations to fit data sets explicitly. The following sections describe previous experimental studies and their respective empirical derivations for along-wind dispersion.

1.3.1 Hanna and Franzese (1999)

Hanna and Franzese (1999)[20] used 12 experimental data sets to determine a generalized equation for along-wind dispersion. Starting with Csanady's overarching equation (9), Hanna and Franzese were able to solve for an overarching along-wind dispersion equation. Hanna and Franzese used the equations from Batchelor's Lagrangian similarity theory[13] and Smith's wind shear component[16] to determine relationships for the turbulence and shear components shown below.

$$\sigma_{xt} = A u_* t \tag{29}$$

$$\sigma_{xs} = B\left(\frac{1}{\sqrt{12}}\right)\sigma_z\left(\frac{du}{dz}\right)t \tag{30}$$

Both A and B are constants where $\frac{du}{dz}$ is the wind shear. They assumed that the wind shear and vertical dispersion are negatively correlated so that the shear component does not vary with stability class, which allows for the use of multiple stability classes in their validation. Hanna and Franzese related dispersion and wind shear proportionally to the friction velocity. Under these relationships, they determined a generic equation for along-wind dispersion as a function of friction velocity and time, with *D* as a constant seen below.

$$\sigma_x = Du_* t \tag{31}$$

Using the 12 data sets available, Hanna and Franzese found the constant, *D*, to equal 2. This constant is a fit for the available data sets which encompass all stability classes and release heights in an unbounded boundary layer as seen in Figure 5.

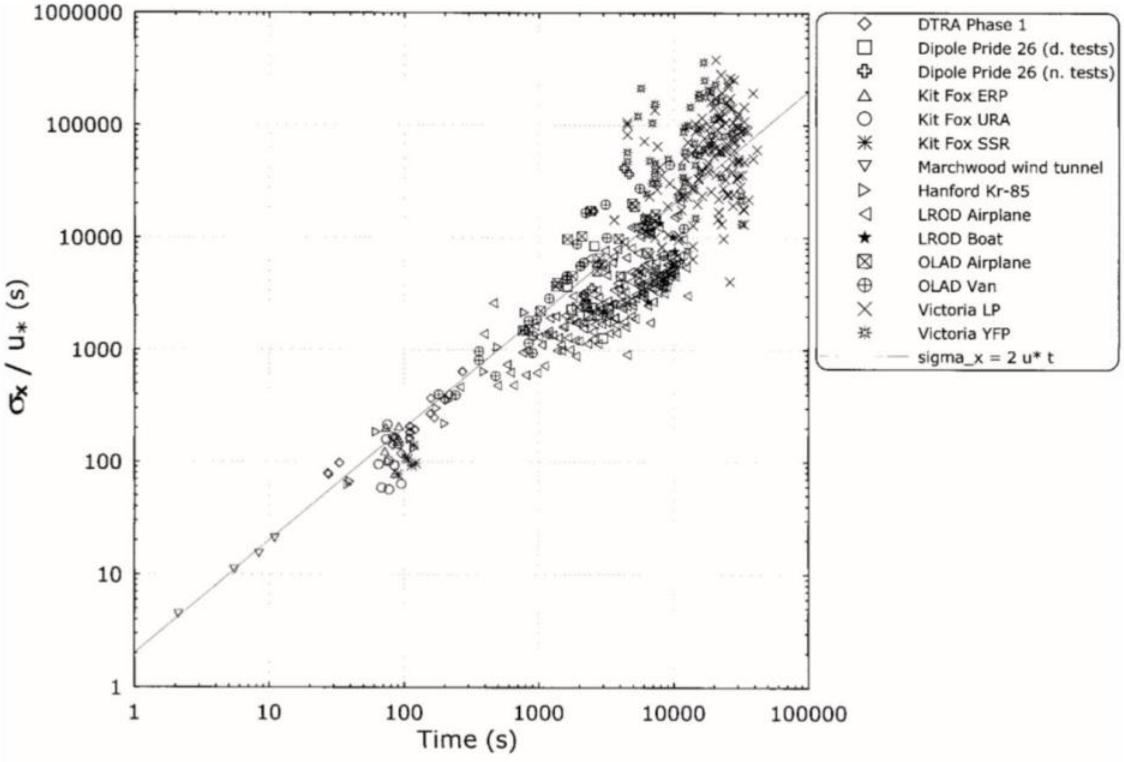

Figure 5. Hanna and Franzese results of the along-wind dispersion coefficient divided by friction velocity and plotted vs. time. Line represents $\sigma_x = 2u_*t$

Figure 5 shows an increasing trend when σ_x / u_* is plotted as a function of time. The data encompasses a wide range of stability classes which will be discussed in a later section. Wind shear is a function of height but is disregarded in the assumptions made by Hanna and Franzese. Here, all data points are weighted equally, however, in reality, some tests have more experimental trials than others. σ_x was solved from σ_t. Therefore, σ_x is a secondary variable, where it should be a primary variable. About 50% of the data is within a factor of 2 for the data shown in Figure 5. It should be noted that the plot is logarithmic which increases the variance between model and data.

1.3.2 Drivas (1974)

Drivas (1974)[21] used a smaller experimental data set to determine an equation for along-wind dispersion. His tests consisted of quasi-instantaneous crosswind line sources released at ground level in urban conditions. Concentration measurements were recorded at 0.4 km, 0.8 km, 1.6 km, 2.4 km, and 3.2 km downwind. The along-wind dispersion coefficient was plotted against time to determine the relationship between the variables. Examples of the plots are shown below in Figure 6.

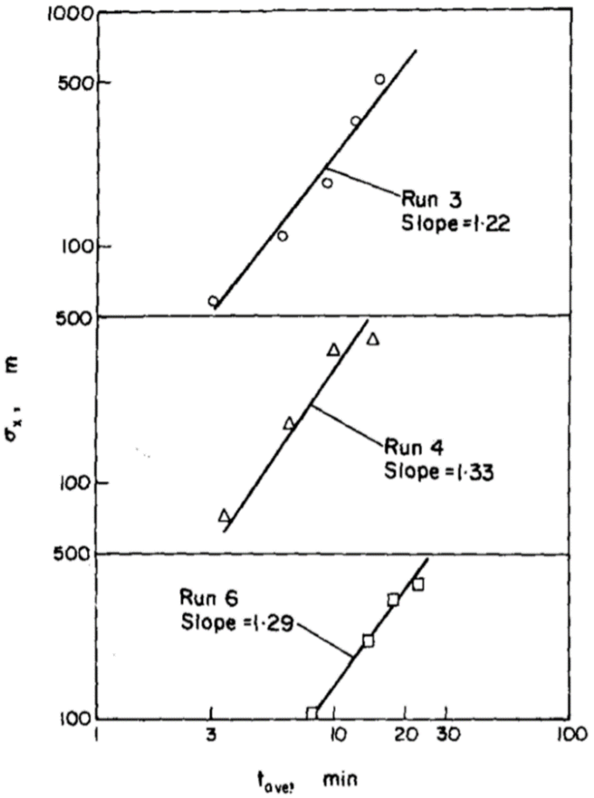

Figure 6. Linear-least square fit for runs, 3, 4, and 6 to show the along-wind horizontal standard deviation vs. the average time of the travel

From here, a relationship between the along-wind dispersion coefficient and time was developed as

$$\sigma_x = at^b \tag{32}$$

where a and b are constants. The constant, b, is determined to be a range from 1.11 – 1.47 depending on the stability class. The more stable the stability class, the greater the value of b is. The closer to neutral the stability class, the closer b is to 1 showing an impact of stability class on σ_x.

1.3.3 Draxler (1979)

Draxler (1979)[22] also used a smaller experimental data set to determine an along-wind dispersion coefficient from instantaneous line sources. He performed three trials in an unbounded atmosphere, with both elevated and ground level releases under several stability classes. Draxler used the formula from Smith and Hay (1961)[23] for the turbulent component of along-wind dispersion

$$\sigma_{xt} = 3i^2t \tag{33}$$

with i as the intensity of the turbulence shown as

$$i^2 = \langle u'^2 \rangle - \langle \bar{u} \rangle^2 \tag{34}$$

where u' is the turbulent velocity and $\bar{u}$ is the mean wind speed. Draxler used Saffman's[12] equation for wind shear in an unbounded boundary layer shown below

$$\sigma_{xs} = \frac{1}{\bar{u}}\sqrt{\frac{1}{25}\Psi^2 K_z t^3} \tag{35}$$

where Ψ is the slope of the wind speed profile and K_z is the vertical turbulent diffusivity. Draxler inserts these equations into equation (36) to get a growth relationship for σ_x shown as

$$\sigma_x \propto t^\alpha. \tag{36}$$

From experimental data, Draxler concluded that the exponent, α, is closer to 1 when dominated by turbulence and closer to 1.5 when dominated by wind shear. Draxler further shows the relationship between σ_x and σ_y shown in Figure 7.

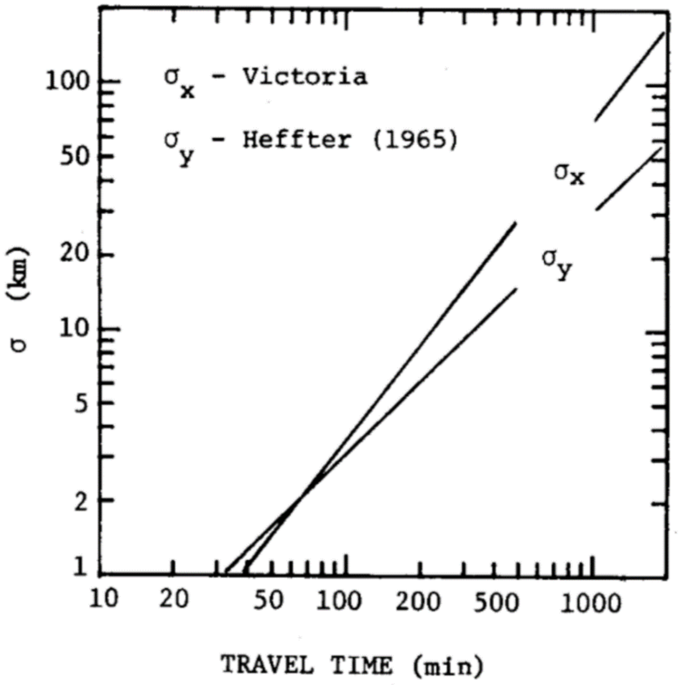

Figure 7. Plot of the along-wind dispersion from the Victoria experiments and cross-wind dispersion for large travel times from Heffter (1965)

Often, the along-wind and cross-wind dispersion are assumed equivalent in modeling. Draxler shows both the function of along-wind dispersion as an exponential of time and the inequivalent relationship between σ_x and σ_y. From experiments performed by Draxler, the $\sigma_x = \sigma_y$ relationship is the shown to be invalid.

1.3.4 Sato (1979)

Sato (1979)[24] performed an analytical study in Japan called the Short Range Diffusion Experiment Series (SRDES). A vacant lot surrounded by trees was used to determine the along-wind dispersion of NO_x released from a balloon 15-20 cm in diameter at an elevation of 1.5 m. The balloon contained 5-10% of NO_x with the remaining volume of inert N_2. Lines of gas samplers were located at distances of 60 m and 100 m downwind. The relationship between the along-wind dispersion coefficient and time for these tests are shown below in Figure 8.

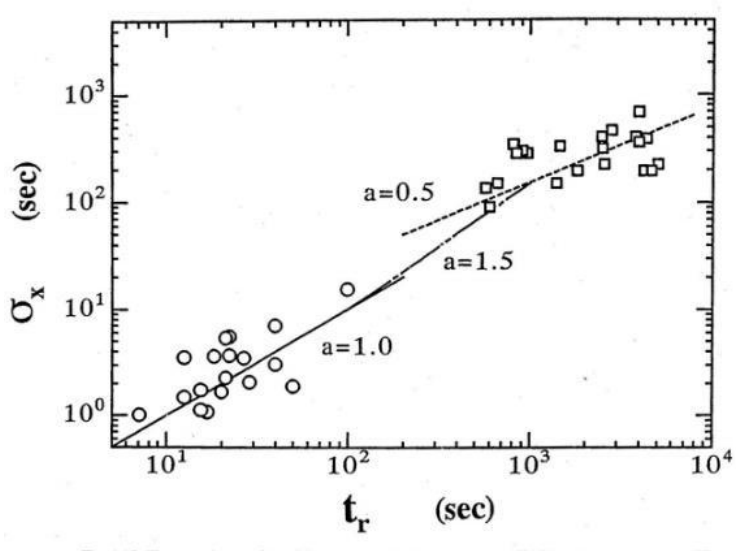

Figure 8. The plot of along-wind dispersion coefficients as a function of time (s)

Sato's experiments proved similar to Draxler's relationship in equation (6). The along-wind dispersion coefficient is proportional to the time raised to a power. This relationship between time and its exponent is shown below.

$$\sigma_x \propto t^{1.1} \tag{37}$$

While Draxler determined σ_x to be a function of time raised to a power of 1-1.5 due to either turbulence or wind shear, Sato determined the overall constant, a, to be 1.1.

1.3.5 Robins and Fackrell (1998)

Alan Robins and J. Fackrell (1998)[25] performed short duration releases in the Marchwood Wind Tunnel. Mixtures of propane and helium, to produce a neutrally buoyant cloud, were injected into a continuous stream of clean air at ground level from a 15 mm diameter tube. Ensemble averages from 150-300 realizations were used to determine concentration-time histories. The non-dimensionalized concentration as a function of time can be seen below in Figure 9.

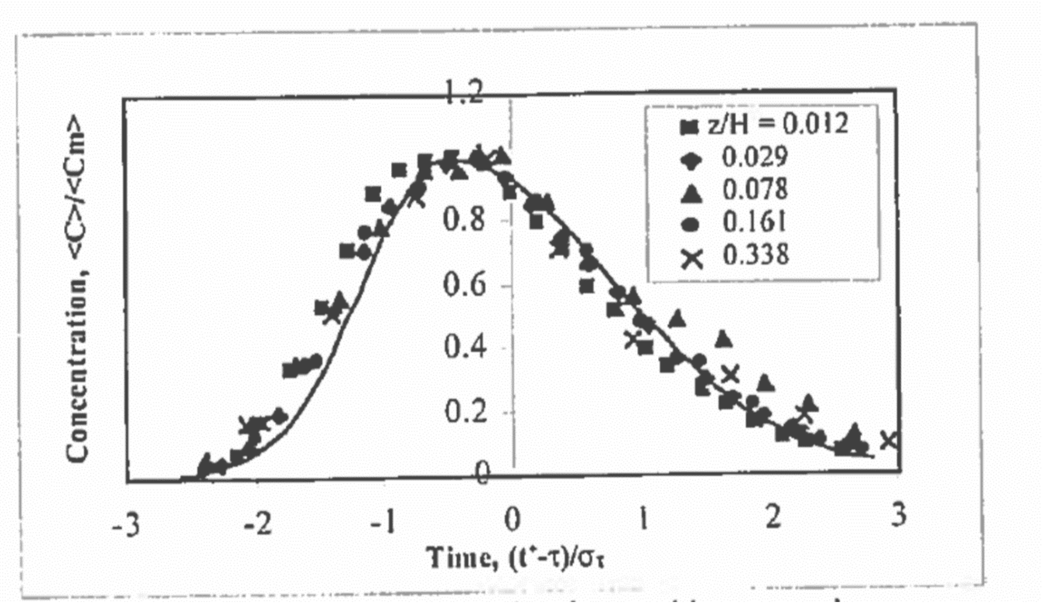

Figure 9. Distribution of non-dimensionalized ensemble averaged concentrations in a cloud, T* = 1.65, at x/H = 5.92. Predictions of a skewed Gaussian model are shown as a solid line[25]

Figure 9 shows the concentration as a function of time for ensemble averages. It is important to recognize that these releases are actually continuous releases with tracer puffs injected into the continuous releases. Consequently, the leading and trailing edges of the clouds produced by Robins and Fackrell may not adequately describe the behavior of finite-duration releases.

1.3.6 Summary of Empirical Derivations

Previous experimental studies span a range of different test conditions from release duration, chemical, release type, field or wind tunnel tests, wind speeds, terrain, surface roughness, and other conditions. A chart summarizing the overall empirical derivations and the varying test conditions is summarized below.

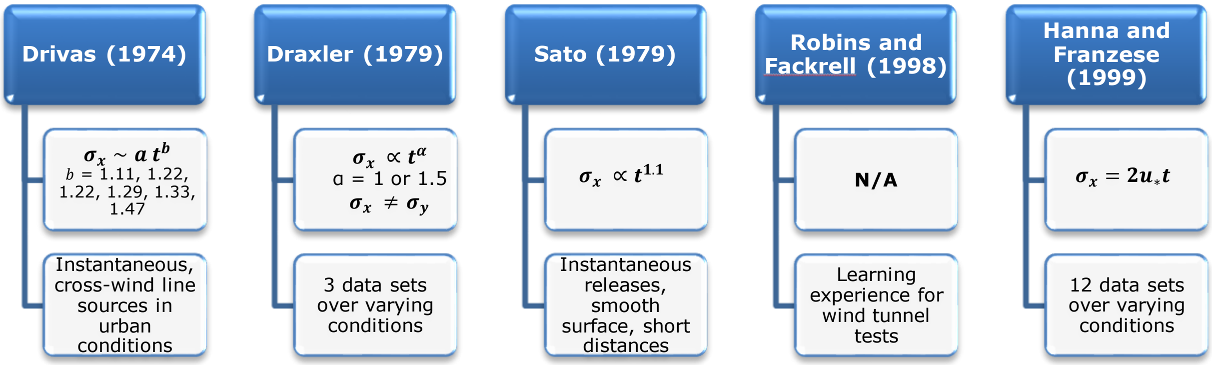

Figure 10. Summary of empirical derivations for along-wind dispersion

All empirical derivations are a function of time with a constant. This is similar to most of the theoretical derivations with exception to Wilson and Ermak as a function of distance. Similar to van Ulden, the time is raised to a power for stable stability classes. Only one derivation include friction velocity of the empirical equations.

1.4 Summary of Theoretical Framework and Empirical Derivations

Along-wind dispersion causes elongation of the cloud in the x-direction. This is caused by the shear and turbulence in the atmosphere acting on the cloud. The relationship between advection cloud speed, time, and distance to determine the along-wind dispersion coefficient is complex. Changing conditions such as stability class, surface roughness, wind speed, the function of distance or time, release height, and other parameters all affect determining the along-wind dispersion coefficient. With varying conditions or assumptions, not all the equations can be integrated into an overarching equation meeting all conditions. Different assumptions or criteria result in diverse equations for the same dispersion coefficient. In Table 2 are the summarized theoretical and empirical derivations for the overall along-wind dispersion equation, shear component, and turbulent component for each derivation.

Table 2. Comparison of shear and turbulence components with an overall along-wind dispersion equation

Author	Overall Along-wind dispersion Equation	Shear Component	Turbulent Component
Chatwin	$\sigma_x = 0.803\frac{u_* t}{\kappa}$	$\sigma_{xs} = 0.596\frac{u_* t}{\kappa}$	Not explicitly solved
Wilson	Ground: $\sigma_x = [0.09\left(\frac{x}{z_r \ln(z_c/z_o)}\right)^2 + \left(\frac{\sigma_{xt}}{\sigma_z}\right)^2]^{0.5}\sigma_z$ Elevated: $\sigma_x = [0.09\left(\frac{nx}{z_r}(\frac{z_r}{z_c})^n\right)^2 + \left(\frac{\sigma_{xt}}{\sigma_z}\right)^2]^{0.5}\sigma_z$	${\sigma_{xs}}^2 = \frac{1}{12}\left(\frac{dU}{dz}\grave{t}\right)^2 {\sigma_z}^2$	$\sigma_{xt} \simeq \left(\frac{u'}{w'}\right)\sigma_z$
Van Ulden	Neutral: $\sigma_x = 0.84\frac{u_* t}{\kappa}$ Stable: $\sigma_x = \{(\frac{3}{4} - \frac{16}{9\pi})\frac{5{u_*}^3 t^3}{kL}\}^{1/2}$ $\simeq 0.43(\frac{5{u_*}^3 t^3}{kL})^{1/2}$	$\sigma_s = 0.5\frac{u_* t}{\kappa}$ $\sigma_c \simeq \sigma_s = 0.5\frac{u_* t}{\kappa}$	$\sigma_d = 0.67\frac{u_* t}{\kappa}.$
Hanna	$\sigma_x = 2u_* t$	Smith's: $\sigma_{xs} = B\left(\frac{1}{\sqrt{12}}\right)\sigma_z\left(\frac{du}{dz}\right)t$	$\sigma_{xt} = Au_* t$
Saffman	Unbounded: ${\sigma_x}^2 = \alpha^2 t^2 (k_z t)^{\frac{2a}{2-c}} f(\rho) + k_x t (k_z t)^{\frac{d}{2-c}} f(\rho)$	$\sigma_{xs} = \frac{1}{\bar{u}}\sqrt{\frac{1}{25}\Psi^2 K_z T^3}$	Not explicitly solved
Drivas	$\sigma_x = at^b$	Experimental	Experimental
Draxler	$\sigma_x \propto t^\alpha$ $\sigma_x = 7.3t^{1.3}\ (specific\ case)$	Saffman's	$\sigma_{xt} = 3i^2 t$ $i^2 = \overline{u'^2}/_{\bar{u}^2}$
Ermak	$\sigma_x(x) = \sqrt{{\sigma_{xs}}^2(x) + {\sigma_{xt}}^2(x)}$	$\sigma_{xs}(x) = a_{xs}x\ , with\ a_{xs} = 0.6\,p\,[\frac{0.48}{\gamma}]^p$	$\sigma_{ya}(x) = \sigma_{xt}(x) = \left(\frac{t_{av}}{600}\right)^{0.2} * e^{I+J(\ln\left(\frac{x}{1000}\right)+K[\ln\left(\frac{x}{1000}\right)]^2}$

Although Saffman, Batchelor, Chatwin, and van Ulden have different assumptions on variables that influence the total effects on along-wind dispersion, all equations have similar outcomes with the along-wind dispersion coefficient, in neutral conditions, as a function of the friction velocity, travel time, and a constant that is approximately 0.8/κ or 2. Increasing the stability class from neutral to stable increases the effects of along-wind dispersion. This is seen with van Ulden's derivations, Drivas' and Draxler's experimental work, and Ermak's substitution for equations. Along-wind dispersion is observed in all atmospheric conditions. Additional correlations between different parameters will be discussed in the non-dimensionalized modeling section.

2 Non-Dimensionalized Equation

2.1 Introduction

The overall goal for the Ph.D. is to perform experiments and model the effects of along-wind dispersion of finite-duration contaminant releases in the atmosphere. While an experimental program was in the developmental stages for original finite-duration releases from an area source in an ultra-low speed wind tunnel, a model was developed before the testing started. Accumulation of previous experimental programs were available for analysis. The tests, standardization of data, analysis, and models are all discussed in this section to determine an optimal model for along-wind dispersion with previous data. A final recommendation for a non-dimensionalized model for along-wind dispersion is presented.

2.2 Available Data

In 2000, data were analyzed by Hanna and Franzese[20] from 11 field test programs and 1 wind tunnel test program totaling 452 data points over varying conditions. Tests available from the original 12 programs were analyzed in an effort to provide a parameterization of along-wind dispersion for ground level releases with an overall equation of $\sigma_x = 2u_* t$. Of the original 452 data points, six data points were not used in the analysis due to the lack of recorded friction velocity or wind speed, resulting in 446 data points. Data used in this analysis are described below.

2.2.1 DTRA Phase 1

The DTRA Phase 1 tests were carried out from the 9th -26th of September in 1996 at the Dugway Proving Ground on Pad 11 producing 23 ensemble averages[26]. Propylene was instantaneously released from air cannons at ground level. Each air cannon produced 0.36 kg of propylene in a period of 0.2-0.4 seconds. DigiPIDs and Ultra-Violet Ion Collectors were both used at distances of 200 m, 300 m, 400 m, 800 m, and 1200 m along a fixed sampling line 1.5 m above the ground. Because of the limited number of samplers, measurements were not made at every downwind location in a single test, and when samplers were located farther downwind, the quantity of propylene released was increased (1 air cannon was used for distances of 200 m and 300 m, 2 air cannons for 400 m, 4 air cannons for 800 m, and 8 air cannons for 1200 m) so a measurable amount of propylene was observed by the concentration sensors. Wind speeds (reference height of 2 m) ranged from 2 to 7 m/s. The surface roughness was estimated to be less than 1 mm.

2.2.2 Dipole Pride

Dipole Pride tests were grouped into day and night tests from the 4th -20th of November in 1996 at the Department of Energy Nevada Test Site – Yucca flat. SF_6 was released from 2 vertically mounted, pressurized cylinders on the back of a 5-ton flatbed truck. These point sources released 8-21.6 kg of mass in a duration of 1-3 seconds[27]. 90 whole air samplers, with 15 minute time averaging, and 6 continuous TGA-4000 SF_6 analyzers were placed in 3 lines at distances of 1 km, 10 km and 20 km[28]. Wind speeds (reference height of 10 m) ranged between 3 to 5 m/s during the day and 2 to 5 m/s during the night. Surface roughness at the Yucca flat was estimated to be 32 mm. Out of the 23 total tests, only 10-day releases and 5-night releases were suitable for analysis.

2.2.3 Kit Fox ERP, URA, SSR

All Kit Fox releases took place at the National Spill Test Facility at the Nevada Test Site. The Equivalent Roughness Pattern (ERP) and Uniform Roughness Array (URA) tests took place from the 24th - 31st of August in 1995 whereas the Smooth Surface Roughness (SSR) tests took place the 11th -15th of September in 1995.[29] The tests were similar in all conditions other than surface roughness. The Kit Fox ERP tests had a surface roughness of 0.2 m, the Kit Fox URA tests had a surface roughness of 0.02 m, and the Kit Fox SSR tests had a surface roughness of 0.002 m[30]. Carbon Dioxide was released from a ground level area source with dimensions of 1.5 m x 1.5 m x 1 m at a rate of 1 m/s resulting in 1.5 kg/s – 4 kg/s being released[31]. Concentrations were measured at distances of 25 m, 50 m, 100 m, and 225 m. Eighty-four high and low infrared concentration sensors, solid state infrared CO_2 sensors, and sample bag Nova sensors were all used to detect concentrations of CO_2 with an averaging time of approximately 20 seconds[32]. Wind speeds (reference height of 2 m) ranged between 2 to 3 m/s for the ERP and SSR test and 3 to 4 m/s for the URA tests. All tests took place immediately before sunset which resulted in lower wind speeds within the neutral-to-stable atmospheric stability range. The ERP and SSR tests produced 6 trials each, and the URA tests produced 9 trials used in this analysis.

2.2.4 Hanford Kr-85

The Hanford Fr-85[33] tests took place from 18 August to 8 November 1967 at the Battelle Pacific Northwest Laboratory. A vial containing Krypton 85 at ambient pressure was crushed by a guillotine-like device at ground level, instantaneously releasing a 1 m puff of the radioactive gas. Concentration was detected by 64 halogen-quenched Geiger-Muller tubes at a distance of 200 m and an elevation of 1.5 m above the ground. 24 halogen-quenched Geiger-Muller tubes were positioned on 6 towers at a distance of 800 m at elevations of 0.8 m, 4.6 m, 10.7 m and 21.3 m. The time averaging associated with the Geiger-Muller tubes was 4.8 seconds. 8 trials were performed, but only 6 releases remained within the boundary of the array of sensors. The wind speed was measured at a reference height of 1.5 m with speeds of 1 to 8 m/s. The roughness was estimated to be 30 mm due to the sagebrush and steppe grass.

2.2.5 LROD

The Long Range Overwater Dispersion (LROD)[34] tests took place from 13th - 26th of July in 1993 at the Pacific Missile Range Facility in Kauai, Hawaii. A crosswind line source of pressurized, liquid SF_6 was released from a high-pressure hose from the back of a plane at an elevation of 90 m at a rate of 9.6 g/meter and a speed of 129 m/s over water. The duration of the release of SF_6 was around 13 minutes for the 100 km line source. Concentration was measured at ground level from boats along with planes at various elevations using electron capture detectors (ECD) and TGA-4000 whole air samplers. The averaging time was around 30-120 seconds for the sequential bag samples. Noise associated with the continuous analyzer resulted in limited use. Concentration was detected from the plane by flying parallel to the dissemination line and 45 km south of the sampling line (5 km, 15 km, 30 km, 60 km, and 100 km). The plane, equipped with a continuous SF_6 analyzer, would fly to the dissemination line then back to 25 m. It would slowly ascend from 25 m to 2500 m for various heights. Testing over water resulted in a surface roughness of 0.02-0.86 mm. A reference height of 10 m was used for wind speed with measured speeds of 3 to 11 m/s. The LROD tests produced 11 ensemble averages.

2.2.6 OLAD

The Over Land Along-wind Dispersion (OLAD)[35] tests were similar to the LROD tests, except over land. These tests took place from the 8th -25th of September in 1997 at the Dugway Proving Ground, West Desert Test Center. SF_6 was released from both plane and truck line sources. The plane released 100 kg of SF_6 at an elevation of 100 m from an N_2 pressurized tank at a rate of 33.3 kg/min for a distance of 20 km. The truck released 15 kg of SF_6 at an elevation of 3 m from a mounted tank at a rate of 1.5 kg/min for a distance of 10 km. Concentrations were recorded with

TGA-4000 whole air samplers, with time averaging of 15 minutes, and 2 continuous electron capture detector (ECD) analyzers at the end of each line at distances of 2 km, 5 km, and 10 km for the truck releases and 10 km, 15 km, and 20 km for the plane releases. Wind speed was measured at the height of 2 m with speeds of 0.5 to 7 m/s. The surface roughness was estimated to be 30 mm. These tests resulted in 3 ensemble averages for the aircraft release and 8 surface ensemble averages for the truck release.

2.2.7 Marchwood Wind Tunnel

The Marchwood[25] wind tunnel tests were the only tests that took place in a wind tunnel in the U.K. A mixture of propane and helium, resulting in neutral buoyancy, was released from a 15 mm ground level point source. The mixture was released for a duration of 0.5 – 12 seconds. 150-300 releases were summarized into 4 ensemble averages. A single FID measured the concentration with a 5 ms sampling interval at locations of 1 m, 3 m, 5 m, and 7 m downwind of the source. Wind speeds ranged from 1-4 m/s at neutral stability class. Surface roughness was estimated to be 0.3 mm for the wind tunnel. The data was not scaled in the analysis.

2.2.8 Oceanside

The Oceanside[36] tests took place at the shoreline of Oceanside and Del Mar in Southern California. 20 µm particles of green and yellow fluorescent pigment (FP) were released by plane, boat, and land with standard Dugway Proving Ground equipment. For the plane releases, the DPG model D-1 released 1500 g/min of FP for a duration of 10 minutes at elevations of 61 m, 122 m, and 152 m over a distance of 40 km. For the boat releases, a DPG Mark IV was used to release 110 g/min for a duration of 2 hours at sea level over 40 km. For instantaneous land releases, the DPG Mark IX was used at three different inland locations to release 10-50 g of FP instantaneously at ground level. The concentration of FP was recorded using rotorod samplers, sequential samplers, vertical samplers, 100 m square grids, dense sampling lines, and metronics drum impact samplers. Time averaging ranged from 5 minutes at coastal regions to 15 minutes at inland conditions. Surface roughness ranged from 30-50 m due to the coastal shoreline. The wind speed reference height varied from 8-120 m with wind speeds ranging from 1-5 m/s.

2.2.9 Fort Wayne

Fort Wayne[37] releases took place in the summer and fall of 1963 in Fort Wayne, Indiana. An aerosol of fluorescent pigment (FP) was released from 2 aircraft in the form of an elevated, 91-244 m, line source over flat farmland that transitioned into urban conditions in Fort Wayne, Indiana. Dry green and yellow FP were released from the planes via FP dispensers supplied by the Dugway Proving Ground. The amount of release was measured by the difference in weight, before and after. The release was upwind of the 180,000 population urban setting with a river running through the city and surrounding agricultural area. Rotorods, Gelman throw-away plastic filter holders, and Gelman paper tape samplers were used for concentration measurements of the FP. The tape provided an averaging time of 5 minutes where the filter holders had an averaging time of 30 minutes. Wind speed was measured at the release height and resulted in speeds ranging from 5-16 m/s.

2.2.10 Short Range Diffusion Experiment Series (SRDES)

The Short Range Diffusion Experiment Series (SRDES)[38] took place in 1979 in Japan by Sato. A 200 m x 200 m vacant lot covered in turf and surrounded by trees was used for the releases. NO_x

was released instantaneously from a balloon at an elevation of 1.5 m. Chemiluminescence NO_x meters were used to detect concentration with a sampling time of <2 minutes. Sample lines were chosen at distances of 60 m and 100 m. Wind speeds were referenced at heights of 0.5 m, 3 m, and 9 m with speeds of 1-2 m/s.

2.2.11 Summary of Tests

Of the 12 experimental programs analyzed, the test conditions vary in location, release height, duration, surface roughness, tracers, and more. An overall summary of each of the different test conditions and uniqueness is shown below in Table 3.

Table 3. Summary of 12 data sets used by Hanna and Franzese in their original analysis

Name	Location	Release	Duration of Release	Unique Conditions
DTRA – Phase 1	Dugway Proving Ground (z_o = 0.3 mm)	Ground level Puff (C_3H_6)	27 – 271 seconds	Ensemble averages
Dipole Pride	Nevada Test Site (z_o = 32 mm)	Ground level Puff (SF_6)	1,692 – 5,112 seconds	Day and Night
KitFox URA	Nevada Test Site (z_o = 20 mm)	Ground level Puff (CO_2)	65 – 95 seconds	Artificial roughness
KitFox ERP	Nevada Test Site (z_o = 200 mm)	Ground level Puff (CO_2)	72 – 91 seconds	Artificial roughness
LROD	Pacific Missile Range Facility (z_o = 0.02-0.86 mm)	90m elevated line source (SF_6)	260 – 12,645 seconds	Airplane release Concentration monitors on boats and airplane
OLAD (van and plane releases)	Dugway Proving Ground (z_o = 30 mm)	100m elevated line source Ground level line source (SF_6)	Van: 180 – 11,820 seconds Plane: 120 – 9,730 seconds	Airplane release Truck release
Marchwood	Marchwood Wind Tunnel (z_o = 0.3 mm)	Ground level Puff (C_3H_6 and He)	2.1 – 11 seconds	Wind Tunnel
Hanford	Battelle Pacific Northwest Laboratory (z_o = 30 mm)	Ground level puff (Kr 85)	39 – 778 seconds	Guillotine like releases of crushed vials

From Table 3, the different test conditions are able to be compared and contrasted across all tests. A non-dimensionalized equation developed from the multiple different tests spanning a variety of conditions will be most beneficial when predicting the along-wind dispersion coefficient for a variety of releases.

2.3 Standardization of Available Data

The test programs mentioned above provides a multitude of available data. The majority of the test programs published their analyzed results through journals. Very few test programs made the raw data available in addition to what was published in journals. If a report or journals did not provide the data needed, the authors or facility were contacted for the original data. Once all of this data was acquired, it was analyzed and standardized for a more uniform analysis. Analysis of the original data was performed to fully understand which methods were chosen to derive specific values such as time, stability class, wind speed, along-wind dispersion coefficient, and more. For the along-wind dispersion coefficient, the most common method was to derive σ_x from σ_t, the standard deviation of the concentration-time history, and u_e, the effective cloud wind speed. Some of the older trials reported σ_x without any indication of how it was derived. All of the derivations were determined before analysis was performed. The standardization took place for the data that was available for model development, uniform wind speed reference height, and uniform determination of stability class as described below.

2.3.1 Data Used in Model Development

Not all data is of the same caliber for an overarching equation for along-wind dispersion. For adequate analysis, the distance (m), time (s), wind speed (m/s), friction velocity (m/s), and measured σ_x (m) needs to be reported. Data from DTRA Phase 1, Dipole Pride, KitFox (URA and ERP), LROD, OLAD, Marchwood, and Hanford test cases all have sufficient data recorded to perform data analysis. The SRDES tests could not be used due to the fact that wind speed was not recorded. Data from the Oceanside test also was not able to be used due to the friction velocity not recorded. Kit Fox SSR, Fort Wayne, and the EAPJ data have major parameters missing from the data collection. These missing parameters were not found in original papers or in Hanna and Franzese's original analysis and therefore could not be used in the data analysis. Overall, there were 446 recorded data sets with sufficient data reported to be considered for analysis for an overarching equation for along-wind dispersion.

The above description of the tests shows that some of the data sets are directly applicable to addressing the description of along-wind dispersion for ground level releases while some data sets are not. The tests performed in the upper boundary layer with plane releases are determined not to have as much control over experimental conditions as the ground level releases. These tests (LROD and OLAD-plane) will not be used in the model or validation data. With the majority of hazardous releases dispersed before 10,000 m downwind, data obtained at distances of less than 10,000 m are emphasized for model generation and validation. This distance restriction excludes the Victoria tests. Under these tight constraints, only the most reliable data is used for model development.

2.3.2 Standardization of Reference Height

For a more standardized data analysis, all parameters need to be comparable. Original reference heights varied from 1.5 m, 2 m, and 10 m. A standardized reference height of 10 m was chosen to fit current models. The power law wind speed profile shown in equation (38) below, was used to standardize the reference height for all ambient wind speeds.

$$u_x = u_o \left(\frac{z}{z_R}\right)^{\alpha} \tag{38}$$

Where u_o is the reported velocity from the test, z_R is the reference height of wind velocity profile specification in the test, z is the standardized reference height of 10 m, u_x is the standardized ambient velocity at a reference height of 10 m, and α is a constant. This α constant was determined from a weighted least-squares fit with to the logarithmic wind speed profile that includes the Monin-Obukhov length, λ, shown below in equation (39) calculated in the program DEGADIS.

$$u_x = \frac{u_*}{k}\left[\ln\left(\frac{z + z_o}{z_0}\right)\psi\left(\frac{z}{\lambda}\right)\right] \tag{39}$$

In equation (39), z_0 is the surface roughness, ψ is a function of the surface roughness, z is the height, λ is the Monin-Obukhov length, and k is the Von Karmen constant which is 0.35 within DEGADIS.

Standardized wind speeds calculated at the height of 10 m were used in place of the reported wind speeds in the original data files. This standardized height allows for a more accurate comparison of the effect of wind speed on the along-wind dispersion coefficient.

2.3.3 Standardization of Stability Class

Atmospheric stability is an important parameterization. Atmospheric stability is a function of the solar insolation, cloud coverage, and wind speed. Pasquill stability classes are the most widely used parameterization of atmospheric stability and will be used in the analysis in addition to Monin-Obukhov length if reported. How a test is classified into its respective stability class is debatable. Golder’s plot, shown below, is widely accepted as one of the best methods to determine Pasquill stability class from surface roughness and the Monin-Obukhov length.

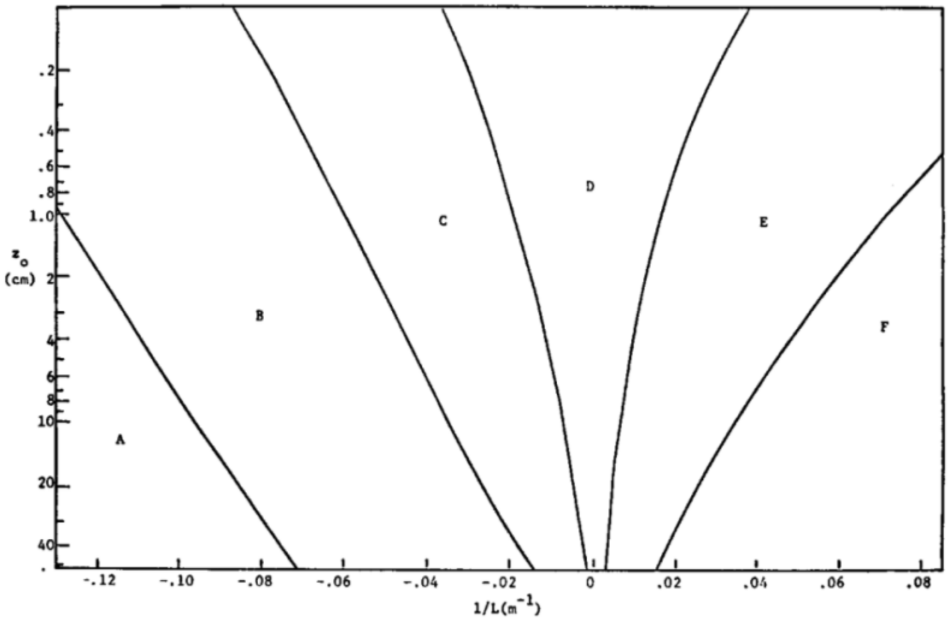

Figure 11. The inverse of the Monin-Obukhov length as a function of surface roughness to determine Pasquill stability class[39]

Figure 11 shows how the inverse Monin-Obukhov length and surface roughness can be plotted resulting in categories to determine Pasquill stability class. Image analysis software, Engauge, was used to recreate Golder’s plot. Data points were then plotted in this recreated Golder’s plot to determine stability class as a function of surface roughness and Monin-Obukhov length. A total of 307 data points had both the surface roughness and Monin-Obukhov length available for analysis. Results of the classification by stability class from Golder’s plot are shown below in Table 4.

Table 4. All tests arranged by stability class from Golder’s plot

Stability Class	A/B	C	D	E	F
Total Tests	5	24	258	15	5

From Table 4, it is clear that there are more tests falling into stability class D than any other stability class. As mentioned prior, not all tests will be used for model development. Only 89 data points were considered of high quality among all data available for model development. These quality data points are shown below in Table 5.

Table 5. Quality Tests arranged by stability class from Golder's plot

Stability Class	A/B	C	D	E	F
Total Tests	5	24	40	15	5

Table 5 shows that among the quality data, there are about 29 unstable tests, 40 neutral tests, and 20 stable tests to be used for the model development. This spread of tests has a more uniform distribution of classes when compared to Table 4 which shows all available data.

2.4 Parametrization and Data Analysis Tools

The along-wind dispersion coefficient depends on multiple variables as shown in the first section of this dissertation. The best parameterization of data needs to be determined for future models by both visual and statistical comparisons. Both numerical and visual comparisons of the models with the raw data and Hanna's equations was performed to determine the optimal model for along-wind dispersion. Multivariable regression analysis was performed to determine constants for the non-dimensionalized models. To determine how the non-dimensionalized models compare with previous models and the original data, both numerical and visual comparisons are performed.

2.4.1 Multivariable Regression Analysis

To determine the numerical values of the non-dimensionalized equations (NDEs), a multivariable regression analysis was performed in Matlab[40]. A multivariable regression analysis, also known as multiple regression, is an extension of linear regression to determine the relationships among variables[41]. With multivariable regression, the relationships between multiple independent variables and their impact on the equation can be determined. Regression analysis is a useful tool in understanding the changes of one variable with respect to other variables. The form of a typical multi-variable regression analysis is shown below in equation (40)

$$Y = a + b_1 x_1 + b_2 x_2 + \cdots + b_n x_n \qquad \textbf{(40)}$$

where the x_n values are the different independent variables and Y is the dependent variable. In equation (40), the values of a and b are constants. A multi-variable regression analysis is applied to the non-dimensionalized equations using a least-squares fit to determine the constants.

2.4.2 Visual Representation of Parameterization

Experimental data has been numerically represented as the along-wind dispersion coefficient as a function of time, friction velocity, wind speed, surface roughness, and other parameters. The two most common parameterizations in theoretical and experimental representations for along-wind dispersion are $\frac{\boldsymbol{\sigma_x}}{\boldsymbol{u_*}}$ or $\frac{\boldsymbol{\sigma_x}}{\boldsymbol{u}}$ vs. t. These two relationships are compared both visually and statistically to determine the best parameterization of the overall data in the following analysis. Figure 12 and Figure 13 represents $\frac{\boldsymbol{\sigma_x}}{\boldsymbol{u_*}}\ vs.\ t$ and $\frac{\boldsymbol{\sigma_x}}{\boldsymbol{u}}$ vs. t respectively, for the original data.

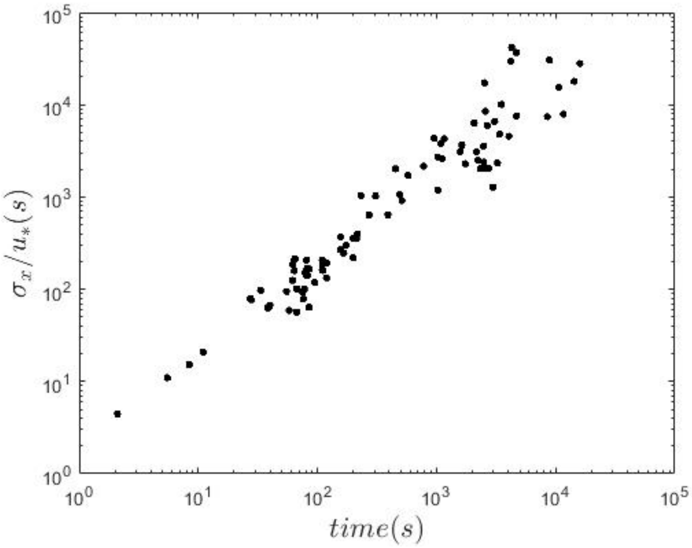

’’’

Figure 12. Time (s) vs. σ_x/u_* (s) for all of the original reported data and Hanna’s equation for a visual comparison

In Figure 12 the relationship between $\frac{\sigma_x}{u_*}$ vs. t shows about 1 order of magnitude between the data points. This figure shows a decent collapse of the data to provide a somewhat “linear” fit.

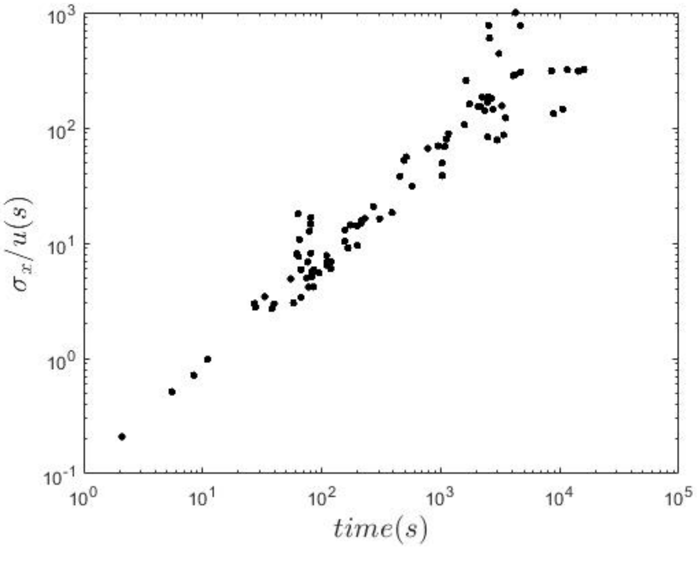

Figure 13. Time (s) vs. σ_x/u (s) for all of the original reported data and Hanna’s equation for a visual comparison

Figure 13 displays $\frac{\sigma_x}{u}$ vs. t which shows a greater order of magnitude between the data points at the same time. Overall, Figure 12 shows a better parameterization for the along-wind dispersion coefficient through visual comparison. In addition to visual parameterizations of data, numerical comparisons were performed.

2.4.3 Parity Plots

Another visual comparison of how well a model or equation predicts data compared to the original data is a parity plot. A parity plot is a single plot with the original values on the x-axis with the predicted values on the y-axis. A reference line is drawn through the center of the plot showing a 100% correlation between the original data and the predicted data. This plot shows a visual comparison of how the predicted data compares or collapses, with the original data. A parity plot of the original data vs. Hanna's equation, $\sigma_x = 2u_* t$, is shown below in Figure 14. This equation was chosen as the original model developed with the analyzed data above.

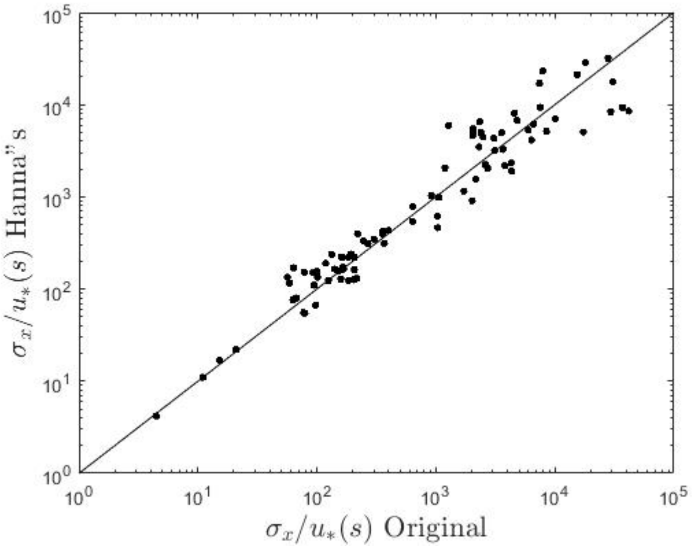

Figure 14. σ_x/u_* (s) Original data vs. σ_x/u_* (s) Hanna's equation prediction for all of the quality data with a reference line showing 100% match

Figure 14 shows the relationship between Hanna's equation for along-wind dispersion and the original data. From the reference line, it can be seen that the predicted data from Hanna's equation overpredicts the data around 100 seconds. Predicted data greater than 100 seconds is evenly over- and underpredicted. Parity plots were used as an additional method to compare the non-dimensionalized predicted data to the original data visually to see how the data collapse.

2.4.4 Non-Parametric Statistical Analysis

One method to analyze the efficiency of the model is to perform a statistical comparison. With small sample sizes, a Gaussian distribution is not achieved. A non-parametric statistical analysis[42] was performed on the predicted vs. original data for the first NDE as a numerical comparison quantifying the performance of the NDE compared to the original data. For the non-parametric statistical analysis, a ratio of the predicted σ_x value compared to the recorded σ_x data was determined. A 90% confidence interval determined the statistical relevance of NDE. Due to a small sample size of certain tests, the non-parametric confidence interval was chosen for evaluation of the parameters of all categories for a comparable preliminary analysis.

2.4.5 Geometric Mean Bias and Geometric Mean Variance

Another numerical method is the comparison of the geometric mean bias (MG) and geometric mean variance (VG). This method of comparing MG VG values was developed by Hanna, Chang, and Strimaitis in 1993 when comparing hazardous gas models and is accepted in this field for model comparisons[43]. The geometric mean bias (MG) equation for an individual point can be seen below in equation (41)

$$MG_1 = exp[Ln(X_{o1}) - Ln(X_{p1})] \tag{41}$$

where MG_1 is the geometric mean bias for a single point, X_{o1} is the original or observed data, and X_{p1} is the predicted data. For a set of n pairs of data, equation (42) can be used to predict the geometric mean bias for a set of points

$$MG_{set} = (MG_1 * MG_2 * \dots MG_n)^{1/n} \tag{42}$$

where MG_{set} corresponds to the geometric mean bias for the set of data. Likewise, geometric mean variance (VG) can be calculated for a single point using equation (43) below

$$VG_1 = exp[\{Ln(X_{o1}) - Ln(X_{p1})\}^2] \tag{43}$$

where VG_1 is the geometric mean variance observed from a single data point. The geometric mean variance for a set of data can be determined using equation (44)

$$VG_{set} = (VG_1 * VG_2 * \dots VG_n)^{1/n} \tag{44}$$

where VG_{set} corresponds to the geometric mean variance observed from the set of data. Values of 1 for MG and VG values are closest to the original values. Values further from 1 for MG and VG values are further away from the original data. If the MG value is less than 1, then the σ_x value is over predicted. If the MG value is greater than 1, then the σ_x value is under predicted. With a σ_x <1, the overall predicted concentration would be less than the observed concentration. Similarly, if σ_x >1, the overall predicted concentration would be greater than the observed concentration. The VG value shows the variance of the predicted data from the original data. Overall, this MG VG method is able to provide a statistical comparison between individual data points and data sets for predicted data and the original data.

Going back to the $\frac{\boldsymbol{\sigma_x}}{\boldsymbol{u_*}}$ vs. t and $\frac{\boldsymbol{\sigma_x}}{\boldsymbol{u}}$ vs. t parameterizations, a MG VG comparison was performed as a numerical method to quantify the optimal parameterization. The MG VG values from both the

$\frac{\sigma_x}{u_*}$ vs. t and $\frac{\sigma_x}{u}$ vs. t were calculated using the original data for X_o values and Hanna's prediction for X_p values. The MG VG values for $\frac{\sigma_x}{u_*}$ vs. t were 0.56 and 2.30 respectively whereas the MG VG values for $\frac{\sigma_x}{u}$ vs. t were 0.50 and 3.16 respectively. Optimal values of MG and VG are close to 1, therefore the $\frac{\sigma_x}{u_*}$ vs. t parameterization is better than the $\frac{\sigma_x}{u}$ vs. t and will be used throughout. This relationship may not have been clearly shown in the visual representation. Both the visual and numerical comparisons of data will be performed for all NDEs developed.

2.5 Non-Dimensionalized Equation (NDE)

Along-wind dispersion causes elongation of contaminant clouds in the x-direction due to shear and turbulence effects in the atmosphere. This elongation is important to model for correct predictions of concentration measurements in the leading edge of the cloud. The effect of advection cloud speed, time, and distance on the along-wind dispersion coefficient is complex. Changing conditions such as stability class, surface roughness, wind speed, release height, and other parameters all affect the along-wind dispersion coefficient. With varying conditions, not all theoretical or experimental equations are able to be integrated into an overarching equation incorporating all parameters. Different assumptions or criteria result in diverse equations for the same dispersion coefficient. At the end of the first section, a table summarizes the overall along-wind dispersion equation, the shear component, and the turbulent component for each theoretical derivation or empirical relationship.

Theoretically, Saffman, Batchelor, Chatwin, and van Ulden have different assumptions on parameters that influence the total effects on along-wind dispersion. All of these derived equations result in an along-wind dispersion coefficient, σ_x, as a function of friction velocity, u_*, travel time, t, and a constant, of approximately 0.8/κ or 2, in neutral stability. Theoretical derivations are predominately derived for neutral stability class. However, along-wind dispersion is observed in all stability classes. The more stable the atmosphere, the greater effect along-wind dispersion plays. This is seen with van Ulden's derivations, Drivas' and Draxler's experimental work, and Ermak's substitution for equations. To predict the along-wind dispersion coefficient, non dimensionalized equations (NDEs) were developed and validated with the available data.

2.5.1 Original NDE

Batchelor's Lagrangian similarity theory predicts σ_x to be a function of friction velocity, u_*, and time, t, while ignoring the release height[13]. This $\sigma_x = Cu_*t$ is expanded upon to get a non-dimensionalized equation. Van Ulden predicts separate equations for both neutral and stable conditions[19]. Surface roughness has been shown to have an effect on wind speed[44]. Surface roughness and stability class are incorporated in the $\left(\frac{u_*}{u}\right)$ part for the NDE. Based on these hypotheses, the original non-dimensionalized equation for along-wind dispersion was developed starting with $\sigma_x = Cu_*t$, and added $\left(\frac{u_*}{u}\right)$ and distance to fully non-dimensionalized the equation resulting in

$$\frac{\sigma_x}{x} = C_1 \left(\frac{ut}{x}\right)^p \left(\frac{u_*}{u}\right)^q \tag{45}$$

where p, q, and C_1 are all dimensionless constants. The $\left(\frac{ut}{x}\right)$ term accounts for the effect of wind speed, u, time, t, and distance, x. The $\left(\frac{u_*}{u}\right)$ term takes into account the stability class and surface roughness.

Multiple parameters were analyzed for optimal prediction of the along-wind dispersion equation. Data were quantified and analyzed based on all data vs. quality data, individual test conditions, surface roughness, stability class, and near field vs. far field. The classifications used to determine the constants for each group, as well as the results of these models, are shown below in the subsequent sections.

2.5.1.1 Validation of Original NDE with All Data

As a first approach, a generalized all-encompassing non-dimensionalized equation was determined using all 446 data tests. Results of the constants determined with all data are shown below.

Table 6. Constants determined for an original non-dimensionalized equation with all 446 tests

Constants	All Data
C_1	0.55
p	1.11
q	0.68
Total Tests	**446**

A visual representation of all of the data plotted as a function of friction velocity and time with the original non-dimensionalized equation using all 446 data points is shown below in Figure 15.

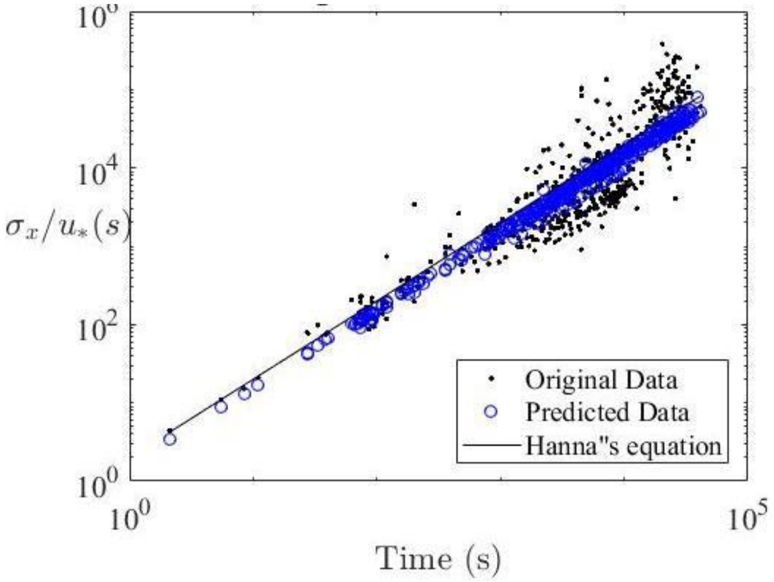

Figure 15. Time (s) vs. $^{\sigma_x}/_{u_*}$ (s) as a function of the original data, original NDE predictions using all 446 data points, and Hanna's predictions

In this figure, the original data and Hanna's predicted equation are used as references for the predicted data from the original non-dimensionalized equation with all 446 data points to determine the constants. This equation is a better fit than Hanna's equation for the data between 1,000 and 10,000 seconds but overall underpredicts the data above 10,000 seconds more so than Hanna's equation.

2.5.1.1.1 Individual Tests

Parameterization by individual test sets was performed as well. Each test site has a unique surface roughness, chemical released, equipment, procedures, and other classifications. Each test spans a range of stability classes, wind speed, friction velocity, and additional conditions. The results of constants determine from each individual test is shown below in Table 7.

Table 7. Constants determined for non-dimensionalized equation by individual tests

Constants	LROD	Dipole Pride	DPG	KF ERP	KF URA	OLAD - van	OLAD - plane	Marchwood	Hanford
C_1	0.05	0.004	0.01	0.14	0.002	0.000	0.34	0.07	4.66
p	0.34	-1.33	-0.85	-1.07	-0.78	-0.13	0.20	1.43	1.87
q	0.21	-1.00	-0.70	-0.32	-1.91	-2.83	0.31	0.00	1.48
Total Tests	**192**	**15**	**17**	**6**	**9**	**26**	**26**	**4**	**12**

Parameterization by individual test sets does not show a good correlation between the individual test sites and conditions. Some tests have negative values for the exponent. Some values have certain constants close to zero showing no impact for those parameters. These results could be due to the different conditions experienced at each site. The wide array of results could also be due to small sample size such as Marchwood Wind Tunnel tests with only 4 tests. While these results show no correlation in individual test sets, this information indicates that along-wind dispersion cannot be predicted easily with the individual test sets and that all data must be incorporated for an accurate model for along-wind dispersion.

2.5.1.1.2 Friction Velocity

A potential parameterization was to separate the tests by friction velocity. With the friction velocity being a function of wind speed and surface roughness, this parameter could account for both wind speed and surface roughness indirectly. The relationship between friction velocity and surface roughness is shown below in equation (46)

$$u_* = \frac{ku}{\ln\left(\frac{z}{z_0}\right) - \psi_m\left(\frac{z}{L}\right)} \qquad \textbf{(46)}$$

Values for surface roughness were not similar, with values of 0.3 mm, 20 mm, 30 mm, or 200 mm throughout the different tests, which made parameterization by surface roughness not very feasible.

With the friction velocity as a function of surface roughness and wind speed, surface roughness is taken into account in the friction velocity term. Results of constants determined by the classification of friction velocity are shown below in Table 8.

Table 8. Constants determined for original non-dimensionalized equation by friction velocity

Constants	0-0.09	0.1-0.19	0.2-0.29	0.3-0.39	0.4-0.49	0.5-0.59	0.6-0.69
C_1	0.50	0.60	0.25	15.1	1.51	0.70	0.003
p	0.24	0.54	1.44	0.85	0.65	-0.10	0.28
q	0.36	0.61	0.24	1.90	0.89	0.68	-1.49
Total Tests	**24**	**42**	**126**	**172**	**24**	**37**	**21**

Although there are no real trends between classifications, the values are mainly positive and more reasonable than the previous correlation by individual test sets. This shows improvement compared to the other classifications performed prior but clearly not the optimal fit.

2.5.1.1.3 Stability Class (Monin-Obukhov Length)

Stability class has a large effect on dispersion in the atmosphere. It was decided to classify the tests by Pasquill stability classes to see if trends would occur. Not all tests had stability class reported. Monin-Obukhov length and surface roughness were used with Golder's graph shown above to group the data into stability classes. A total of 307 tests had both the surface roughness and Monin-Obukhov length. These data points were used for this classification by stability class. Results of the original non-dimensionalized equation with parameterization by stability class are shown below in Table 9.

.

Table 9. Constants solved for original NDE by stability class

Stability Class	A	B	C	D	E	F	G
C_1	0.02	0.05	0.61	14.23	27.63	1.05	0.73
p	-0.86	-2.05	0.62	1.31	-0.28	0.40	0.09
q	-0.44	-0.11	0.63	1.89	2.08	0.73	0.44
Total Tests	4	16	22	180	58	20	7

From the constants determined, there are slight correlations between the stability classes. We can see unstable classes having a trend of more negative exponents. Stability class C-G has mainly positive constants for exponents. Stability class E has a negative value for p and a very large constant. This is believed to be caused by a large amount of LROD airplane releases tests skewing the data. While slight trends are shown with this parameterization with all data, the trends are not substantial enough to elaborate upon further.

2.5.1.1.4 Near Field vs. Far Field (Time)

“Near field” and “far field” are commonly referred to with modeling of releases in the atmosphere. The distinction between near field and far field is not well defined but commonly determined through Richardson number or an arbitrary value. For this analysis, arbitrary values were chosen for the distinction between the near field and far field. Results of constants using 1,000, 3,000, 5,000, 7,500, and 10,000 seconds as the separation value of near field and far field are all shown below in Table 10.

Table 10. Constants determined from multivariable regression analysis for original NDE categorized by near-field vs. far field by the time

Constants	Near/Far	1,000 sec	3,000 sec	5,000 sec	7,500 sec	10,000 sec
p	Near	0.85	1.02	0.98	1.08	1.18
	Far	1.06	1.20	1.36	1.24	0.67
q	Near	1.09	1.37	1.20	1.10	1.10
	Far	0.62	0.45	0.35	0.13	-0.27
C_1	Near	2.54	4.56	2.62	1.84	1.72
	Far	0.44	0.28	0.21	0.12	0.05

Additional trends are brought to light through parameterization of near field and far field. The values for the constant p in the near field increases as the value for the transition increases showing an increased dependence on time, wind speed, and distance. The values for the constant p in the far field is larger than p in the near field for 4 of the 5 tests. The big trend shown is in q and C_1 for the far field. Both of these constants decrease as the arbitrary value for the split increases. This decreased dependence on the $\left(\frac{u_*}{u}\right)$ is believed to be showing the effect of the planetary boundary layer. A visual representation of the non-dimensionalized predicted σ_x values, Hanna and Franzese's σ_x values, and the original σ_x values as a function of time are all shown below in Figure 16.

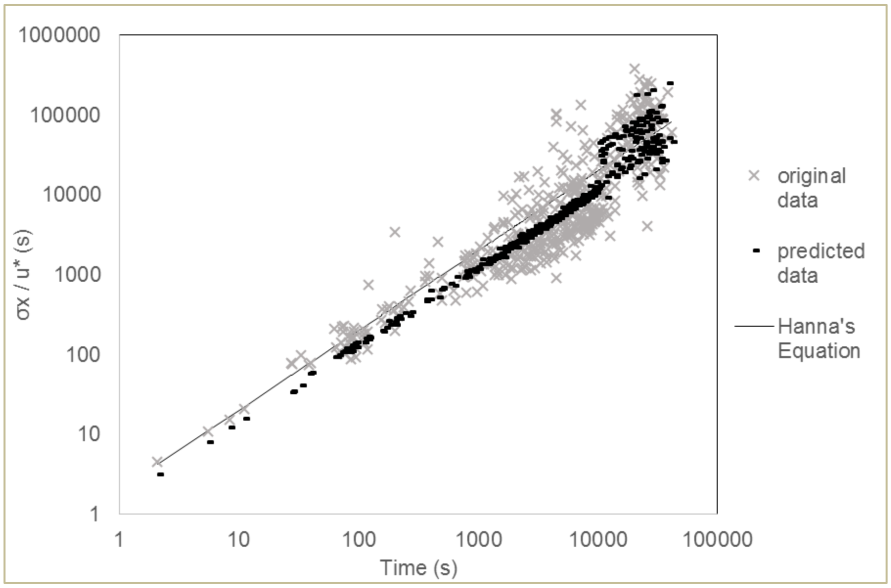

Figure 16. Time (s) vs. σ_x / u_* (s) as a function of the original data, original NDE predictions by the near and far field with 10,000s as the divide, and Hanna's predictions

This prediction of σ_x values with the NDE by near field and far field is a better fit than Hanna's prediction. From 1,000-10,000 seconds, the predicted σ_x values are a better fit than Hanna's equation which is over predicting the σ_x values. In the far field, from 10,000-100,000 seconds, the data predicted values are more dispersed, fitting the real data better than a straight line from Hanna's equation. These results show promising trends for an overall along-wind dispersion equation.

2.5.1.1.5 Near Field vs. Far Field (Distance)

Near field and far field classification was also tested as a function of distance in place of time. Again, the distinction between near field and far field is not well defined. Arbitrary values were chosen for this separation of 1,000, 2,000, 3,000, 5,000, 10,000, and 15,000 meters. Results of the constants from these values are shown below in Table 11.

Table 11. Constants determined from multivariable regression analysis with original NDE categorized by near-field vs. far-field by distance

Constants	Near/Far	1,000 m	2,000 m	3,000 m	5,000 m	10,000 m	15,000 m
p	Near	0.54	0.49	0.47	0.61	0.76	0.90
	Far	1.05	1.04	1.05	1.03	1.02	1.04
q	Near	1.08	1.15	1.18	0.92	0.99	0.70
	Far	0.64	0.61	0.61	0.59	0.55	0.60
C_1	Near	3.27	4.15	4.42	1.86	2.05	0.72
	Far	0.47	0.42	0.42	0.39	0.34	0.40

There are not as many trends shown when parameterizing the values by distance. However, the values in the far field are fairly stable for all distances which were not shown with the classification of near field and far field by time.

2.5.1.2 Original NDE validated with "Model" Data

As mentioned in section 2.3.1, certain tests are more applicable to addressing along-wind dispersion for ground level releases. The tests determined to be used for "model" development are Marchwood, KitFox ERP, KitFox URA, DTRA phase 1, Hanford, and Dipole Pride. Note the "model" data and "validation" data are different. In the original discrimination of tests, the OLAD-van tests were not included. Later on, the OLAD-can tests were included due to additional scrutiny of the data. For the "model" tests used here, a total of 63 quality test points were used to develop the non-dimensionalized equation. Results of a multi-variable regression analysis using only the "model" data are shown below in Table 12 compared to all of the data.

Table 12. Constants determined for original NDE equation with "model" data

Constants	All Data	"Model" Data
C_1	0.55	0.108
p	1.11	1.12
q	0.68	0.11
Total Tests	**446**	**63**

The constants determined from using only "model" data sets are comparable for *p* values obtained using all data. The values for *q* and C_1 change when using only "model" data to determine the constants. A visual representation of these values is shown below in Figure 17 with the "model" data points.

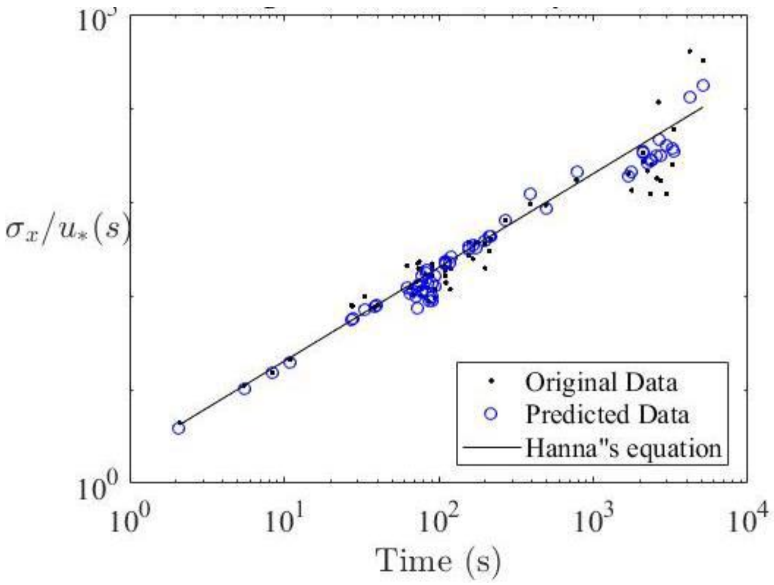

Figure 17. Time (s) vs. $^{\sigma_x}/_{u_*}$ (s) as a function of the original data, original NDE predictions using "model" data points, and Hanna's predictions

This figure shows the fit of the original non-dimensionalized equation with constants derived from the "model" data. This graph represents 63 data points that are able to be modeled with improved accuracy than the original non-dimensionalized equation with all data for constants derived. Model data is of a higher caliber and more controlled test environment than other data. Trends of stability class are retested with only the “model” data.

2.5.1.2.2 “Model” Data Sets by Stability Class

The first trend that was observed with all of the data and the original NDE were slight trends in stability class. Further classification of the “model” data by stability class was analyzed. The results of “model” data with stability class are shown below in Table 13 with previous constants determined for comparison.

Table 13. Constants determined from multivariable regression analysis from original NDE categorized by “model” data and stability class

Constants	All Data	“Model” Data	Model: A-C	Model: D	Model: E-G
p	1.11	1.12	0.88	1.28	0.57
q	0.68	0.11	-0.41	0.93	0.33
C_1	0.55	0.11	0.02	1.20	0.37
Total Tests	**446**	**63**	**30**	**12**	**21**

While the original NDE validated with all of the data showed trends in stability class, no noticeable trends are seen when constants are determined from “model” data by stability class with the original non-dimensionalized equation. While near field and far field showed trends with all of the data, the “model” data does not exceed 10,000 seconds so is unable to be classified into near field and far field for model validation.

2.5.1.3 Summary of Original NDE

An original non-dimensionalized equation was developed to model the effects of along-wind dispersion. Different classifications or grouping of the data was performed to determine optimal constants. Many of the variations did not provide good models where other variations of the NDE model proved better. Due to a small sample size of certain tests, a non-parametric confidence interval was chosen to evaluate the parameters of all categories. This was evaluated with $\alpha = \frac{\sigma_x(predicted)}{\sigma_x(data)}$. If $\alpha < 1$, then the model is under predicting σ_x values and if $\alpha > 1$, then the model is over predicting σ_x values. α values are best when closest to 1. Shown below in Table 14 are the most promising parameterizations of the NDE with their overall equation, 90% confidence interval, and range of data.

Table 14. 90% Confidence intervals determined from non-parametric statistical analysis

Parameterization (quantity of tests)	Equation	90% Confidence Interval	Range
Hanna (446)	$\sigma_x = 2u_* t$	$1.63 \leq \alpha \leq 1.88$	26%
Original NDE (All Data - 446)	$\frac{\sigma_x}{x} = 0.55\left(\frac{ut}{x}\right)^{1.11}\left(\frac{u_*}{u}\right)^{0.68}$	$1.17 \leq \alpha \leq 1.36$	19%
Original NDE (“Model” Data - 63)	$\frac{\sigma_x}{x} = 0.108\left(\frac{ut}{x}\right)^{1.12}\left(\frac{u_*}{u}\right)^{0.11}$	$0.97 \leq \alpha \leq 1.14$	17%
10,000s: NDE near field (315)	$\frac{\sigma_x}{x} = 4.92\left(\frac{ut}{x}\right)^{0.72}\left(\frac{u_*}{u}\right)^{1.44}$	$1.00 \leq \alpha \leq 1.16$	16%
10,000s: NDE far field (131)	$\frac{\sigma_x}{x} = 0.42\left(\frac{ut}{x}\right)^{1.14}\left(\frac{u_*}{u}\right)^{0.59}$	$1.24 \leq \alpha \leq 1.52$	28%

Overall, all of the original non-dimensionalized equations provided better predictions than Hanna’s equation from the α values closer to 1 and smaller ranges of the 90% confidence intervals. The original non-dimensionalized equation using all data provided an improvement by 7% range and provided predictions closer to the original σ_x values. The original non-dimensionalized equation using only the quality “model” data had a 90% confidence interval closer to the original values and a range 9% tighter than Hanna's equation. The near-field and far-field parameterization also proved well. Visually, the near field and far field fit is the best from 10,000 seconds and larger. This last model is able to capture the fit of the data much better than Hanna's equation.

2.5.2 Lagrangian NDE

From prior parameterizations discussed with the original NDE, the most promising results separated the data into near field and far field. A value of 10,000 seconds was chosen for this arbitrary value from Wilson's publication on Lagrangian Timescale[45]. A new non-dimensionalized equation incorporating Wilson's value for Lagrangian Timescale, t_L , was developed and implemented into the NDE model. The $\left(\frac{u_*}{u}\right)$ tem is kept to incorporate the friction velocity, wind speed, and indirectly the stability class. The Lagrangian Timescale, t_L is incorporated in the $\left(\frac{t}{t_L}\right)$ term. The left side resulted in $\frac{\sigma_x}{ut_L}$ for non-dimensionalization of the entire equation. This Lagrangian NDE is shown below in Equation (47)

$$\frac{\sigma_x}{ut_L} = C_1\left(\frac{t}{t_L}\right)^p\left(\frac{u_*}{u}\right)^q \tag{47}$$

with t_L = 10,000 sec. This new correlation for the Lagrangian NDE incorporates the Lagrangian time scale from prior testing and will be parameterized to determine the optimal relationship for predicting the along-wind dispersion coefficient. For analysis of this equation, the non-parametric statistical analysis will be performed to determine confidence intervals in addition to visual parameterizations.

2.5.2.1 All Data Sets

As an initial step, determination of the constants using all of the data was performed. The constants from this parameterization are shown below in Table 16.

Table 15. Constants determined for Lagrangian NDE with all data

Constants	All
p	1.01
q	0.66
C_1	0.51
Total Tests	**446**

The constants prove similar to the original non-dimensionalized equation using all of the data. A visual representation of the Lagrangian non-dimensionalized equation using all data is shown below in Figure 18.

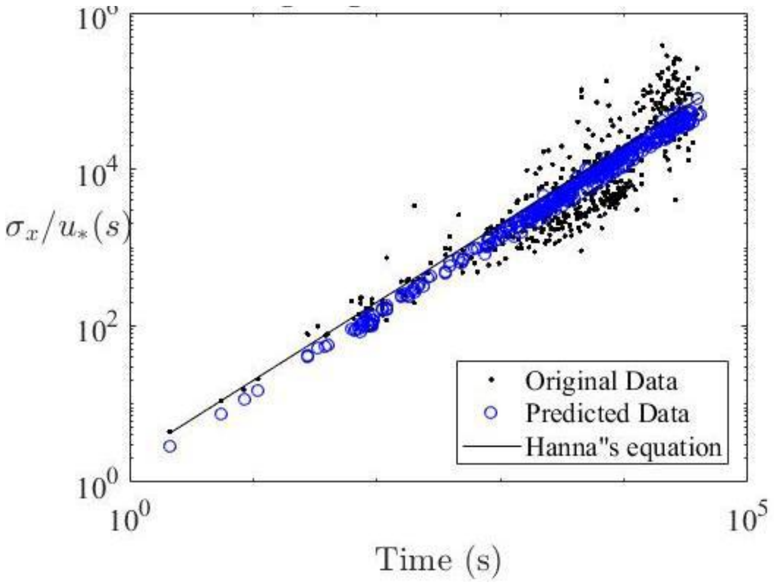

Figure 18. Time (s) vs. σ_x/u_* (s) as a function of the original data, Lagrangian NDE predictions using all 446 data points, and Hanna's predictions

Visually, the fit of the Lagrangian NDE is comparable to the original NDE shown in Figure 15. All of the predicted data is below Hanna's equation which fits the data better between 1,000 and 100,000 seconds but can be improved upon overall.

2.5.2.2 "Model" Data Sets

Determinations of the constants using only the "model" data of Marchwood, KitFox ERP, KitFox URA, DTRA phase 1, Hanford, and Dipole Pride tests were performed with improvement seen in the original NDE. The constants from this parameterization are shown below in Table 16.

Table 16. Constants determined for Lagrangian NDE with "model" data

Constants	All	Model
p	1.01	0.94
q	0.66	0.13
C_1	0.51	0.10
Total Tests	**446**	**63**

The results of the Lagrangian NDE with "model" data shows smaller constants when compared to the Lagrangian non-dimensionalized equation with all data. The constants determined with the "model" data show that the terms on the right-hand side of the equation have less of an impact on the along-wind dispersion coefficient as compared to all of the data. The Lagrangian NDE fit with "model" data is shown below in Figure 19 to see a visual representation of the model validated with "model" data.

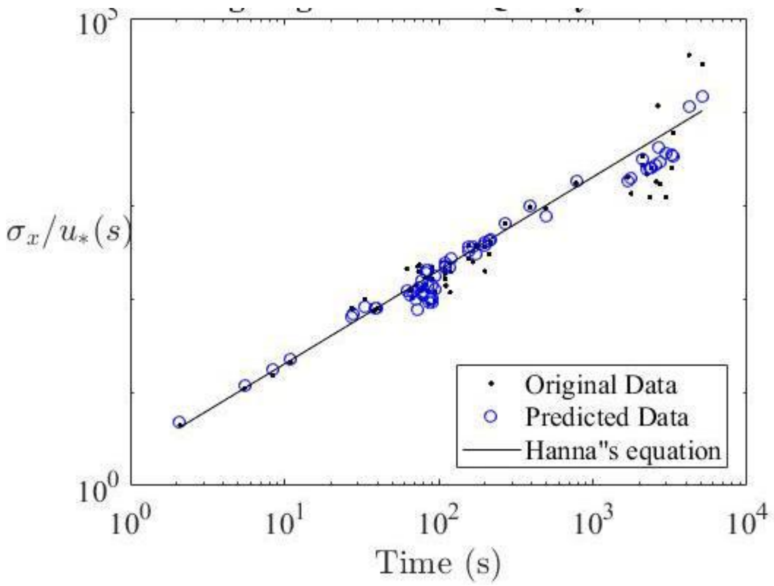

Figure 19. Time (s) vs. σ_x/u_* (s) as a function of the original data, Lagrangian NDE predictions using only “model” data points, and Hanna’s predictions

The Lagrangian non-dimensionalized equation with constants derived from “model” data shows a better fit for the “model” data. The predicted data is observed to have different values for the same time capturing the spread of data better. This spread of predicted data could not be achieved with Hanna’s equation visually showing a better fit for the “model” data for along-wind dispersion.

2.5.2.3 “Model” Data Sets by Stability Class

As prior performed with the original NDE, parameterization by “model” data and stability class was determined due to prior trends. The results from this parameterization are shown below in Table 17.

Table 17. Constants determined for Lagrangian NDE with "model" data with stability class

	All Data	All "Model" Data	Model: A-C	Model: D	Model: E-G
p	1.01	0.94	0.75	0.93	1.20
q	0.66	0.13	1.03	0.96	0.76
C_1	0.51	0.10	0.59	1.11	2.23
Total	446	63	30	12	21

From this parameterization, very noticeable trends appeared in the constants. An increase is shown in the constant *p* as stability class transitions from the convective boundary layer to the stable boundary layer. The constant *q* decreases over the same transition. C_1 also increases over this transition. A visual representation of the Lagrangian NDE by stability class compared with original data can be seen below in Figure 20.

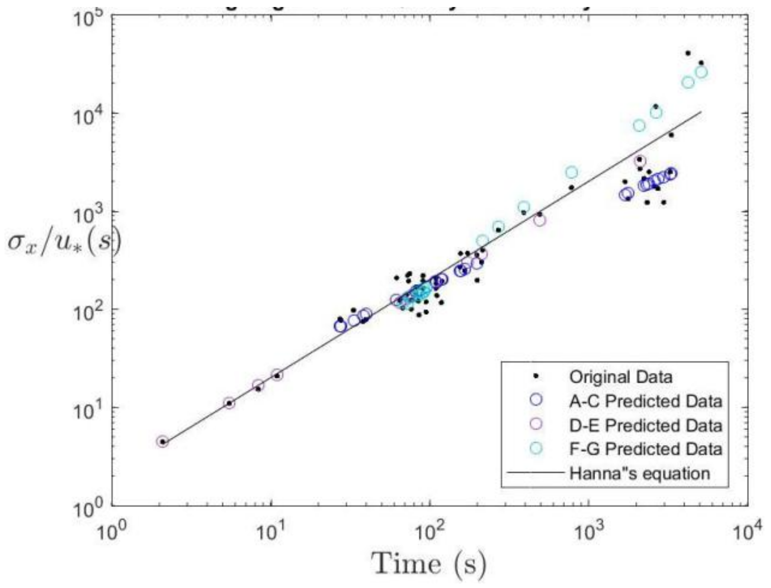

Figure 20. Time (s) vs. σ_x/u_* (s) as a function of the original data, Lagrangian NDE predictions with "model" data points and stability class, and Hanna's predictions

This graph shows only the "model" data with the Lagrangian non-dimensionalized fit using "model" data by stability class. This NDE model shows an improved fit of the Lagrangian NDE incorporating stability class. The deviation of the original data both above Hanna's line and below the line is able to be captured appropriately. The expansion of this equation to all of the available data is plotted below in Figure 21.

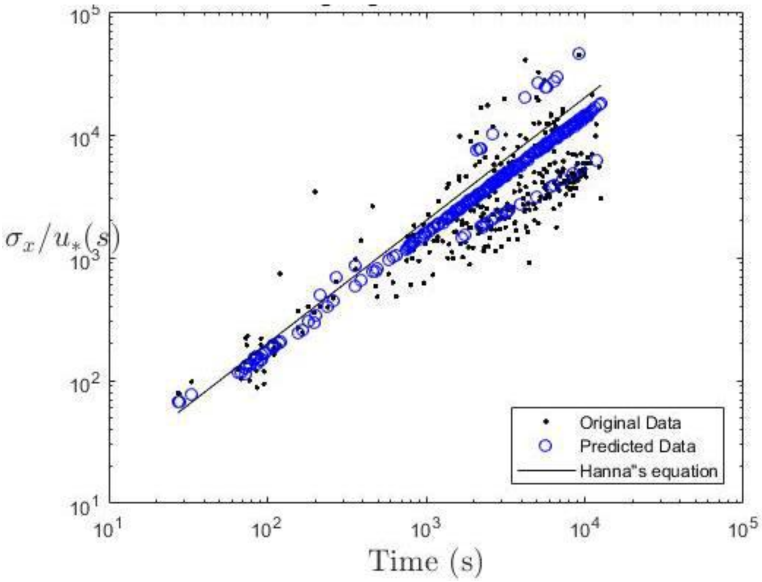

Figure 21. Time (s) vs. σ_x/u_* (s) as a function of the original data, Lagrangian NDE predictions with "model" data points and stability, and Hanna's predictions

While the constants determined with the Lagrangian non-dimensionalized equation with "model" data by stability class are a great fit for the "model" data, they are not a great fit for all of the data. This equation is an improvement compared to Hanna's equation as well as the original NDE due to the spread of the prediction that fit the data both above and below Hanna's prediction but can be improved upon.

2.5.2.4 Summary of Lagrangian Non-Dimensionalized Equation

The Lagrangian non-dimensionalized equations proposed provides improvements on the overall predictions for the along-wind dispersion coefficient. A non-parametric confidence interval was chosen to evaluate the outcome of each model with $\alpha = \frac{\sigma_x(predicted)}{\sigma_x(data)}$ with optimal values closest to 1. Shown below in Table 18 are the Lagrangian NDEs with their overall equations with constants, 90% confidence interval, and range of data.

Table 18. 90% Confidence intervals determined from non-parametric statistical analysis

Parameterization (total tests)	Equation	90% Confidence Interval	Range
Hanna (446)	$\sigma_x = 2u_*t$	$1.63 \leq \alpha \leq 1.88$	26%
Lagrangian NDE (all - 446)	$\frac{\sigma_x}{ut_L} = 0.51(\frac{t}{t_L})^{1.01}(\frac{u_*}{u})^{0.66}$	$1.17 \leq \alpha \leq 1.36$	19%
Lagrangian NDE (“Model” - 63)	$\frac{\sigma_x}{ut_L} = 0.10(\frac{t}{t_L})^{0.94}(\frac{u_*}{u})^{0.13}$	$0.99 \leq \alpha \leq 1.14$	15%
Lagrangian NDE (“Model” by Stability Class – 63)	$\frac{\sigma_x}{ut_L} = C1(\frac{t}{t_L})^p(\frac{u_*}{u})^q$	$0.96 \leq \alpha \leq 1.09$	13%

The Lagrangian non-dimensionalized equation shows improvement when compared to both Hanna’s equation and the original non-dimensionalized equation. The original NDE with constants determined from all data is comparable to the Lagrangian NDE with constants determined from all data. The effects of the equations start to differ when the constants are determined from both “model” data and “model” data with stability class. The Lagrangian NDE has as a tighter range for both “model” data and “model” data by stability class than the original NDE and Hanna’s equation. The α values are also closer to its optimal value of 1 with the Lagrangian NDEs compared to the original NDE and Hanna’s equation.

2.5.3 Theoretical NDE

Similar to the Original NDE, the Theoretical NDE takes into account the friction velocity and time twice whereas the Original NDE takes these parameters into account only once. The left side of the equation is non-dimensionalized by these parameters instead of the distance in the original NDE. This arrangement non-dimensionalized with the parameters discussed in the theoretical derivations makes the equation slightly different than the original NDE. The overall theoretical NDE is shown below in equation (48).

$$\frac{\sigma_x}{u_* t} = C(\frac{u_*}{u})^{p_1}(\frac{u}{u_e})^{p_2} \tag{48}$$

where p_1, p_2, and C are all dimensionless constants. Similar to the original NDE, the $\left(\frac{ut}{x}\right)$ or $\left(\frac{u}{u_e}\right)$ term accounts for wind speed, u, time, t, and distance, x. The $\left(\frac{u_*}{u}\right)$ term takes into account stability class indirectly through wind speed and friction velocity. A multi-variable regression analysis was performed with all of the data classified by stability class to determine the constants for C, p_1, and p_2. The results of this analysis are shown below in Table 19.

Table 19. Values for *C*, *p_1*, and *p_2* of theoretical NDE

Constants	AB	C	D	EF
C	0.034	0.460	0.238	0.071
P_1	-1.262	-0.421	-0.706	-1.235
P_2	-1.782	-0.0828	-0.652	-1.553
tests	**5**	**24**	**40**	**20**

From Table 19, all values of p_1 and p_2 are negative. All values of C are positive. Beyond being negative or positive, there are no trends in the values within the constants. The predicted data with this theoretical NDE is visually shown below in Figure 22.

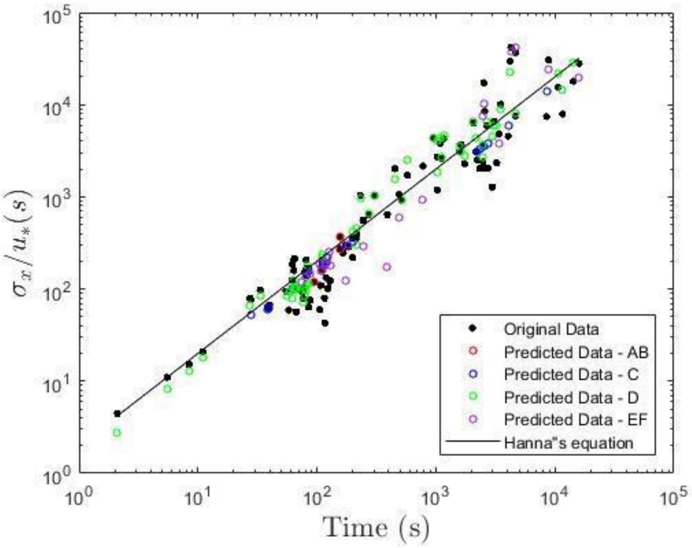

Figure 22. Time (s) vs. σ_x/u_* (s) as a function of the original data by theoretical NDE and Hanna's predictions

Figure 22 shows σ_x/u_* vs. time for the original data, predicted data from the Theoretical NDE, and Hanna's equation. From the figure, many of the points are shown to overlap with the original data. A statistical comparison of how the predicted data with the theoretical NDE and Hanna's equation are shown with MG VG values in Table 20.

Table 20. MG VG values for theoretical NDE

	AB	C	D	EF	All
MG – NDE	1.000	0.935	0.958	0.928	**0.946**
VG – NDE	1.000	1.180	1.155	1.632	**1.149**
MG - Hanna	0.827	0.752	0.950	0.818	**0.908**
VG - Hanna	1.095	1.301	1.335	1.974	**1.331**

From Table 20, the theoretical NDE is an improved fit over Hanna's equation for all stability classes and overall data due to the MG and VG values being closest to 1. Overall, the theoretical NDE classified by stability class is able to model the data better than Hanna's equation based on the visual representation in Figure 22 and MG VG values closer to 1 in Table 20. Although the theoretical NDE performs better than Hanna's equation, the input data can limit the use of the theoretical NDE if it is not available, such as the effective wind speed, u_e.

2.5.4 Condensed NDE

The previous non-dimensionalized equations show improvement when compared to Hanna's equation. The major trends seen with the original NDE was an improvement when the time was split into the near field and far field. This lead to the Lagrangian NDE. From the Lagrangian NDE, the improvement was seen when "model" data was used with stability class. Another non-dimensionalized equation was developed to incorporate both the trends in stability class and time. A condensed non-dimensionalized equation has been developed to incorporate trends of stability class or $(\frac{\boldsymbol{u_*}}{\boldsymbol{u}})$ and have all input parameters available. This condensed non-dimensionalized equation is shown below in Equation (49)

$$\frac{\sigma_x}{u_* t} = C_1 (\frac{u_*}{u})^{\mathrm{p}} \tag{49}$$

Where stability class is taken into effect with $(\frac{\boldsymbol{u_*}}{\boldsymbol{u}})$ term on the right hand side. σ_x as a function of u_* and *t* is taken into account on the left hand side in this condensed non-dimensionalized equation. "Model" data was used to develop the constants. A p-value was determined to be 0.995 due to the averaged individual constants solved by "model" data and stability class for both C_1 and p values. The overall equation for the final NDE is shown below in equation (50)

$$\frac{\sigma_x}{u_* t} = C_1 (\frac{u_*}{u})^{0.995} \tag{50}$$

Where C_1 are the constants determined from each grouping of stability class, similarly performed in all other NDEs. These values for constants are shown below in Table 21 with their respective MG VG values.

Table 21. 90% Confidence intervals determined from non-parametric statistical analysis

Constants	AB	C	D	E	FG	All	Hanna
C_1	0.068	0.071	0.086	0.100	0.142	-	-
p	0.995	0.995	0.995	0.995	0.995	-	-
Total Tests	**9**	**18**	**21**	**3**	**12**	**63**	**63**
MG	0.916	0.905	0.995	1.001	0.966	0.953	0.850
VG	1.150	1.171	1.067	1.002	1.236	1.134	1.357

The trend observed with the constants show that as the stability class transitions from the convective boundary layer to the stable boundary layer, the constant value increases. In Table 21, the MG VG values for the “model” data are determined for Hanna’s equation, all of the “model” data with stability class, and each of the individual stability classes. These MG VG values show that each of the condensed non-dimensionalized equation’s predictions are better than predictions by Hanna’s overall equation. A visual representation of the data predicted by the condensed NDE is shown below in Figure 23.

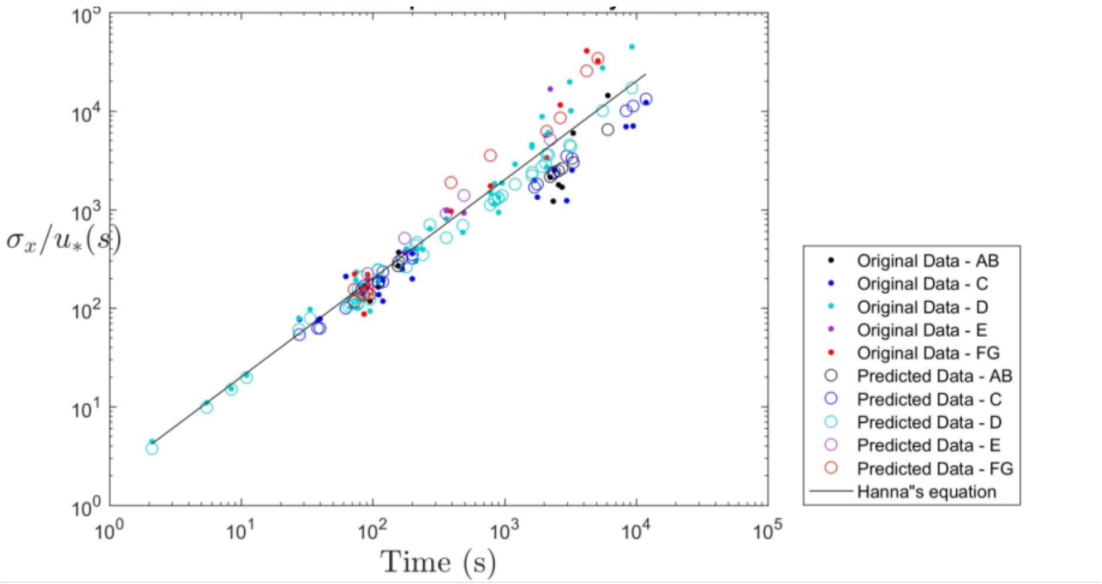

Figure 23. Time (s) vs. σ_x/u_* (s) as a function of the original data by stability class, final NDE predictions by "model" data with stability class, and Hanna's predictions

This figure shows all of the model data with the original data, predicted data by the final non-dimensionalized equation, and Hanna's prediction. The condensed non-dimensionalized equation by stability class is able to capture the trends evidenced in Figure 23 appropriately.

2.5.5 Final NDE

Throughout the analysis, data were checked and doubled checked to make sure all results are consistent. OLAD-van tests were revisited and decided to be included in the final quality data to be used in model validation. Note the OLAD-plane tests were still excluded due to their release in the upper boundary layer. This inclusion of the OLAD-van tests resulted in a total of 89 tests to be used as "validation" data for validating the constants. Kit Fox SSR tests were also accumulated at this time, but not included in the validation data due to inconsistency in the data analysis. The methods reported for determination of σ_x did not match with the values reported for σ_x. A final

NDE was developed with the quality “Validation” data and is reported below in the final NDE sections.

2.5.5.1 Additional Data for Model Validation and Trends in Stability Class

In addition to “validation” data inclusion, stability class was scrutinized. From previous NDEs categorized by stability class, trends were seen in the constants for the respective stability classes. This is expected because stability class is known to have an effect on atmospheric dispersion. To see the effect of the stability class on the along-wind dispersion coefficient, the “validation” data was color-coded by stability class. Overall trends in the original data by stability class are shown below in Figure 24.

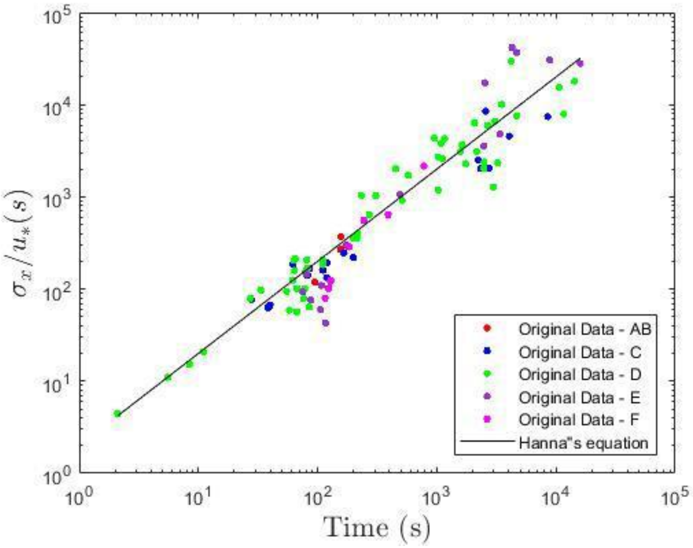

Figure 24. Time (s) vs. σ_x/u_* (s) as a function of the original data by stability class and Hanna’s predictions

From Figure 24, noticeable trends are seen between the different stability classes. Stability Classes AB and C do not have as steep of a slope as the line predicted by Hanna. Stability Class D spreads out both above and below the line predicted by Hanna, but of the similar slope. Stability classes E and F have a slightly steeper slope than the line predicted by Hanna. These trends show that the stability class has an effect on the overall along-wind dispersion coefficient with respect to the slope of the data trends. Stability class is taken into account with the $(\frac{\boldsymbol{u_*}}{\boldsymbol{u}})$ term. Determining a constant as a function of the stability class is believed to be the most promising option and has showed success with previous NDEs.

2.5.5.2 Final NDE by Stability Class

Figure 24 shows noticeable trends in the stability class. This supports the $(\frac{\boldsymbol{u_*}}{\boldsymbol{u}})$ term from the theoretical non-dimensionalized equation. The $\left(\frac{ut}{x}\right)$ or $\left(\frac{u}{u_e}\right)$ term in the theoretical non-dimensionalized equation accounts for wind speed, u, time, t, and distance, x. This term is not as applicable due to the availability and predictability of the effective wind speed, u_e. Due to limitability of the effective wind speed and decreased impact of the effective wind speed, the $\left(\frac{u}{u_e}\right)$ term is removed from the equation resulting in the condensed NDE shown in Equation (51). Although a term is excluded, the condensed NDE still shows improved modeling of the along-wind dispersion coefficient. The quality "validation" data was used to determine the constants for this final non-dimensionalized equation through a multi-variable regression analysis. An overall value for the exponent was determined to be -0.5 due to individual constants with the validation data. This new equation is shown below

$$\frac{\sigma_x}{u_* t} = C_1 (\frac{u_*}{u})^{-0.5} \tag{51}$$

where values of C_1 are determined for each stability class. With the OLAD-van data included in the quality data, the constant changes from previous value determined with the condensed NDE and 63 "model" data points. A single variable regression analysis is used with the data classified into their respective stability classes and p = -0.5 to determine the values for C_1. The values for the constants as a function of stthe ability class are shown below in Table 22 with their respective quantity of tests.

Table 22. Values for C_1 with p = -0.5

	AB	**C**	**D**	**E**	**F**	**All**
C_1	0.311	0.339	0.408	0.429	0.576	0.408
Tests	**5**	**24**	**40**	**15**	**5**	**89**

Table 22 shows clear trends in the C_1 values as a function of the stability class when the p constant is set to a value of -0.5. The trend observed with the C_1 constant shows that as the stability class transitions from the convective boundary layer to the stable boundary layer, the C_1 value increases. The average value of all of the tests for the constant C_1 is 0.408. This 0.408 value is consistent with a neutral stability class which aligns with models that use neutral stability if the stability class is unknown. A visual representation of the final NDE classified by stability class is shown below in Figure 23.

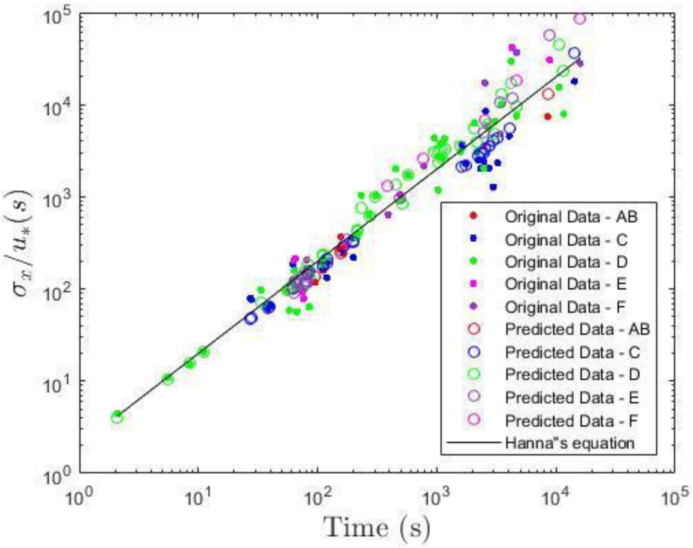

Figure 25. Time (s) vs. σ_x/u_* (s) as a function of the original data by stability class, final NDE predictions classified by stability class, and Hanna's predictions

Figure 25 shows the original data by stability class, predicted data by the final non-dimensionalized equation classified by stability class, and Hanna's prediction. This visually shows that this non-dimensionalized equation is able to capture the trends evidenced in the stability classes appropriately. A statistical comparison of how the predicted data with the NDE and Hanna's equation are shown with MG VG values below in Table 23.

Table 23. MG VG values for NDE by stability class with p = -0.5

	AB	C	D	EF	All
MG – NDE	0.939	0.925	0.889	1.024	**0.931**
VG – NDE	1.096	1.240	1.178	1.458	**1.248**
MG - Hanna	0.728	0.713	1.011	1.217	**0.942**
VG - Hanna	1.234	1.418	1.296	1.484	**1.365**

Overall the MG VG values for all the validation data points are similar for both the final NDE MG VG values and Hanna's equations MG VG in Table 23. Classifying the data points into their respective stability classes shows that the MG VG values for the NDE are able to model the data more appropriately than Hanna's equation. A parity plot is shown below in Figure 26 for another representation of how the predicted data compares with the original data and shows how well this NDE model collapses the experimental data.

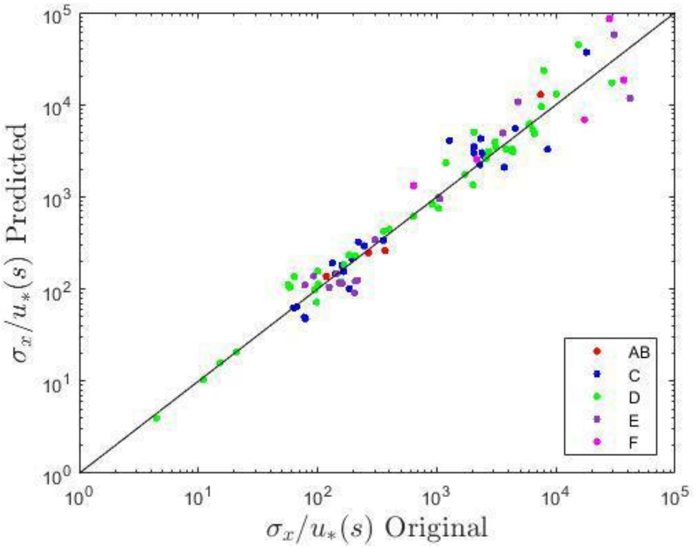

Figure 26. σ_x/u_* (s) for the original data vs. σ_x/u_* (s) for the NDE by stability class for all of the quality data with a reference line

Figure 26 shows that the predicted data falls along the reference line of what the data should be if equivalent to the original data. The data is collapsed tighter between 0 and 10,000 seconds. There is a bit larger spread of the data after 10,000 seconds. The final NDE by stability class does not consistently over or under predicting the data which is good. Compared to Hanna's equation, shown in a parity plot in Figure 14, the final NDE by stability class is a better model due to the tighter and more even distribution of the data points.

Overall, the NDE by stability class is able to model the data better than Hanna's equation based on the visual representation in Figure 25, MG VG values closer to 1 in Table 23, and collapse the data better in the parity plot in Figure 26.

2.5.5.3 Final NDE by Stability with Monin-Obukhov Length

While the final NDE by stability class is a better fit than Hanna's along-wind dispersion equation and previous NDEs, it is believed it can be improved upon due to the trends observed in the C_1 constants in Table 21. These trends show that as the stability class transitions from the convective boundary layer to the stable boundary layer, the C_1 value increases. This final proposed NDE takes into account the Monin-Obukhov Length, λ, to model these trends. The final NDE was used as the basis for the NDE with Monin-Obukhov Length. The final NDE is shown again in equation (52) but with a different value for C_1 shown in equation (53)

$$\frac{\sigma_x}{u_* t} = C_1 \left(\frac{u_*}{u}\right)^{-0.5} \tag{52}$$

$$C_1 = C_{s/c} - \left(C_{s/c} - C_d\right) * [\exp\left({}^{\lambda_{s/c}}/_{\lambda}\right)] \tag{53}$$

where $C_{s/c}$ and $\lambda_{s/c}$ are dimensionless constants. Equation (53) is able to make the C_1 values a function of the Monin-Obukhov length which directly relates to stability. Equation (53) is arranged so that at a neutral boundary layer with a Monin-Obukhov length of 10,000, the constants cancel out leaving the C_1 value equal to 0.408. This value is consistent with the C_1 value for stability class D from Table 23. This arrangement allows for a smooth transition between the convective boundary layer with negative Monin-Obukhov lengths and stable boundary layer with positive Monin-Obukhov lengths. A smooth transition for all Monin-Obukhov lengths is desired from a modeling perspective over individual stability classes. The values for the constants determined from equation (53) with a multi-variable regression analysis are shown below in Table 24.

Table 24. Values for $C_{s/c}$ and $\lambda_{s/c}$ constants with p = -0.5

	Negative λ	Positive λ	*D*	All
$C_{s/c}$	0.313	0.408	0.408	
$\lambda_{S/C}$	186.360	-0.008		
P	-0.5	-0.5	-0.5	
tests	**32**	**51**	**40**	**83**

Table 24 shows the constants for $C_{s/c}$ and $\lambda_{s/c}$ for the convective and stable boundary layers. There are not obvious trends in the data. The total tests show a slight decrease in amount compared to the previous NDEs due to inclusion of the Monin-Obukhov length. Only 83 data points out of the 89 included Monin-Obukhov length to account for this difference. A visual representation of the Final NDE with Monin-Obukhov length predicted data is shown below in Figure 27.

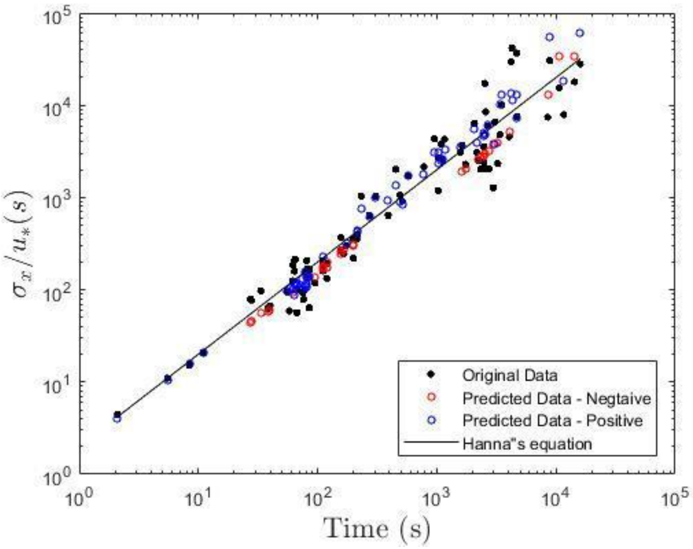

Figure 27. Time (s) vs. $^{\sigma_x}/_{u_*}$ (s) as a function of the original data, NDE predictions classified by Monin-Obukhov Length, and Hanna's predictions

Figure 27 shows the original data, data predicted with the final with Monin-Obukhov Length by convective and stable boundary layer, and Hanna's prediction. The slope of the NDE for a negative Monin-Obukhov length is less than Hanna's prediction which aligns with Figure 24 for unstable stability classes or the convective boundary layer. The slope of the NDE for a positive Monin-Obukhov length is greater than Hanna's prediction which also aligns with Figure 24 for stable stability classes. A statistical comparison of how the predicted data with the NDE and Hanna's equation are shown with MG VG values below in Table 25.

Table 25. MG VG values for NDE by Monin-Obukhov Length

	Negative λ	**Positive λ**	**All**
MG – NDE	0.978	1.019	**1.001**
VG – NDE	1.247	1.318	**1.286**
MG - Hanna	0.785	1.117	**0.957**
VG - Hanna	1.446	1.424	**1.433**

The MG VG values for all of the data points in Table 25 are improved for the final NDE with Monin-Obukhov Length compared to Hanna's equation. Classifying the Monin-Obukhov length by negative and positive values shows that the NDE has improved geometric means and geometric variances compared to Hanna's equations for both the convective and stable boundary layers. A parity plot is shown below in Figure 28 for an additional visual representation of how the predicted data with this NDE compares with the original data.

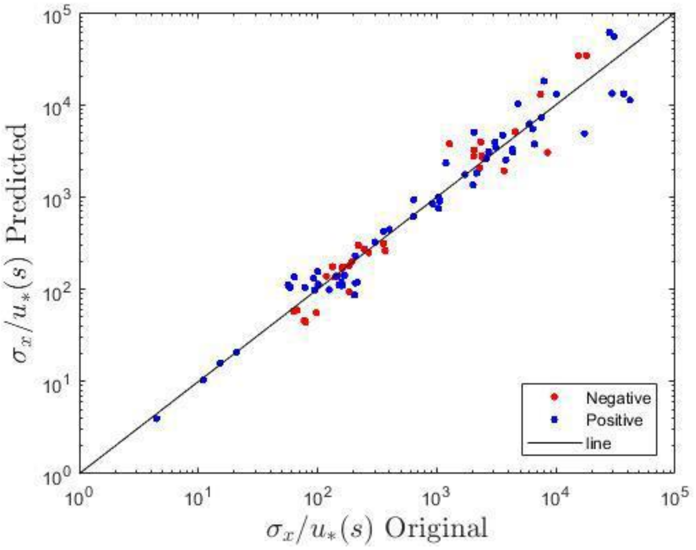

Figure 28. σ_x/u_* (s) for the original data vs. σ_x/u_* (s) for the NDE by stability class for all of the quality data with a reference line

Figure 28 shows that the predicted data falls along the reference line of what the data should be. The data is collapsed equally throughout all time. Compared to Hanna's equation, shown in a parity plot in Figure 14, the NDE with Monin-Obukhov length better predicts σ_x values compared to Hanna's equation due to the tighter grouping around 100 seconds and has more even distribution of data points greater than 100 seconds.

Similar to the NDE by stability class, the NDE with Monin-Obukhov length is an improved model based on the visual representation in Figure 27, MG VG values closer to 1 in Table 25, and collapse of the data with the parity plot in Figure 28.

2.6 Summary

Multiple non-dimensionalized equations (NDEs) have been developed incorporating prior derivations of the along-wind dispersion coefficient and available data. The theoretical NDE provided improved predictions compared to Hanna's equation, which is an improved fit for the overall data. Although this NDE is visually and statistically better than Hanna's equation, the model itself is comprised of four separate equations based on stability class and requires the effective wind speed, which may not always be available. Additional NDEs were developed without the effective wind speed and classified by the stability class, labeled as the Final NDEs. Both of these Final NDEs proved better than Hanna's equation. The main difference between the two final NDEs is whether or not Monin-Obukhov length is available. If the Monin-Obukhov length is available, equations (52) and (53) are recommended to be used with values for constants from Table 24. These equations provide one continuous NDE throughout all conditions. If Monin-Obukhov length is not available, equation (51) is recommended with values for constants from Table 21. Both of the Final NDEs are able to capture the spread of data better than Hanna's equation due to additional parameters and the inclusion of stability class.

3 Experimental Program

3.1 Introduction

An experimental program in the ultra-low speed wind tunnel at the Chemical Hazards Research Center was established to determine an appropriate along-wind dispersion coefficient from the concentration-time histories of finite-duration releases under different test conditions including wind speed, release duration, distance downwind, and more. Descriptions of the equipment and facility, experimental program, analysis, and results of the finite-duration releases are presented below.

3.2 Equipment and Facility

The tunnel has a working section of 24 m in length with a 6.1 m x 2.1 m cross-section and wind speeds from 0.34 m/s to 1.1 m/s. The LDV system allows for velocity profiles to be measured in 3 directions. A constant stress layer of 40cm produced with modified Irwin spire arrangement and surface roughness ensures that all tests performed were within the constant stress layer. The FID system also allows for concentration-time histories to be accurately measured. An area source developed specifically for this program provides repeatable release durations at constant rates. All of these capabilities provide an optimal testing facility for finite-duration releases. In this section, the facility will be described as well as the equipment with necessary modifications.

3.2.1 Ultra-Low Speed Wind Tunnel

The Chemical Hazards Research Center houses an ultra-low-speed wind tunnel to model the effects of hazardous gases in the atmosphere. The wind tunnel has a working section of 24 m in length with a 6.1 m x 2.1 m cross-section. The wind tunnel has an established boundary layer of 60 cm and a constant stress layer of about 10cm with one layer of spires. The tunnel was designed to run at wind speeds less than 2 m/s for scalability to atmospheric conditions, specifically for denser-than-air gases but applicable for neutrally buoyant gases as well[46]. The wind tunnel is a "push through" wind tunnel where the air is pushed through the working section in contrast with many tunnels that are pull through. The tunnel is centrally located in the room with adequate spacing on either side to provide uniform flow around and through the wind tunnel within the isolated room. A control room adjacent to the wind tunnel provides observation and control of equipment during testing without disrupting the flow. A floor plan of the wind tunnel with its adjacent control room is shown below in Figure 29.

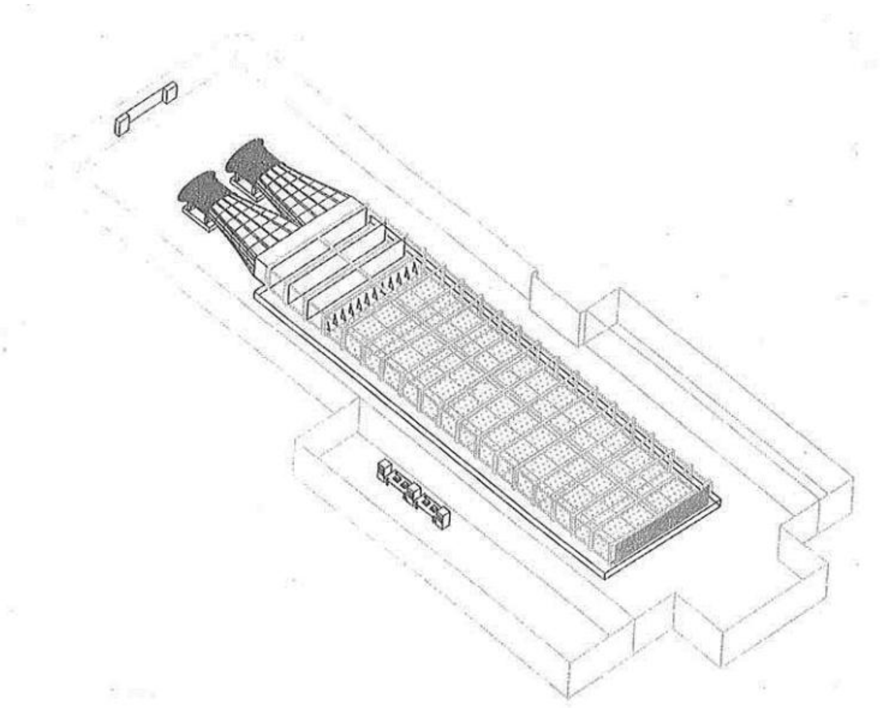

Figure 29. Floor plan of the wind tunnel at the CHRC[47]

In this floor plan, all tunnel characteristics discussed above can be seen. The symmetry of the wind tunnel was found necessary for uniform flow in the tunnel. Not shown in the figure are three baffles adjacent to the wind tunnel in alignment with the straightening section of the wind tunnel. These baffles were tuned to ensure uniform flow distribution in the wind tunnel.

3.2.1.1 Fans and Air Flow

Two adjustable pitch vane-axial fans (Buffalo Forge Company Model 72D5 ADJUSTAX) built by the Buffalo Forge Company are used to push air through the working section of the wind tunnel. The 1.8 m diameter, 75 horsepower fans are controlled with a Fenner M-Trim speed controller optimizing the master-and-slave method (Eaton Company DYNAMATIC Model VT-323). This model uses eddy-current drives to control the speed of each fan within 0.5 % of the maximum speed. Dolan-Jenner optical sensors were used to measure the fan rotation speed of each fan.

From the outlet of each fan, transition ducts carry wind from the circular output of the fans into a rectangular input at the front of the wind tunnel. These ducts are comprised of 0.3 cm thick polycarbonate plastic sheets connecting the end of the fan to the working section of the wind tunnel. Honeycomb at the entrance of the wind tunnel provides a pressure drop of the flow for flow straightening. This honeycomb has 1.2 cm cell size with 10.1 cm thick plastic-impregnated Kraft paper. After the honeycomb, 4 seamless fiberglass screens are located at distances of 1.0 m, 1.1 m, 2.0 m, and 2.1 m downwind for additional flow straightening. After the air has passed through the circular fans, rectangular input, honeycomb, and 4 screens, it is uniform and dispersed across the full cross-section of the wind tunnel.

3.2.1.2 Boundary Layer and Surface Roughness

Fourteen Irwin spires placed at a distance of 30 cm downwind the last screen, were used to generate a turbulent boundary layer. These spires are comprised of 0.36 cm thick acrylic and are 92.7 cm in height, 13.2cm at the base, and 23.2cm in length as shown in Figure 30.

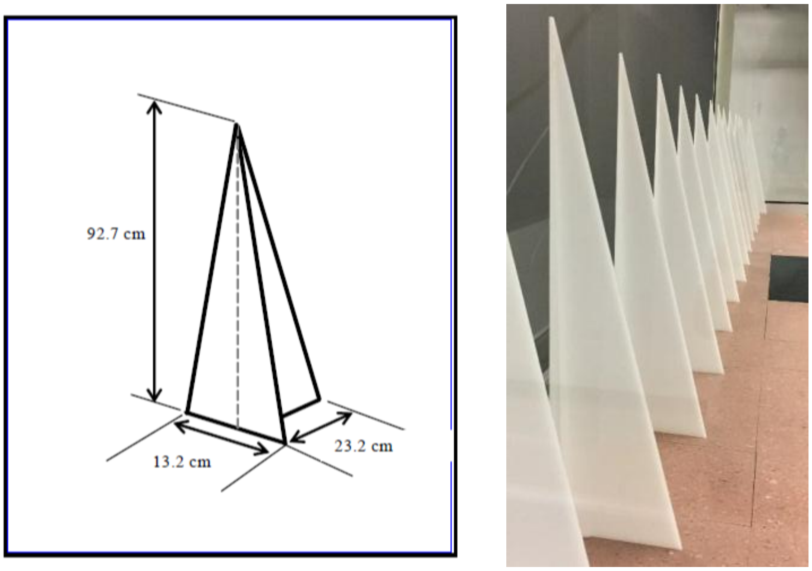

Figure 30. Drawing of Irwin Spires (left)[47] and picture of Irwin Spires in wind tunnel (right)

Figure 30 shows the physical dimensions of the Irwin spires (left) and the physical placement of the Irwin spires in the wind tunnel (right) with 46.3cm between each spire and 6.6cm between the spires and the wall. The boundary layer is established through these Irwin Spires for a fully developed boundary layer of 60 cm in depth after a distance of 6m downwind[48]. In addition to the Irwin spires, aluminum angles were placed on the floor of the wind tunnel to provide a surface roughness in the wind tunnel. The aluminum angles are 3.81 cm in height, width, and length with an angle of 90^{0}. They are placed at a spacing of 30.5 cm between the centers of each roughness piece, using a template. A drawing showing the dimensions of each aluminum angle and their physical distribution in the wind tunnel are shown below in Figure 31.

Figure 31. Physical placement of aluminum angles for surface roughness in wind tunnel

A turbulent boundary layer with a height of 10 cm was obtained using one layer of Irwin spires and aluminum angles. The boundary layer is considered fully developed 6 m downwind of the 1 m tall spires. The remaining portion of the wind tunnel downwind of this boundary layer generation region served as the working section of the tunnel.

3.2.1.3 Validation of Uniform Flow (Visual)

Flow is expected to be uniform through the wind tunnel, but some variation was observed. Flow around the tunnel is desired because of building constraints which have an effect on flow in the tunnel. To achieve uniform flow in the wind tunnel, three baffles were installed on the starboard side of the wind tunnel in alignment with the straightening section. The angles in which these baffles were positioned needed to be determined for uniform flow in the wind tunnel. Validation of the uniform flow was visually achieved using a water-based fog solution fed through a Rosco 1500 fog machine and house-made fog chiller into PVC piping through the center of the wind tunnel directly behind the Irwin spires from a point source. Black plastic was fixed on the floor of the wind tunnel floor for improved visualization of the white smoke. Blue painters tape was secured to the black plastic in 61 cm x 61 cm increments for quantified visualization. Multiple arrangements of the three baffles at different angles were tested to achieve uniform flow through video taken in the wind tunnel. A screenshot of uniform flow is shown below in Figure 32.

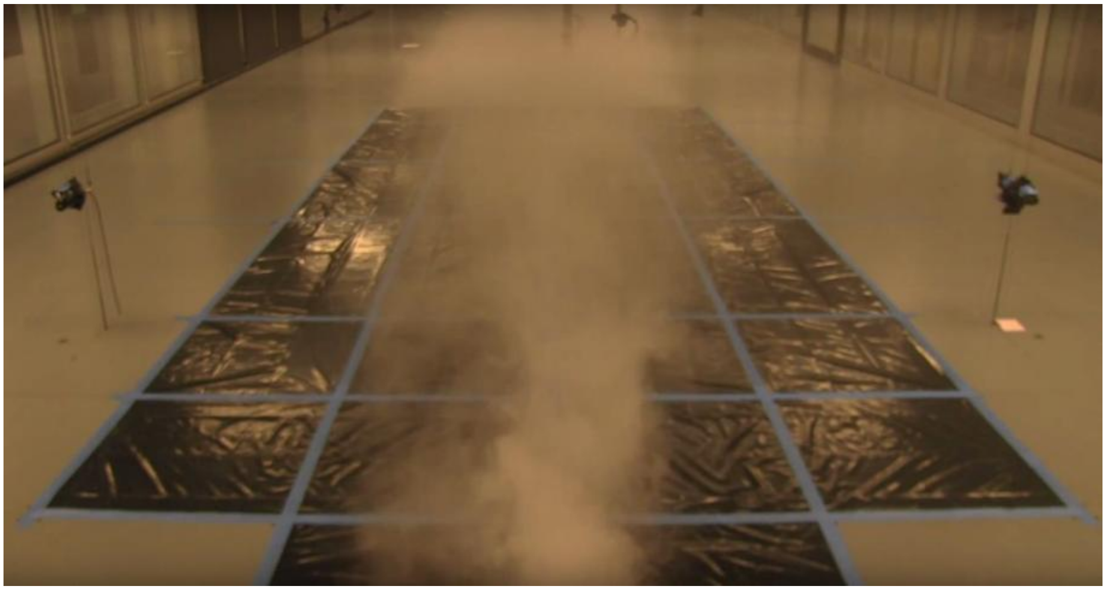

Figure 32. Uniform flow in the tunnel with fog and black plastic on the floor for visualization

Figure 32 shows that the flow injected at the center of the wind tunnel is relatively uniform from a visual perspective throughout the wind tunnel. Subsequently, all other tests conducted in the wind tunnel were done using this configuration. To further validate the uniform distribution of the flow, velocity profiles were measured which will be discussed in a later section.

3.2.1.4 Wind Speed and RPM relationship

The relationship between fan speed in rotations per minute (RPM) and average velocity at the height of 40 cm was determined through prior experimental work shown below in Figure 33.

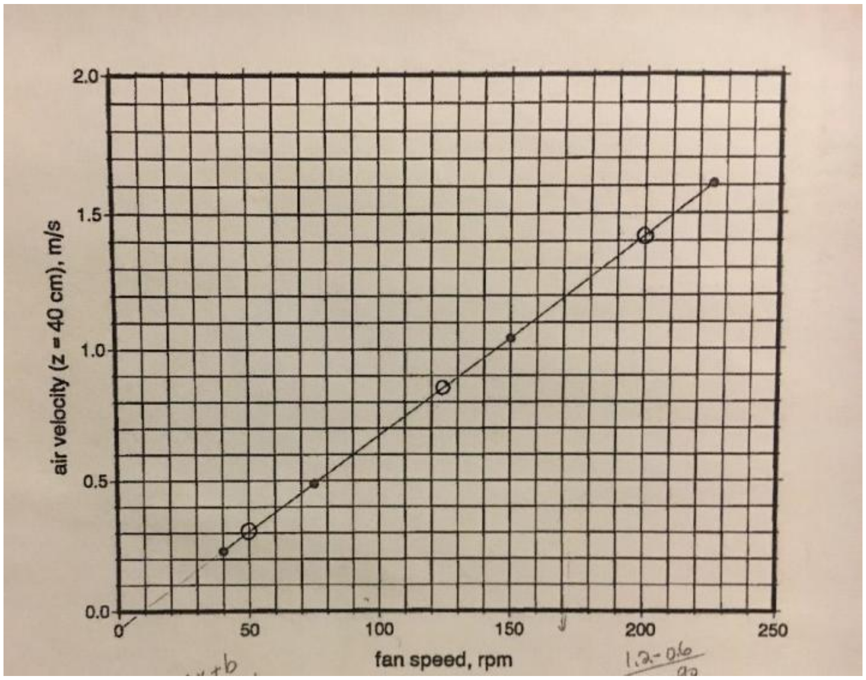

Figure 33. The relationship between velocity in the wind tunnel at the height of 40cm and fan speed in rotations per minute (rpm).

From Figure 33, the relationship between the fan rotations and wind speed in the tunnel is shown to be relatively linear. This relationship was used as a general guideline to set the fan speeds for consistent velocity. These experiments were conducted using fan speeds of 90 and 50 RPM for free stream velocities of 0.71 m/s and 0.35 m/s, respectively at the height of 60 cm.

3.2.1.5 Traverse System

An existing traverse system installed on the ceiling of the wind tunnel was used to remotely place instruments at appropriate positions including Hot Wire Anemometer (HWA), Laser Doppler Velocimeter (LDV), and Flame Ionization Detector (FID) within the wind tunnel. In the present experiments, the atomizer, HWA, LDV, and FID were respectively mounted on arms 1, 2, 3, and 4. Each arm houses a micro-electric motor to move the machine mounted at the end of each arm in the x-, y-, and z-direction. All positions of the arms were controlled remotely from the control room with numerical values indicated on display within the control room.

3.2.2 Area Source

Ground level releases were chosen for these tests for direct application in modeling. For the experiments within this project, an area source was developed for finite-duration releases to improve understanding of the effects of along-wind dispersion. The design and implementation of the area source are discussed below.

3.2.2.1 Design of Preliminary Area Source

A 0.31 m x 0.31 m x 0.31 m (L x W x H) area source was created for the finite-duration experiments. In the preliminary prototype, three sides and the bottom were made out of wood one side was made of a polycarbonate sheet for visualization. The top of the box was comprised of cold-rolled steel with 23% perforated holes. The box had 3 mixing layers of 23% perforated sheets at heights of 7.6 cm, 15.2 cm, and 22.9 cm from the bottom of the box to ensure adequate mixing of the incoming gas from the bottom. For visibility during preliminary testing, 4 strips of white LED 12V lights (MPJA light strip model 31364 OP) were attached to 0.3 cm metal rods that were suspended through holes drilled in the sides of each box. These light/rod combinations were placed across the back of the box at a distance of 5 cm from the back edge. The heights of the lights were at 3.8 cm, 11.4 cm, 19 cm and 26.7 cm for ample lighting between the mixing layers. The tape was used to seal the holes suspending the light / rod combinations to provide a well-sealed box.

3.2.2.2 Visual Testing of Mixing of Area Source

Visualization tests were performed with Rosco water-based fog fluid fed through a Rosco 1500 fog machine at the lowest setting of 1, into 2.4 m length of dryer duct with a 7.6 cm diameter. The dryer duct was fed into the 7.6 cm diameter entrance hole at the bottom of the box. Various combinations of the plates were tested to determine equal spreading of the fog across the 0.31 m x 0.31 m area source. The tests were performed with various arrangements of the mixing plates and an arrangement with a 15.2 cm x 15.2 cm centered blockage on the 7.6 cm plate. In tests, it was apparent that the box filling time was significant to the uniform flow at the outlet of the box. Figure 34 shows a uniform layer of fog leaving the top of the source box with well-mixed fluid inside the box. This configuration was used in the final source box fabricated from aluminum.

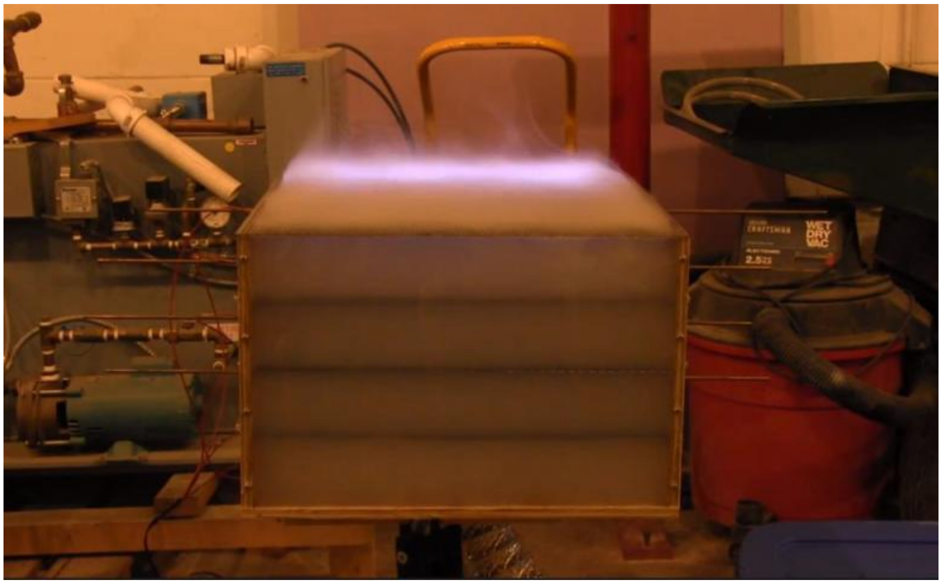

Figure 34. Screenshot of video to show well-distributed flow through preliminary area source

3.2.2.3 Concentration Testing of Mixing of Area Source

After flow visualization was performed on the area source, a 500 ppm propylene and tank air mixture was fed into the bottom of the box for concentration measurements. Concentration measurements were done with a miniPID (Aurora Scientific model 200b) that had no modifications performed. After calibration was performed on the machine, concentration measurements were made at 7.6 cm increments throughout the entire box. Uniform concentration was measured at each test point. After the aluminum box was created, visual releases were performed, and concentration was measured with the fastFID. All results showed a uniform distribution of concentration across the area source.

3.2.2.4 Creation of Permanent Area Source

After preliminary testing of the wooden box was complete, an aluminum version of the box was made with the same mixing design as the preliminary wooden box. The top of the box was modified from the preliminary area source to allow for a controlled release of the source gas. This modified top was comprised of 2 sheets of cold rolled steel with 23% perforated holes and a sheet of polypropylene with 23% perforated holes between the two metal sheets. This design allows for the polypropylene middle sheet to be moved pneumatically between the two metal sheets to open and close the holes when aligned and misaligned, respectively, to allow for finite-duration releases of the source gas through the top of the area source. The box was secured into the wind tunnel at a distance of 20 ft downwind, and 10 ft crosswind (or centerline), with the top of the area source, mounted flush with the floor. When the top of the box is closed, slots in two the sides of the box are opened for the source gas to be vented under the floor of the wind tunnel allowing for a continuous release of the source. This configuration allows the mass flow meters providing the source gas for operating at a constant rate which eliminated issues that can be encountered if the mass flow meters are stopped and started.

3.2.2.5 Automation of Permanent Area Source

The area source was automated with a 120V 5-valve solenoid valve, Arduino Uno, and relay board. House air was fed at 60psi into 3/8” tubing under the wind tunnel to pneumatically control the area source through the solenoid valve. The 60psi house air was connected to the input of the solenoid valve to 1) open the top of the area source while shutting the ventilation sides or 2) close the top of the area source while opening the ventilation sides. The solenoid valve was operated from the control room through the relay board, Arduino, and computer recording data. The Arduino software also allowed for the release duration to be accurately controlled for any release duration desired. Virtual clicker software synchronized the capture of data with the release of source gas.

3.2.3 Concentration testing

Concentration can be measured effectively by different methods. Two common machines to measure the concentration of atmospheric releases are Flame Ionization Detectors (FID) and Photo Ionization Detectors (PID). Both machines are non-specific detectors using an energy source to form ions and record the amount of ions detected. A discussion of the two concentration measurement apparatus is presented below.

3.2.3.1 Fast Flame Ionization Detector (FID)

A Cambustion HFR-400 Atmospheric fast Flame Ionization Detector (FID) was the main equipment used for concentration measurements in the wind tunnel at the Chemical Hazards Research Center. The FID system utilizes a hydrogen flame to burn a hydrocarbon traced sample through a capillary tube inside the instrument. Ions are detected with a metal high DC voltage ion collector. The schematic of the fastFID system is shown below in Figure 35.

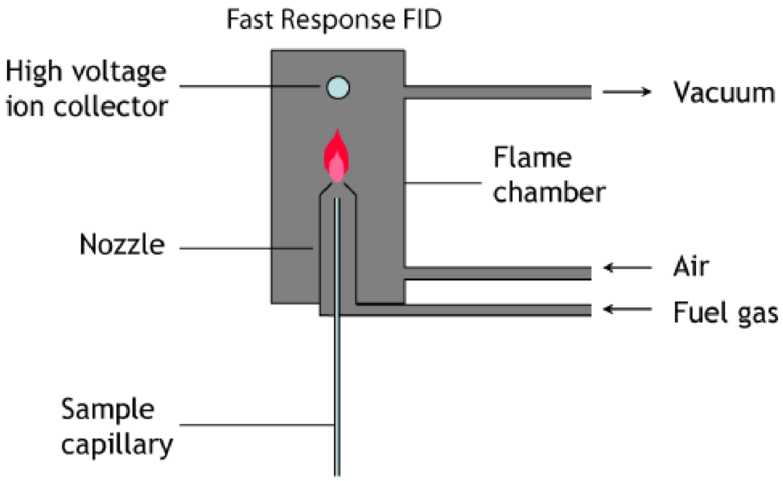

Figure 35. Schematic of fast FID [49]

The current produced by the high voltage ion collector is proportional to the rate of ionization which is dependent on the concentration of hydrocarbons being sampled. The FID is a non-specific aspirated probe that utilizes propane, in these tests, as the source tracer gas for concentration measurements. Known concentrations of propane were used to calibrate the FID. A basic calibration plot is shown below when first testing the fastFID.

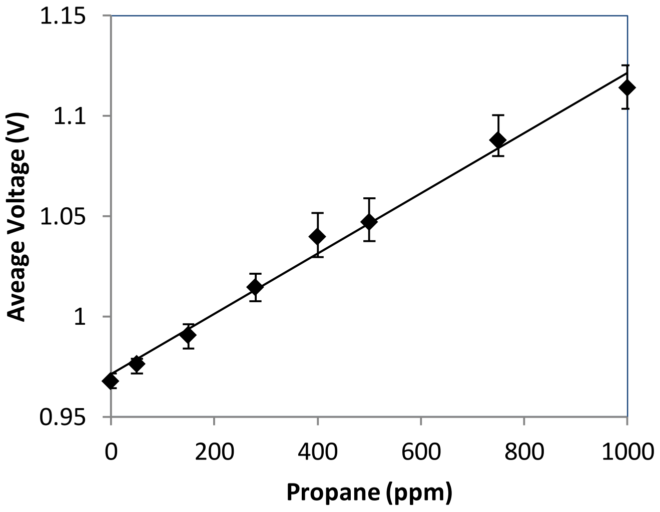

Figure 36. Concentration (ppm) vs. Signal plot for Propane with the fastFID system

Early in the test program, variation in the voltage during calibration was much larger than expected shown in Figure 36. Expanding on the variations, Figure 37 shows the voltage as a function of time where the level of variability is unacceptable for a transient experiment.

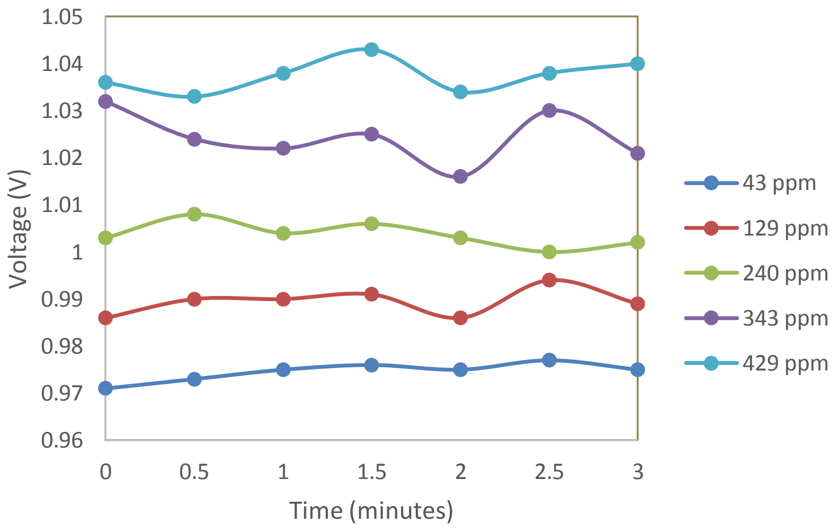

Figure 37. Time vs. signal plot for multiple concentrations of propane using the FID system

After an extensive investigation, the unstable signals shown above were found to be due to inadequate mixing of the propane and air from the mass flow meters. A Koflo Stratos static mixer was installed in the gas lines used during calibration and experiments. In addition to the mixer, the mass flow meters were mounted to a single metal block to reduce the delay when changing concentrations levels during calibration. These additions improved the delivery of gasses producing an acceptable calibration curve shown below.

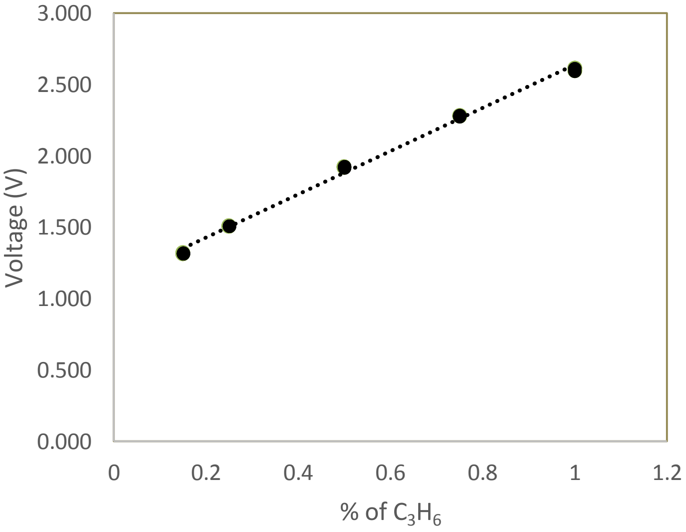

Figure 38. Calibration curve of propane with fast FID

With these changes, the fastFID signal during calibration was stable and linear as shown in Figure 38. The standard deviation of each signal varied from 1.2 mV at 0.15% C_3H_6 to 7 mV at 1% C_3H_6.

3.2.3.2 Mini PhotoIonization Detector (miniPID)

Before the unstable signal associated with the FID was determined to be a mixing problem, an Aurora Scientific miniPID model 200b was purchased. The miniPID is similar to the FID in that it is an aspirated probe using a nonspecific ion detector. The main difference between the PID and FID is that a PID uses a lamp for the energy source where the FID uses a hydrogen flame. The PID is able to ionize compounds with ionization energy less than the lamp power. The pathway of gas sampling through the PID is similar to the FID and is shown below in Figure 39.

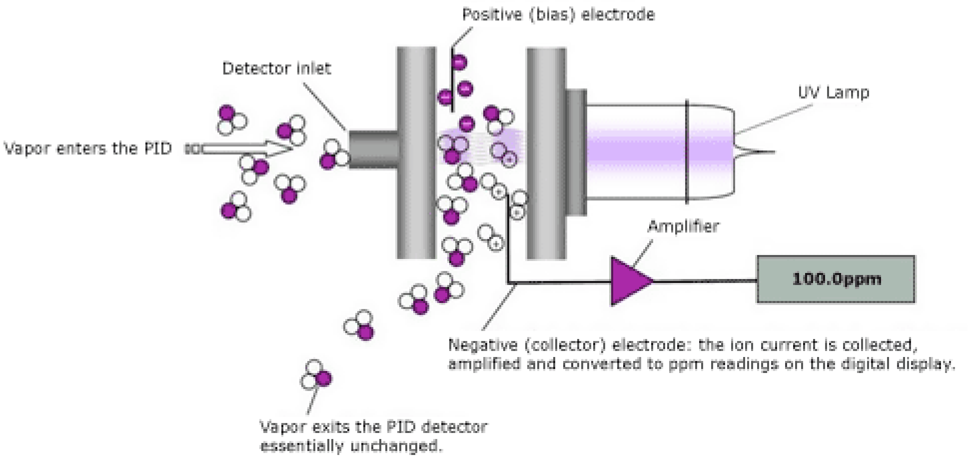

Figure 39. Schematic of PID[50]

From Figure 39, the flow of a sampled gas enters the probe where it passes between two plates. The ions generated by the lam are measured and produce a voltage proportional to the ions produced. The miniPID was modified so that the intake volumetric flowrate matches the area of the probe inlet. This was performed with various chokes on the vacuum line behind the head of the miniPID. Appropriate flow rates were obtained so that the sample velocity was roughly equal to the expected wind speed at the measurement height. Unfortunately, this resulted in time delay issues with the measurements.

3.2.3.3 Comparison of Signals from FID and PID

The decreased flow rates caused a time delay within the miniPID. A period of >3 minutes was required for the miniPID before stable signals could be achieved. For non-choked flow, a period of 1 minute was needed before the miniPID produced stable readings. Both 1 minute and 3 minute periods between introduction of sample and a stable reading were unrealistic to be used for the finite-duration tests. Figure 40 compares the response of the miniPID and fastFID.

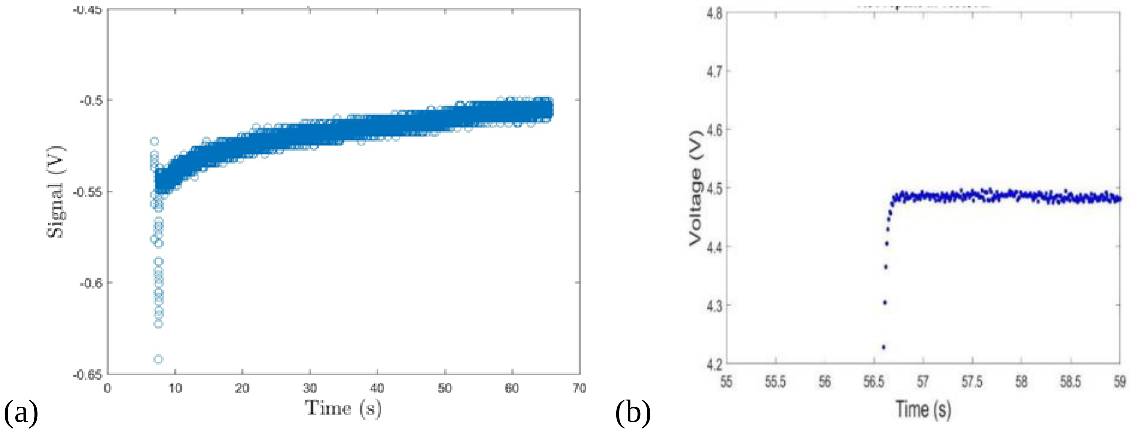

Figure 40. Concentration as a function of time for the miniPID (a) and the fast FID (b)

The signal to noise ratio with the miniPID during this stabilization period is about 10-20% of the signal where the FID has a random signal to noise ratio of <1%. Based on this comparison, the fastFID was used in the experiments.

3.2.4 Mixing of Gases

The accuracy of the concentration depends on the accuracy of the equipment and release of gases into the wind tunnel. As mentioned in the fastFID section, accurate delivery of gasses was improved based on modifications made.

3.2.4.1 Calibration of Mass Flow Controllers (MFC)

A 5 LPM MKS G-series Mass Flow Controller was used for propane in addition to a 20 LPM MKS 1559A Mass Flow Controller for house air. The 5 LPM and 20 LPM MFCs were calibrated using a purpose-built apparatus shown in Figure 41.

Figure 41. Calibration apparatus for 5 lpm and 20 lpm MFC using positive displacement

A 5.313 L Plexiglas box initially filled with water. The time to fill the inner box is recorded to determine the flow rates of the 5 LPM and 20 LPM mass flow controllers using displacement with air. The inner box is manually lifted on a pulley system as gas fills the inside to keep the water level inside and outside of the box equivalent. The corrected flow rates for the MFCs are shown below in Table 26 where y is the output on the MFC with the correction applied, and x is the input value on the MFC to achieve the desired output.

Table 26. Corrected flow rate equations for mass flow controllers

MFC	Corrected flow rate equations for MFCs
5 LPM	$y = 1.0377x$
20 LPM	$y = 1.0088x + 0.0108$

In addition to the corrected flow rate equations shown in Table 26, the input values were adjusted for daily temperature T and pressure P using the ideal gas law. The MFCs were controlled by an MKS Model 647B Multi-Gas Controller. All flow rates of gases were adjusted for the corrected flow rate through calibration and the daily temperature and pressure in the room for increased accuracy.

3.2.4.2 Connection of Gases

The connection from mass flow controllers to the mixing apparatus was observed to have a time delay associated with the 5 SCCM MFC that was used with the miniPID. With low flow rates such as 5 SCCM, this length can add an hour to the time the gases are turned on until a well-mixed flow is achieved. A solid aluminum block with standard pipe fitting tapped holes was used as the connection site for up to 5 mass flow controllers to decrease the time delay associated with lower flow rates as shown in Figure 42.

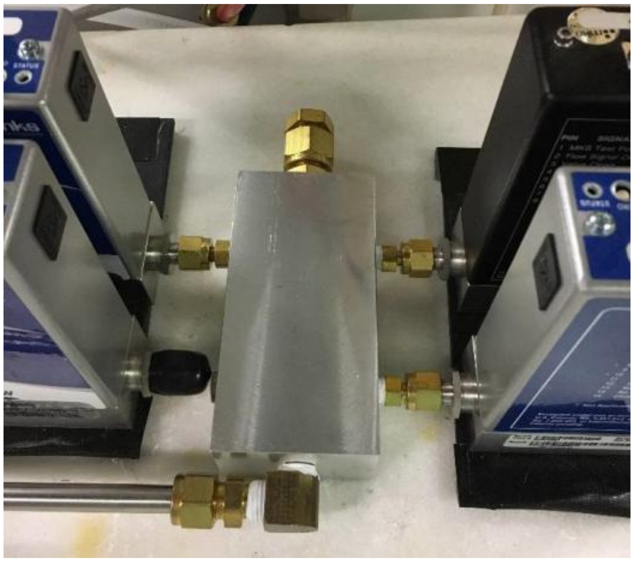

Figure 42. The connection of mass flow meters used in tests

The dimensions of the aluminum box are 11.4 cm x 5.7 cm by 5cm with four 1/8” threaded holes on the longer edges of the box to accommodate the standard MFCs, a 3/8” threaded hole at the end for larger MFCs, and a 1/4” threaded hole at the head of the box for outlet flow to be fed into a static mixer. When an MFC was not connected, plugs were used to seal the threaded holes. The aluminum box drastically decreased the dead time between the output of the MFC and the mixing apparatus from 1 hour to almost instantaneous flow to the mixing apparatus.

3.2.4.3 Mixing of Gases

From the aluminum box, the gases flow straight into a Koflo Stratos static mixer with 32 helical mixing elements within the 3/8” OD metal tube. The design of the Koflo Stratos static mixer is shown below in Figure 43.

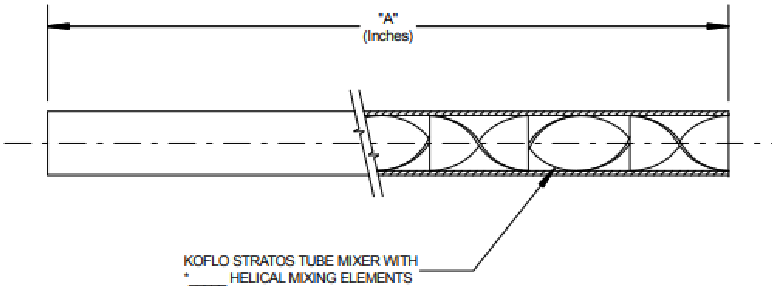

Figure 43. Koflo Stratos static mixer[51] used in the gas setup

The new apparatus ensures adequate mixing by the 32 helical mixing elements.

3.2.4.4 Additional Mixing of Gases with Dead Space

At low concentrations, a sinusoidal signal was observed on an oscilloscope. Gases were proven to be well mixed at higher concentration. The mass flow controllers were observed to be fluctuating in their output causing the sinusoidal signal. Dead space was created with a 2 L volume with metal baffles to result in a more uniform signal from volume averaging. The original dead space developed for the mixing setup is shown below in Figure 44.

Figure 44. Dead space, static mixer, and aluminum box for accurate delivery of gases

From Figure 44, the original 2 L dead space can be seen on the top left side of the figure. The dead space with mixing baffles mitigated the effects of a sinusoidal signal resulting in well mixed, accurate delivery of source gases. A 10 L dead space was developed with the same method when delivering larger volumes of gas to the area source. Both dead spaces remove the fluctuations of the MFCs in maintaining an accurate and steady concentration of output gases.

3.2.4.5 Results of the new mixing of gases

When gas is fed from the cylinders to the mass flow controllers, through the aluminum box, static mixer, and dead space, accurate and well-mixed gases are produced. Concentration measurements of propane were retested with the FID to check the stability of the signal and are shown below in Table 27.

Table 27. Concentration testing of FID with propane after modifying the mixing setup

Propane %	average (V)	max (V)	min (V)	Range %	Stand. Dev (V)
1	2.555	2.583	2.529	2.0%	0.006
0.75	2.227	2.249	2.205	2.0%	0.005
0.5	1.871	1.890	1.856	1.8%	0.004
0.25	1.474	1.484	1.462	1.5%	0.003
0.15	1.295	1.306	1.282	1.9%	0.003
0	0.983	0.986	0.979	0.7%	0.001

The average voltage, maximum voltage, and minimum voltage measured for a known concentration of propane are shown above in Table 27. In addition to the voltages, the ranges of the variation in signals and their standard deviations were also recorded and show the consistent and accurate delivery of gases.

3.2.5 Laser Doppler Velocimetry (LDV)

A Laser Doppler Velocimetry (LDV) system is a non-intrusive velocity measurement system projecting monochromatic, coherent lasers into fluid flow seeded with particles. The reflection of laser light by the particles causes a Doppler shift in frequency that is proportional to the velocity of the moving, illuminated particles. The Doppler shift is the difference between frequencies. The velocity is then determined by analyzing the frequency of the signals.

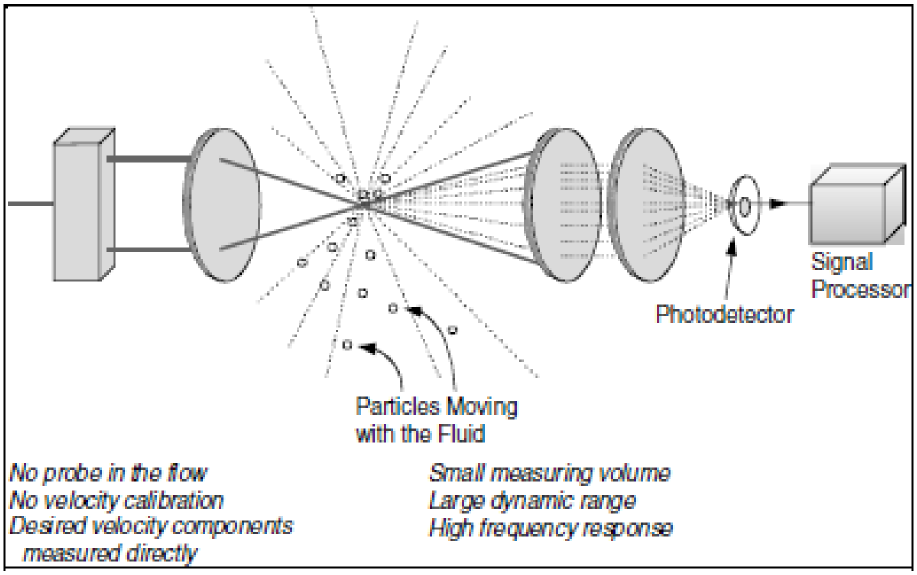

Figure 45. Example of the LDV system

The LDV system at the CHRC is comprised of (1) Coherent Innova 70C Argon laser (2) TSI Colorburst transmitting optic system (3) TSI TRx10 fiber optic transmitting and receiving probes (4) TSI IFA FSA 4000 signal processing system with the TSI Flowsizer 64 Software. A continuous Argon laser was supplied and split into multiple wavelengths (514.5 nm - green, 488.0 nm - blue, and 476.5 nm - violet) using the TSI Colorburst transmitting optic system. The wavelengths were carried through fiber optic cables to the probes. The probes were aligned so that all 6 beams intersected at a focal point. The flow was seeded with an atomizer or fog machine as background seeding to provide neutrally buoyant particles which pass through the focal point for the measurement of velocity.

3.2.5.1 Seeding of the LDV

Adequate seeding is vital for the optimal performance of the LDV. Seeding particles need to be small enough to be picked up by the fluid flow and travel at the same velocity as the fluid. Seed particles need to be neutrally buoyant to accurately track the flow without buoyancy effects adding to the velocity in the vertical direction. If denser-than-air effects are seen, the LDV will pick up the downward motion of the particle as the downward velocity. The seed particles need to be injected non-invasively into the flow rate to avoid disruption of flow upwind. If a large object is directly upwind of the flow, bluff body effects will be measured by the LDV instead of true velocity in the wind tunnel. Lastly, seeding material needs to be non-toxic due to exposure in the facility. Two pieces of equipment used for seeding will be discussed further: atomizer and fog machine.

3.2.5.1.1 Atomizer

A TSI Model 8320 Atomizer was used primarily for seeding of the LDV system. The atomizer had a house supply of air fed to the atomizer at 80psi. The initial design of the atomizer had a straight outlet tube which provided seeding directly above the atomizer. This was not a desirable configuration for seeding down to the floor of the wind tunnel. Consequently, a new outlet tube was created using curved flexible tubing secured to a ¼ cross-section of a 3” PVC pipe 2.5 cm in thickness. A larger diameter tube was then attached to the flexible tubing projected parallel to the floor from the atomizer body. This modification allowed for the spread of seeding to reach the floor for velocity measurements at low heights and can be seen in Figure 46.

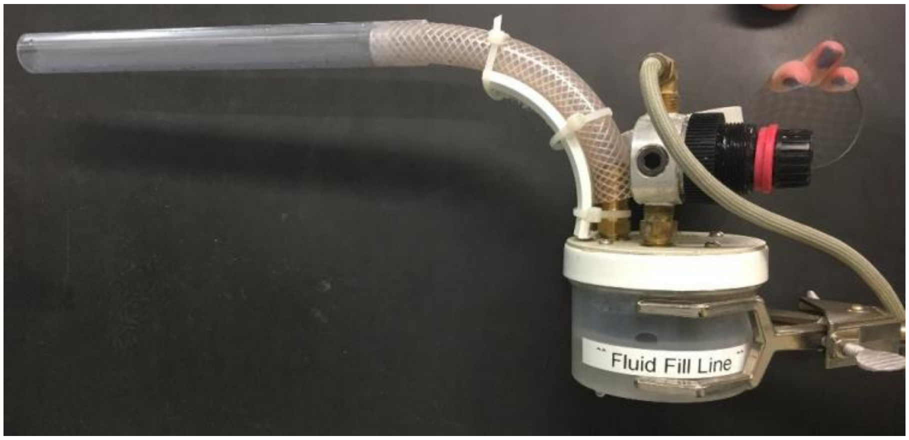

Figure 46. TSI Model 8320 Atomizer with outlet tube modifications for optimal seeding

The modified atomizer was placed 0.24 m upwind, 45 cm crosswind, and at the same height of the LDV to provide adequate seeding and not cause bluff body effects. This distance provided ample seeding for the LDV for preliminary tests. The atomizer was filled with a 50% glycerin and 50% deionized water by volume ratio. This solution had been pre-mixed for 1 hour in an ultrasonic agitator before use in the atomizer to ensure a uniform solution. For wind speeds of <1 m/s, the seeding was observed to be "slumping" towards the ground before it reached the LDV 0.24 m downwind. This phenomenon was presumed to be the result of the presence of large droplets expressed in the non-dimensional Weber number[52], *We*

$$\boldsymbol{We = \frac{\rho v^2 l}{\sigma}} \tag{54}$$

Where ρ is the density (kg/m^3), v is the velocity (m/s), l is the characteristic length (or droplet diameter) (m), and σ is the surface tension (N/m). With the glycerin being dense, this parameter was unable to be changed. To decrease the surface tension, a surfactant was added to the seeding solution. 1-Butanol was chosen due to its long hydrocarbon chain and evaporation properties. Molarities of 0.1-1M were tested in the glycerin-water solution. The molarity of 1M showed no denser-than-air effects on the plume and was used for all LDV testing using the atomizer.

3.2.5.1.2 Fog Machine

Previous LDV tests performed in 2001 at the CHRC used a Rosco 1500 fog machine filled with Rosco fog fluid (propylene glycol and deionized water) resulted in seeding rates of 1000Hz with the LDV in coincidence mode for 2D measurements[53]. In a bid to replicate such high seeding rates, 3 fog machines were tested: Rosco 1500, Rosco PF-1200, and a Virhuck 400W machine. Modifications to the machines were undertaken to allow for continuous delivery of fog and control of the releases from the control room. In addition to the flow, different solutions were tested: Rosco Fog Fluid, Froggy's Fog Cryo Freeze, Froggy's Fog Fast Dissipating, Chauvet DJ FJ-U, and multiple homemade solutions of glycerin in DI water (50%, 25%, and 12.5%). While glycerin in DI water produced the thickest smoke, a slippery residue is left. Propylene glycol was found in the SDS's of all manufactured solutions. Different compositions of propylene glycol and DI water was tested until it was found that high concentration of this solution caused difficulty breathing and destroyed contact lens. These results are consistent with exposure of non-asthmatics to propylene glycol mist resulting in decreased tears, increased ocular and throat symptoms, decreased forced vital capacity, and cough[54].

Different configurations for the delivery of the fog fluid was tested. Three configurations that were analyzed: 1) direct delivery of fog from the machine, 2) delivery of fog from the machine through 0.24 m of 7.6 cm aluminum dryer duct, and 3) delivery of fog from the machine through 0.24 m of 7.6 cm aluminum dryer duct submerged in an ice bath. The different configurations for delivery have an effect on the temperature fog which results in a change in the density of the fog. A comparison of the 3 delivery mechanisms of 50% glycerin and 50% DI water solution are shown below in Figure 47.

Figure 47 Delivery of 50% glycerin solution with no dryer duct (left), with dryer duct (middle), and with dryer duct submerged in ice (right)

The delivery mechanisms have a large effect of the fog seeding and density as shown above in Figure 47. Delivery of fog without a fog chiller or dryer duct was shown to provide the most diluted but most dispersed cloud. Delivery of fog through a fog chiller with and without ice provided a more dense cloud. While delivery of fog through a fog chiller provided denser seeding, they had denser than air effects which are not desired with the LDV. A delivery of 50/50 glycerin/water solution was chosen due to its neutral buoyancy and non-toxic properties. This fog was flooded in the entire wind tunnel to remove entrainment effects when directly injected upwind of the wind tunnel. While this method provided great seeding, a thorough cleaning of the wind tunnel needed to be performed after all velocity profiles were measured. The seeding of the entirety of the wind tunnel flow was required when measuring increased turbulence observed with multiple rows of spires.

3.2.5.2 Mounting and Alignment of the probes

All six beams produced from the Colorburst system of 3 frequencies (blue, green, and violet) needed to be aligned for 3D measurements through a 100-micrometer hole. To measure the velocities within 0.5cm to the floor, the probes were mounted at angles of ~54^0 (blue and green probe) and ~12^0 (violet probe) so that the focal point of all of the lasers could reach the floor. LDV measurements are typically made with each probe normally mounted at a 90˚ angle with respect to the flow. The TRx10 fiber optic probe projected blue and green beams, so any alignment issues had to be repaired by the manufacturer. The violet probe, however, was separately mounted and needed to be aligned with the focal point of the blue and green probe. The configuration of the probes is shown below.

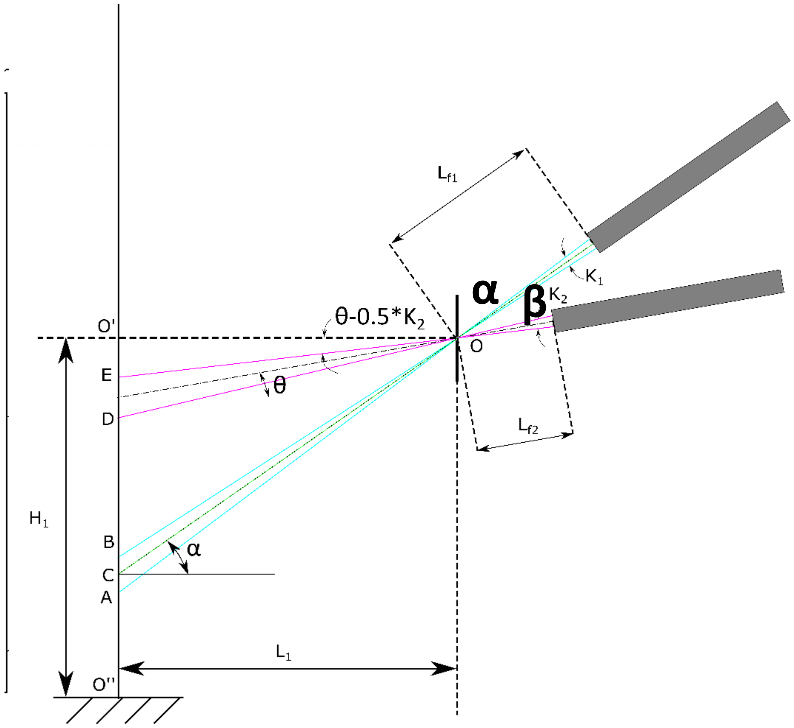

Figure 48. Alignment of probes with their respective angles of α for the green and blue probe and β for the violet probe

The alignment procedure was performed with a 100-micrometer diameter aperture. The power of each beam was measured at the output of the 100-micrometer hole to ensure that full beams were projected during alignment.

3.2.5.3 3D flow

LDV systems are able to measure flow in single or multiple directions depending on the angle of the probe. In particular, if three frequencies are produced with three pairs of beams, as in the testing arrangement, the LDV is capable of measuring velocity in three directions. Coincidence mode in the software was enabled for the tests. This allowed for 3D velocities of the particle to be measured simultaneously, allowing for properties such as Reynolds stress or friction velocity to be obtained from the measurement of flow. If a particle was not measured by all of the beams, it was not recorded resulting in more accurate velocity measurements.

3.2.5.4 Matrix Transformation

To account for corrections in the direction from 90˚ to the angles mounted in the probe arrangements, a transformation matrix was applied in the software. The projection of the matrix with respect to the angles of the probes provides the adjusted velocity measurements in the x-, y-, and z-direction. The transformation for the 3D LDV system at the CHRC is shown with theoretical and numerical values in Figure 49.

	x	y	z
1	$\cos\gamma$	$-\sin\alpha \cdot \sin\gamma$	$\cos\alpha \cdot \sin\gamma$
2	0	$-\cos\alpha$	$-\sin\alpha$
3	0	$-\cos\beta$	$\sin\beta$

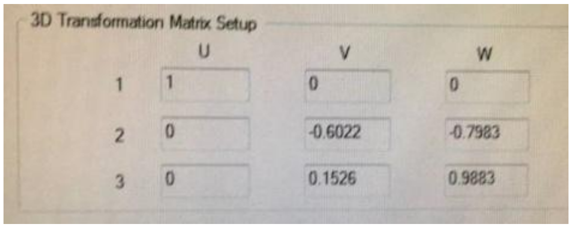

3D Transformation Matrix Setup

	U	V	W
1	1	0	0
2	0	-0.6022	-0.7983
3	0	0.1526	0.9883

Figure 49. Theoretical[55] (left) and numerical (right) values for the matrix transformation for the LDV mounted at angles

From the numerical values shown in Figure 49, the full velocity in Channel 1 (green beams) is contributing to U (velocity in the x-direction). The measured velocities from Channel 2 (blue beams) and Channel 3 (violet beams) are split between V and W (velocities in the y- and z-direction respectively) due to their angles. The software measures the velocities of each channel and then transforms the velocities to account for the angles in which they are mounted with the transformation matrix to produce accurate transformed 3D velocity measurements.

Testing of this transformation matrix was performed comparing all velocities and turbulence intensities reported with the transformation matrix applied in the software to values measured solely by one pair of frequencies at a 90˚ angle with no correction. During this comparison, the violet probe was shown to be unusable. A new transformation matrix was applied with the blue beam measuring both the y- and z-direction with the sin(α) and cos(α) respectfully. After this transformation matrix was applied, the values at an angle still did not match the values measured at 90˚. An error in the manual was found. Performing the inverse of the transformation matrix to the data measured at an angle was shown to provide the same values as measured at 90˚. The TSI Flowsizer was unable to process this. The inverse of the transformation matrix for 2 beams resulting in 3D velocity measurements required Matlab for data processing.

3.2.5.5 Flowsizer 64 Software Settings

The Flowsizer 64 software measures and analyzes the frequencies transmitted from the probes and their backscatter through a signal processor to determine the correct velocities for each channel. The software is a function of its inputs, so accurate input conditions are vital to accurate outputs. The input conditions for the tests performed are described below in the hardware and software settings.

3.2.5.5.1 Hardware Settings

The hardware settings specify the correct parameters associated with the laser and the fiber optic probes, such as frequencies, distances, sizes, etc. In the hardware settings, the channels enabled can be selected for 1, 2, or 3D measurements. The transformation matrix, described above, is implemented in the hardware settings to correct for the angles of the probes. Information about the specific probes used is input into the hardware settings such as wavelength, focal length, beam separator, laser beam diameter, beam expander, fringe spacing, Bragg cell, and diameter sizes. In this configuration, TSI TRx10 fiber optic probes were used. Optic settings for the system are shown below.

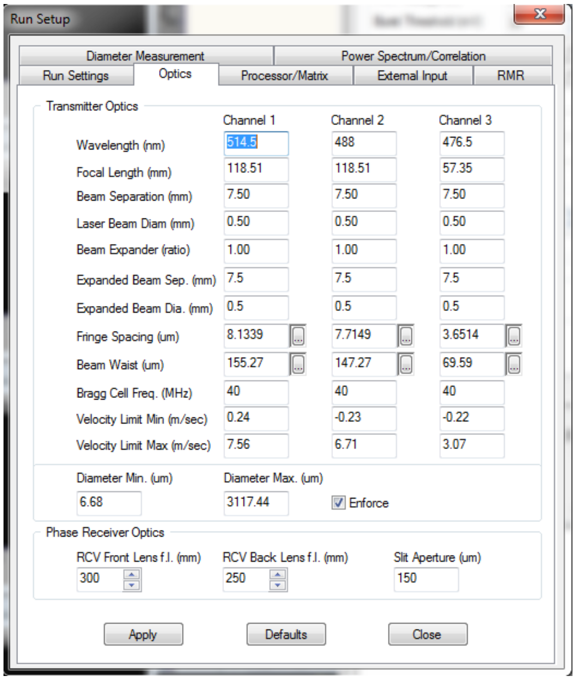

Transmitter Optics

	Channel 1	Channel 2	Channel 3
Wavelength (nm)	514.5	488	476.5
Focal Length (mm)	118.51	118.51	57.35
Beam Separation (mm)	7.50	7.50	7.50
Laser Beam Diam (mm)	0.50	0.50	0.50
Beam Expander (ratio)	1.00	1.00	1.00
Expanded Beam Sep. (mm)	7.5	7.5	7.5
Expanded Beam Dia. (mm)	0.5	0.5	0.5
Fringe Spacing (um)	8.1339	7.7149	3.6514
Beam Waist (um)	155.27	147.27	69.59
Bragg Cell Freq. (MHz)	40	40	40
Velocity Limit Min (m/sec)	0.24	-0.23	-0.22
Velocity Limit Max (m/sec)	7.56	6.71	3.07

Diameter Min. (um) 6.68

Diameter Max. (um) 3117.44

☑ Enforce

Phase Receiver Optics

RCV Front Lens f.l. (mm) 300

RCV Back Lens f.l. (mm) 250

Slit Aperture (um) 150

Figure 50. Optimal Hardware settings for Optics in Flowsizer 64 software

From Figure 50, the specified values for each of the settings are shown. These values were obtained from the TRx10 fiberoptic probe manual, Coherent Innova 70C Laser manual, and physically measured for the setup within the wind tunnel. The settings input into the hardware are all a function of the equipment used and how it is physically aligned.

3.2.5.5.2 Software Settings

The software settings in the Flowsizer 64 Software consist of the PMT voltage, Burst Threshold, Band Pass Filter, Signal to Noise Ratio, Downmixing Frequency, Gate Scale, and Subranges. The software settings are less concrete in comparison to the hardware settings in which they are dependent on the overall system and not individual measured values. To determine the optimal values for each setting, trial and error are required. The optimal settings for the LDV configuration in the wind tunnel at the CHRC at 90RPM are shown below in Figure 51.

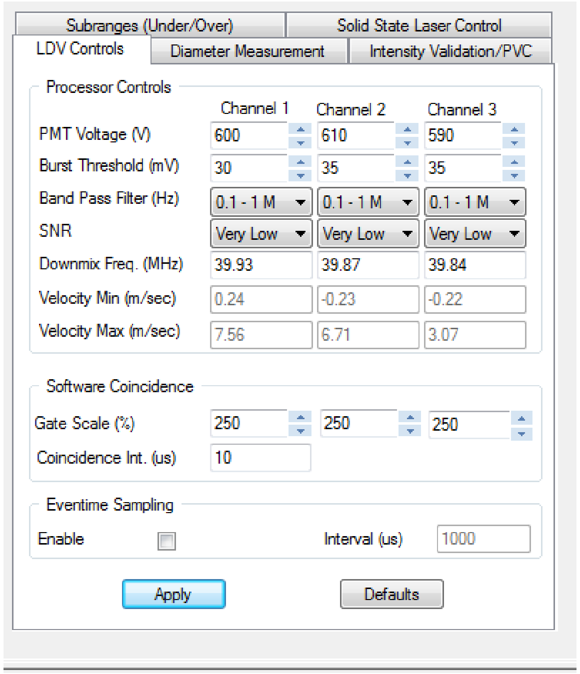

Processor Controls

	Channel 1	Channel 2	Channel 3
PMT Voltage (V)	600	610	590
Burst Threshold (mV)	30	35	35
Band Pass Filter (Hz)	0.1 - 1 M	0.1 - 1 M	0.1 - 1 M
SNR	Very Low	Very Low	Very Low
Downmix Freq. (MHz)	39.93	39.87	39.84
Velocity Min (m/sec)	0.24	-0.23	-0.22
Velocity Max (m/sec)	7.56	6.71	3.07

Software Coincidence

Gate Scale (%)	250	250	250
Coincidence Int. (us)	10		

Eventime Sampling

Enable ☐ Interval (us) 1000

Figure 51. Optimal Software settings for LDV controls in Flowsizer 64 software

Optimal settings were determined by comparing, the data rate, burst efficiencies, and Gaussian distributions to ensure that they compare to the values recommended by the manufacturers for quality and reliable measurements. Gaussian distributions of the velocity or frequency versus valid count for all channels are desired. An example of the Gaussian distributions achieved is shown below in Figure 52.

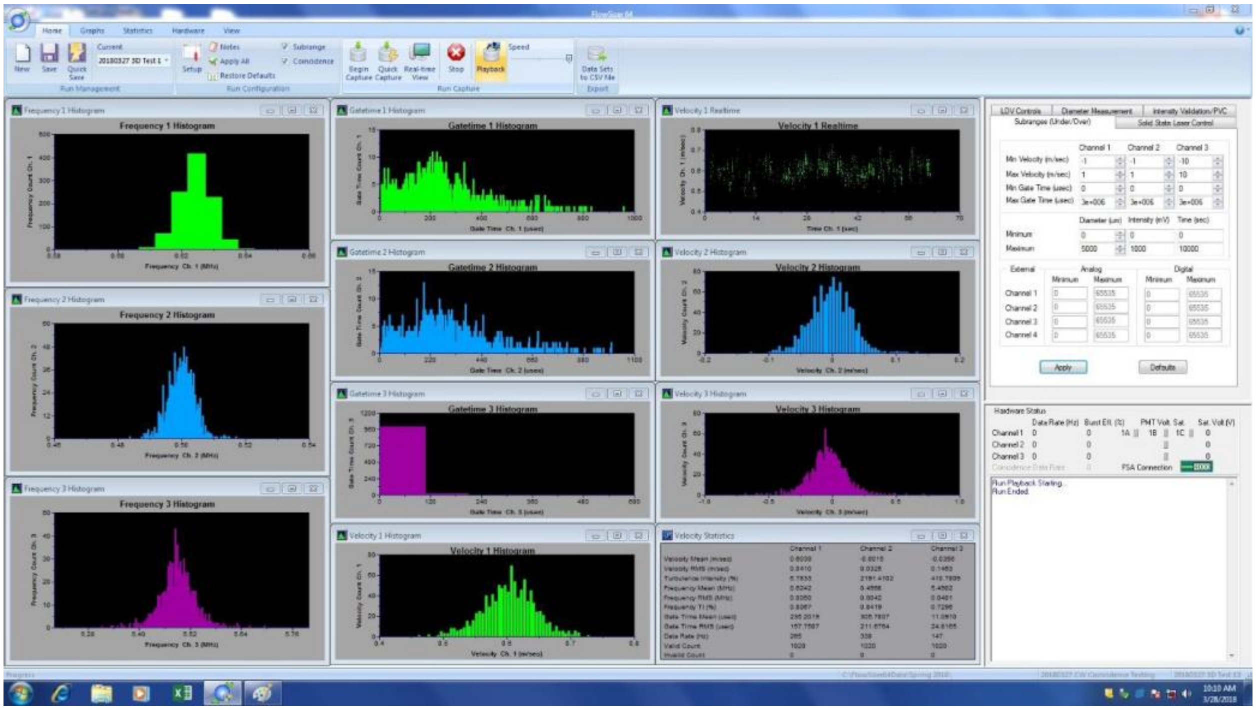

LDV Controls | Diameter Measurement | Intensity Validation/PVC | Subranges (Under/Over) | Solid State Laser Control

	Channel 1	Channel 2	Channel 3
Min Velocity (m/sec)	-1	-1	-10
Max Velocity (m/sec)	1	1	10
Min Gate Time (usec)	0	0	0
Max Gate Time (usec)	3e+006	3e+006	3e+006

	Diameter (um)	Intensity (mV)	Time (sec)
Minimum	0	0	0
Maximum	5000	1000	10000

External	Analog Minimum	Analog Maximum	Digital Minimum	Digital Maximum
Channel 1	0	65535	0	65535
Channel 2	0	65535	0	65535
Channel 3	0	65535	0	65535
Channel 4	0	65535	0	65535

Run Playback Starting.
Run Ended.

	Channel 1	Channel 2	Channel 3
Velocity Mean (m/sec)	0.6038	-0.0015	-0.0356
Velocity RMS (m/sec)	0.0410	0.0328	0.1463
Turbulence Intensity (%)	6.7833	2181.4102	410.7895
Frequency Mean (MHz)	0.6242	0.4556	5.4562
Frequency RMS (MHz)	0.0050	0.0042	0.0401
Frequency TI (%)	0.8067	0.8419	0.7296
Gate Time Mean (usec)	295.2019	305.7937	11.0810
Gate Time RMS (usec)	157.7587	211.6764	24.6165
Data Rate (Hz)	285	338	147
Valid Count	1020	1020	1020
Invalid Count	0	0	0

Figure 52. Results of velocity measurements from optimal software settings

From Figure 52, Gaussian distributions are achieved for the velocities and frequencies for channels 1, 2 and 3. This shows that the settings chosen are of optimal values to produce accurate velocity measurements.

3.2.5.6 Analysis of the Velocity Measurements

Transformed velocities obtained from the processor matrix as a function of time, were exported from the Flowsizer 64 software. These values were analyzed within Matlab for their respective sample size with the following equations[56]. The instantaneous, transformed values for velocities were exported from the Flowsizer 64 software and are referred to below as U_i, V_i, and W_i for the x, y, and z instantaneous velocity directions respectively. The mean velocities in each direction, *U, V,* and *W,* are solved as a function of the instantaneous velocities for the sample size, *N,* in equations (55) - (57).

$$\boldsymbol{U = \frac{1}{N}\sum_{i=1}^{N} U_i} \tag{55}$$

$$\boldsymbol{V = \frac{1}{N}\sum_{i=1}^{N} V_i} \tag{56}$$

$$\boldsymbol{W = \frac{1}{N}\sum_{i=1}^{N} W_i} \tag{57}$$

The turbulent components associated with each velocity, *u, v,* and *w,* are solved as a function of the instantaneous velocities and their deviation from the mean velocities for each test with equations (58) - (60).

$$\boldsymbol{u = \left[\frac{1}{N}\sum_{i=1}^{N}(U_i - U)^2\right]^{\frac{1}{2}}} \tag{58}$$

$$\boldsymbol{v = \left[\frac{1}{N}\sum_{i=1}^{N}(V_i - V)^2\right]^{\frac{1}{2}}} \tag{59}$$

$$\boldsymbol{w = \left[\frac{1}{N}\sum_{i=1}^{N}(W_i - W)^2\right]^{\frac{1}{2}}} \tag{60}$$

The correlation between the turbulent components *u* and *w* is shown with ρ_{uw} below.

$$\boldsymbol{\rho_{uw} = \frac{\overline{(U_\imath - U)(W_\imath - W)}}{uw}} \tag{61}$$

The Reynolds shear stress, $-uw,$ is a function of the turbulent intensity components in the x and z directions.

$$\boldsymbol{-uw = -\overline{(U_\imath - U)(W_\imath - W)}} \tag{62}$$

The friction velocity, u_*, is a function of the Reynolds shear stress.

$$\boldsymbol{u_* = \sqrt{-uw}} \tag{63}$$

Triple correlations for each direction are determined with equations (64) - (68).

$$\boldsymbol{u^3 = \overline{(U_\imath - U)^3}} \tag{64}$$

$$\boldsymbol{v^3 = \overline{(V_\imath - V)^3}} \tag{65}$$

$$\boldsymbol{w^3 = \overline{(W_\imath - W)^3}} \tag{66}$$

$$\boldsymbol{u^2w = \overline{(U_\imath - U)^2(W_\imath - W)}} \tag{67}$$

$$\boldsymbol{uw^2 = \overline{(U_\imath - U)(W_\imath - W)^2}} \tag{68}$$

The Skewness factors, $S_u, S_v,$ and S_w for each direction are determined through equations (69) - (71).

$$\boldsymbol{S_u = \frac{\overline{(U_\imath - U)^3}}{\left[\overline{(U_\imath - U)^2}\right]^{\frac{3}{2}}}} \tag{69}$$

$$\boldsymbol{S_v = \frac{\overline{(V_\imath - V)^3}}{\left[\overline{(V_\imath - V)^2}\right]^{\frac{3}{2}}}} \tag{70}$$

$$\boldsymbol{S_w = \frac{\overline{(W_\imath - W)^3}}{\left[\overline{(W_\imath - W)^2}\right]^{\frac{3}{2}}}} \tag{71}$$

The Flatness factors, $F_u, F_v, and\ F_w$ for each direction are determined through equations (72) - (74).

$$\boldsymbol{F_u = \frac{\overline{(U_\imath - U)^4}}{\left[\overline{(U_\imath - U)^2}\right]^{2}}} \tag{72}$$

$$\boldsymbol{F_v = \frac{\overline{(V_\imath - V)^4}}{\left[\overline{(V_\imath - V)^2}\right]^{2}}} \tag{73}$$

$$\boldsymbol{F_w} = \frac{\overline{(\boldsymbol{W_\iota} - \boldsymbol{W})^4}}{\left[\overline{(\boldsymbol{W_\iota} - \boldsymbol{W})^2}\right]^2} \tag{74}$$

Each of these relationships was analyzed for each test performed with the LDV and is available in electronic lab notebooks for all velocity profiles. It should be noted that these relationships require 3D velocity measurements. Previous experiments were unable to provide the relationships above due to only 2D measurements captured.

3.2.6 Hot Wire Anemometry (HWA)

A hot wire anemometry (HWA) system was used in conjunction with the Laser Doppler Velocimetry (LDV) system for velocity measurements in the wind tunnel. The HWA system was comprised of a TSI IFA-300 Constant Temperature Anemometer (CTA), HWA film sensors (TSI 1248A-10 film), and TSI ThermalPro Software. The HWA system is sensitive to high frequencies, able to recognize small changes in frequencies, and cheaper than the LDV[57]. While the HWA has its advantages, it does not provide 3D velocity profiles. While it is only a 1D system, it is a good check to make sure the LDV system produces comparable results. The HWA system utilizes a thin film placed across two probes shown below in Figure 53.

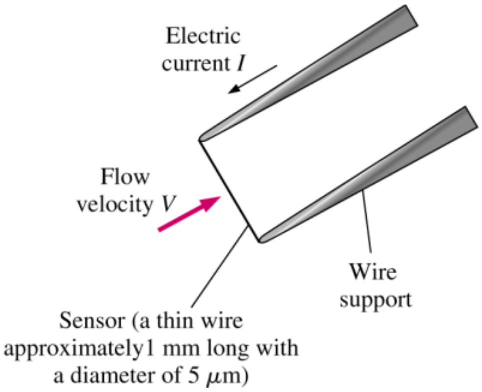

Figure 53. Visual representation of HWA probe with velocity, film (labeled wire), and current[58]

Introducing a velocity across the film, shown in Figure 53, changes the temperature of the probe. When placed in fluid flow, a change in velocity causes a change in temperature which is directly correlated to the change in output voltage. In the present tests, gains and offsets were applied to the output voltage for improved single to noise ratio. Output voltages were fed into a 12-bit analog-to-digital converter and recorded with TSI ThermalPro software at a rate of 500Hz for 2 minutes. Results of the recorded voltages were analyzed with Matlab.

A careful calibration was conducted with a transparent acrylic tube 1.2 cm in diameter and 76 cm in length. Tank air was fed from a mass flow controller into the end of the calibration tube at velocities that would produce Reynolds numbers <2100 (to ensure laminar flow). Approximately 10 velocities were chosen for calibration values using this setup. Voltages were recorded for each of these velocities, and a 4th order polynomial was fit to the calibration curve. Output voltages were analyzed with the calibration curve to determine the appropriate velocities associated with the output voltages. Each probe was calibrated before and after each test to account for the change in temperature and pressure in the room during testing.

3.2.7 Velocity Profiles

To determine uniform flow within the wind tunnel, velocity measurements were conducted from which 3D velocity profiles were extracted and analyzed. A velocity profile measures the velocity at a stationary x- and y-location in the wind tunnel starting at the height of 60 cm and decreasing logarithmically until a height of 1 cm. Velocity profiles made with the HWA were compared to the velocity profiles made with the LDV to ensure wind speeds were accurately portrayed between the two systems. All velocity profiles were performed with fan speeds at 50 and 90 RPM running for greater than 1 hour for fully stabilized flow within the wind tunnel with air conditioners off and all doors shut. Velocity profiles were measured at specific locations in the wind tunnel shown below in Figure 54.

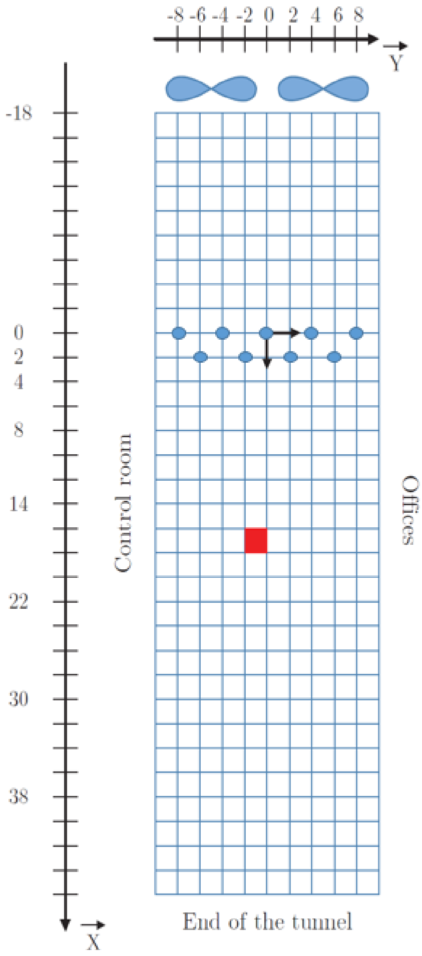

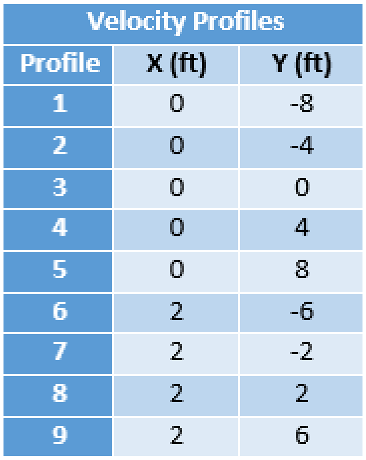

Velocity Profiles		
Profile	**X (ft)**	**Y (ft)**
1	0	-8
2	0	-4
3	0	0
4	0	4
5	0	8
6	2	-6
7	2	-2
8	2	2
9	2	6

Figure 54. The scale of Wind Tunnel (left) with locations of velocity profiles obtained (right)

Velocity profiles measured at locations across the full span of the width of the tunnel to assure that the velocities were indeed uniform throughout the entire wind tunnel. Full results of all of the velocity profiles are located in the appendices.

3.2.7.1 Validation of LDV with HWA

Velocities produced by the LDV needed to be validated with the HWA to ensure the settings selected in the Flowsizer software predicted accurate velocity measurements. To validate the LDV results, two velocity profiles taken with the HWA on different days were compared. Validation velocity profiles were performed at velocity profile 3 (X-0ft and Y-0ft) with fans set at 90 RPM. The results of these validations are shown below in Figure 55.

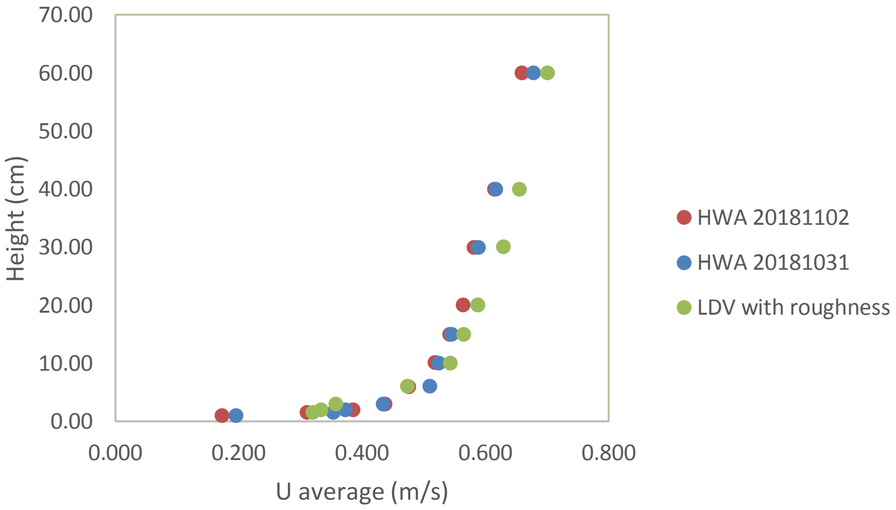

Figure 55. Validation of Velocity Profiles at X=0ft and Y=0ft with 90RPM with LDV measurements and HWA measurements from 2 separate dates

From Figure 55, the velocity profiles obtained at velocity profile 3 show reasonable values with average errors ≤ 6% of each other. The only condition that was changed between the LDV and HWA measurements were the artificial surface roughness installed for the LDV tests. This addition only has an effect on the bottom 10 cm of the velocity profile and therefore should not have an effect on these results. It should also be noted that the HWA is sensitive to temperature. As the room temperature increases, there can be a change in the accuracy of the velocity results where the LDV system is not sensitive to temperature.

3.2.7.2 Validation of Uniform Flow

To ensure uniform distribution of the velocity in the wind tunnel, both visual and numerical validations were performed. Visual validation of the flow was achieved through fog testing with the additional baffles shown in Figure 32. Validation of uniform flow was achieved through 9 velocity profiles obtained with the LDV across the span of the wind tunnel. The average velocity in the along-wind direction, *U*, is shown below in Figure 56.

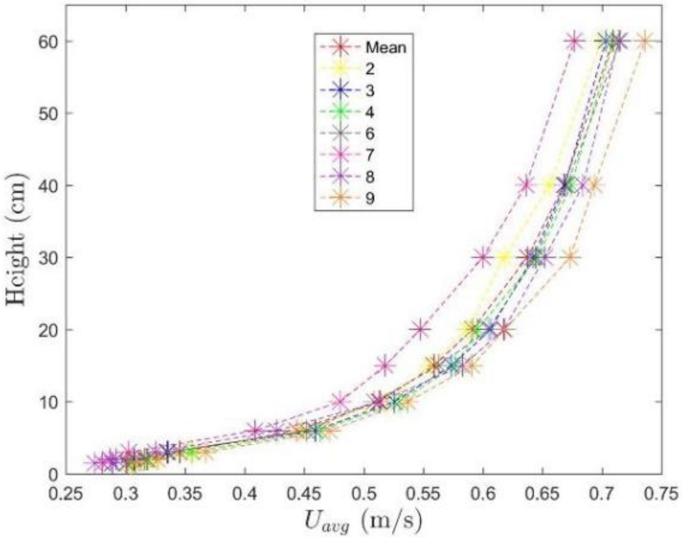

Figure 56. Average velocities in the along-wind direction from 9 velocity profiles measured with the LDV system taken with a single row of spires

From Figure 56, uniform velocity profiles are shown for the multiple locations. About 95% of the profiles are within 5% of the average velocity for each height. This shows that uniform velocities distribution in the along-wind direction across the span of the wind tunnel is achieved.

In addition to the velocities in each direction, other parameters were analyzed and compared across the wind tunnel. Results of the analysis for each of these parameters are located in the Appendix.

One important parameter is the friction velocity. The results of the friction velocity for each of the tests are shown below in Figure 57.

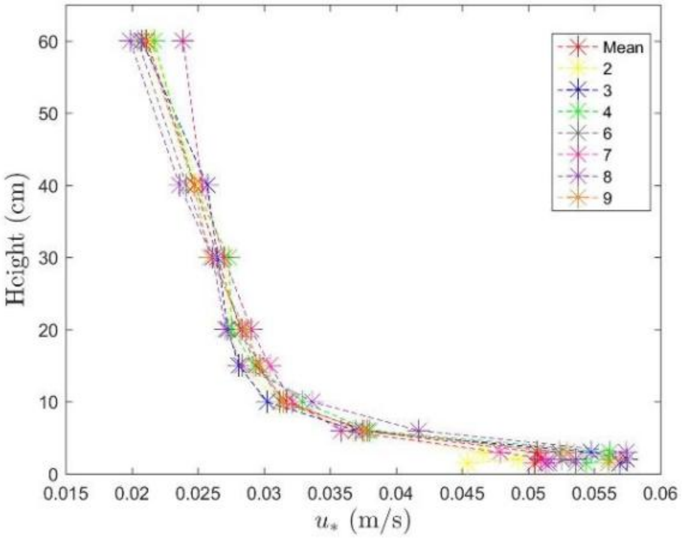

Figure 57. Friction velocities from 9 velocity profiles measured with the LDV system

From Figure 57, the friction velocity as a function of height is portrayed for each of the locations. The friction velocity is greater at locations closer to the ground, which is expected. After about 10 cm, the friction velocity decreases as a function of height. This relationship shows that a constant stress layer is achieved in the wind tunnel from the floor to a height of about 10 cm. This constant stress layer is developed from the surface roughness placed on the floor of the wind tunnel.

3.2.8 Constant Stress Layer

While the surface roughness and spires produce a constant stress layer of about 10 cm, an increased constant stress layer is desired. Increasing the constant stress layer would simulate the atmospheric boundary layer more accurately and increase the height in which tests can be performed ensuring they are within the constant stress layer for scaling. Different configurations of spires and surface roughness were tested to increase the height of the constant stress layer. A summary of the test parameters is shown below in Table 28.

Table 28. Table of Test Conditions for increasing constant stress layer

Test Condition	Rows of Spires	Characteristic Length (L) between Rows of Spires	Roughness Elements
1S_0L_NR	1	N/A	None
1S_0L_R	1	N/A	Applied
2S_0.5L_R	2	0.5 L	Applied
2S_1L_R	2	1 L	Applied
2S_2L_R	2	2 L	Applied
3S_1L_R	3	1 L	Applied

From the tests performed above, the constant stress layer was able to be increased to a height of about 40cm. Drag (friction) parameters – namely the friction velocity u_*, the relative depth of constant shear stress (*i.e.* ,the ratio of the thickness of the constant shear stress to the boundary layer thickness ${}^{z_{uw}}/_{\delta}$), and the coefficient of skin friction of the floor C_f were determined to ascertain the friction effects due to the use of Irwin spire-roughness arrangements. Two methods were used to compute the friction velocity u_*. The first method is based on the consideration of the streamwise flow in the region very near the wall[59]. For a flow of shear stress τ, density ρ, kinematic viscosity ν, vertical stream wise gradient $\frac{\delta U}{\delta z}$ and Reynolds shear stresses uw and vw the friction velocity according to the streamwise momentum equation near the wall is ${u_*}^2 = ({}^{\tau}/_{\rho}) = \sqrt{(uw^2 + vw)^2}$. With the present measurement technique, this value is readily accessible from the data by taking the average of the Reynolds shear stress measurements close to the wall that appears to be constant. The alternative method used is based on the validity of the classical log law $U = \frac{u_*}{\kappa}\ln(\frac{z-d}{z_o})$, where κ is the von Karman constant 0.4, d is the displacement length, and z_o

is the roughness length. By fitting the velocity profiles to the log law, u_* was obtained as the gradient of the plot. As shown in Figure 58. within the limits of uncertainties, the two methods yield almost equivalent values for the varying tests. At face value however, it appears that friction, velocity tends to increase with number of rows of spires, and characteristic length of spacing between spires.

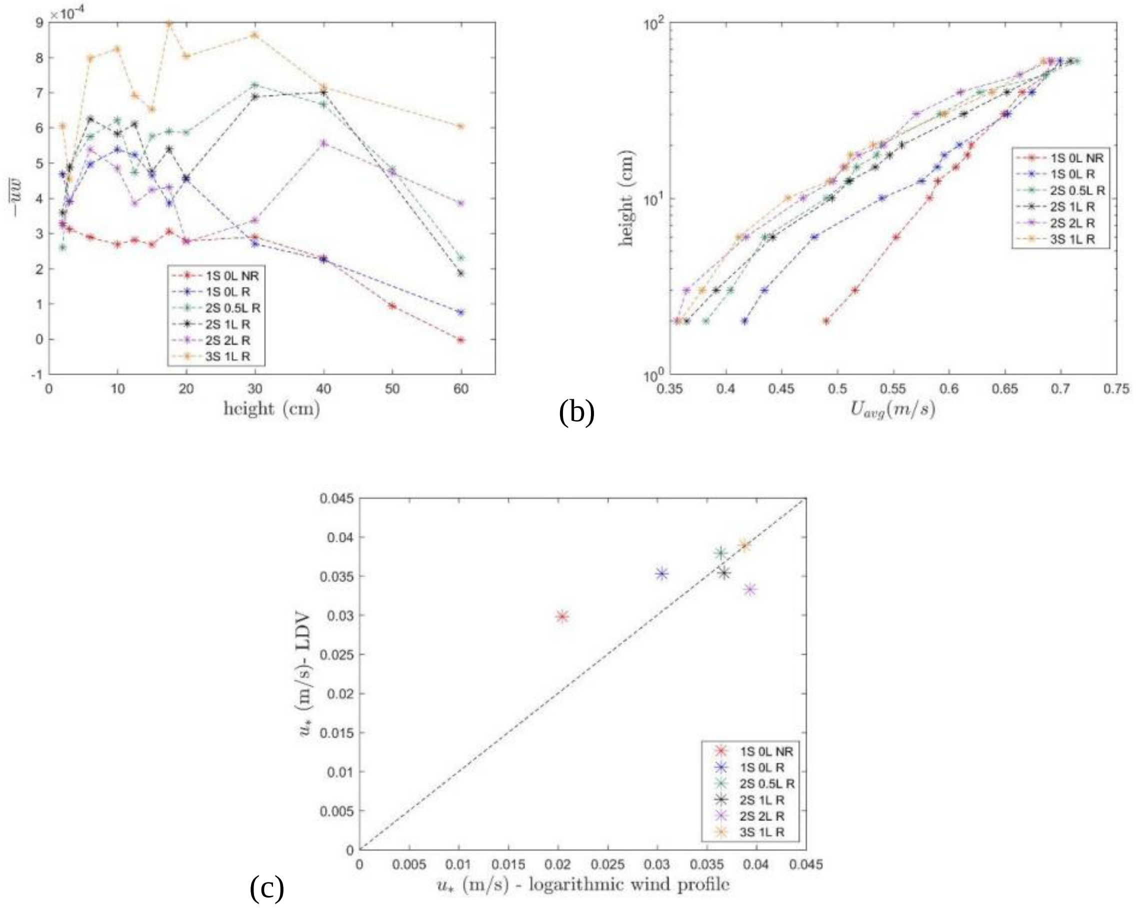

(a) (b) (c)

Figure 58. Drag friction parameters are shown with the Reynolds stress vs. height (a), logarithmic height vs. average wind speed (b) and the friction velocities solved with both methods (c)

By assessing the depth of the constant shear stress z_{uw} (*i.e.*, the depth of measurements for which the average shear stress was obtained), the relative depth of constant shear stress z_{uw}/δ was determined. As shown in Figure 58, the use of roughness in a spire-roughness arrangement (single row of spires) actually leads to a decrease in the constant shear stress thickness. On the other hand, this depreciation is cancelled when 2 or more rows of spires are used. The results show that the way to optimize the gain in constant shear stress thickness is not to increase the number of rows by more than 2, but to use 2 rows with a characteristic length spacing between rows limited to $1L$ (resulting in $^{z_{uw}}/_{\delta}$ = 0.84). The practical significance of this improvement is valuable in the experimental simulation of real-case scenarios such as the dispersion of pollutants from a line or area source.

The results of the tested performed resulted in a constant stress layer of 40 cm and turbulence intensities closer to atmospheric values simulating the atmosphere more accurately than other test configuration reported in the literature. This increased constant stress layer resulted in the certainty of all tests performed taking place within the constant stress layer resulting in more accurate scaling of the data with the same characteristic length.

3.2.9 Summary of Facility and Equipment

Overall, the Chemical Hazards Research Center and its equipment provide an excellent facility for the finite-duration area source releases. The wind tunnel is ultra-low speed and of a length sufficient for testing at longer downwind distances. The accurate delivery of gases and fastFID allow for accurate concentration-time histories with minimal time delay. The area source developed provides true finite-duration releases never before performed in an experimental program. The velocity profiles show uniform flow in 3D. The constant stress layer of 40 cm ensures the finite-duration releases are within the constant stress layer for accurate simulated atmospheric conditions.

3.3 Experimental Program

The experimental program in the ultra-low speed wind tunnel at the Chemical Hazards Research Center was established to determine an appropriate along-wind dispersion coefficient. From the first section, the along-wind dispersion has been predicted to be a function of a multitude of parameters. These parameters include wind speed, friction velocity, distance, and time. To account for all of the parameters and their relationships, a large test matrix was designed. An outline of the test conditions are shown below in Table 29.

Table 29. Test conditions performed for finite-duration releases

Parameter	Description
Wind Speeds	Two wind speeds were investigated (0.35m/s and 0.71m/s)
Release Rates	Two release rates were investigated ~1/10th the wind speed for each wind speed to mitigate entrainment effects
Release Locations	Three locations downwind will be investigated per wind speed (2, 4, and 8ft for 0.35 m/s and 4, 8, and 12ft for 0.71 m/s)
Release Durations	Release Duration of 30, 60 and 120 seconds were performed to assess the impact of along-wind dispersion on observed gas concentration
Ensemble Averages	65 replicate releases performed for ensemble averages for a given set of release conditions

With the above test conditions, all parameters were explored to determine their effect on along-wind dispersion. Each of the parameters will be discussed in the following sections with additional details as to why each of the specified values was chosen.

3.3.1 Wind Speeds

Two wind speeds of 0.35 m/s and 0.71 m/s were chosen for investigation. The wind speeds can be scaled from wind tunnel to field scales using the Froude number. The Froude number, *Fr*, is shown below

$$\boldsymbol{Fr} = \frac{\boldsymbol{u_o}}{\sqrt{\boldsymbol{g_o l_o}}} \tag{75}$$

where u_o is the velocity, $g_o$is gravity, and l_o is the characteristic length. With scaling, the Froude numbers are equivalent. For length scale ratios of 1:25, 1:50, and 1:100 wind speeds for both 0.35 m/s and 0.71 m/s are scaled to 1.75 m/s and 3.55 m/s, 2.5 m/s and 5 m/s, and 3.5 m/s and 7.1 m/s respectively. Some scaled values are portrayed in the figures to see the effect scaling has on the data but no scaling was performed in the analysis of the raw data reported in tables. If scaling is shown, it is clearly labeled.

3.3.2 Release Rates

Release rates were chosen so that the velocity from eh area source did not exceed 1/10th of the free stream velocity to avoid entrainment effects. The overall mass release rates are shown below.

Table 30. Release rates with respect to wind speed and mass

Wind Speed (m/s)	Release Duration (s)	Release Rate (lpm)	Release Rate of C_3H_6 (kg/s)
0.71	120	68	0.010517
0.71	60	68	0.005259
0.71	30	68	0.002629
0.35	120	34	0.005587
0.35	60	34	0.002794
0.35	30	34	0.001397

3.3.3 Release Locations

The area source was located 6.1 m downwind from the Irwin spires. This location has a fully established boundary layer in the wind tunnel. The fastFID was located at the height of 1cm from the ground at nominal distances of 2 ft, 4 ft, 8 ft, and 12 ft downwind from the edge of the area source tiles. The exact distance was an additional 0.5 feet from the edge of the area source tile to the edge of the physical area source release. For labeling purposes, the distances are labeled at nominal distances of 2 ft, 4 ft, 8 ft, and 12 ft downwind of the area source tiles. For numerical analysis, the exact distance from the fastFID to the downwind edge of the source was used.

3.3.4 Concentrations of Source

A 1% concentration of propane in air was used as the source gas for the test releases. With air having a density of 1.225 kg/m^3, and propane with a density of 1.882 kg/m^3, a 1% propane in air results in a density of 1.233 kg/m^3, which is neutrally buoyant. This concentration of propane in air was detected in sufficient amounts at all downwind locations in the test matrix. For larger downwind distances, an increased amount of propane would be needed to be measured by the FID. In pure nitrogen, the amount of propane can exceed the lower flammable limit (LFL. The out of service fuel concentration (OSFC) has been experimentally solved to be 6.2%[60]. Substituting nitrogen for air to increase the propane concentration and therefore increase the downwind distance was preliminarily tested. During calibration, an increase in sensitivity of the FID to nitrogen was found in addition to degradation of the instrument response.

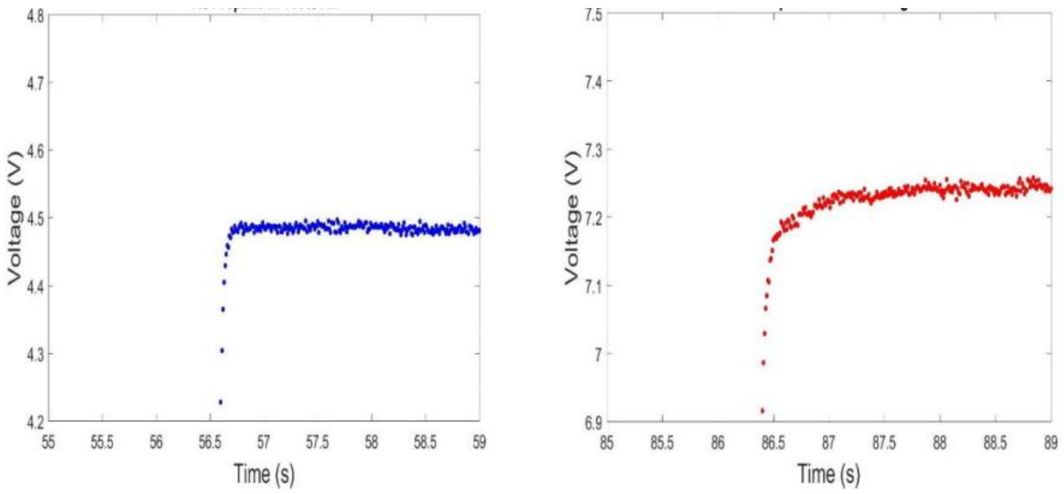

Figure 59. Comparison of calibration and time delay for 1% propane in air (left) and 1% propane in nitrogen (right) introduced, with both reporting values of 0V at 0% propane

At 0% propane in either air or nitrogen, a voltage of 0 is observed. For 1% propane in air, a voltage of ~4.5V is observed. For 1% propane in nitrogen, a voltage of ~7.25 is observed. When the carbon bonds are ionized with excess nitrogen, carbon ions seem to be ionizing with the nitrogen resulting in a larger observed voltage. When performing finite-duration releases in the wind tunnel, the volume of 3% propane in balance nitrogen is unable to produce the same concentration-time histories for propane in air shown below in Figure 60 for the same location, wind speed, and release duration.

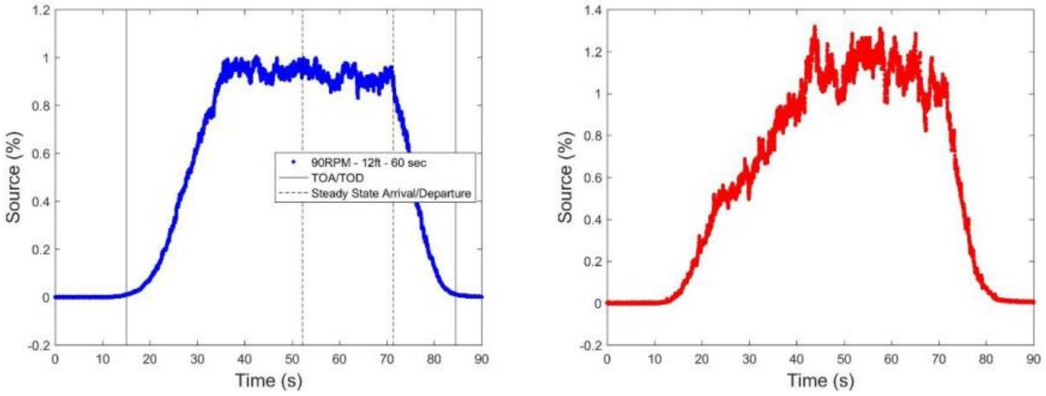

Figure 60. Comparison of ensembles of 60-sec release at 12 ft and 0.71 m/s of 1% propane in air (left) and 3% propane in nitrogen (right)

From Figure 60, it is shown that nitrogen has an overall effect on the leading edge of the cloud. Both tests are expected to be equivalent. While they show similar steady-state concentrations, a delay in the signal is shown for the leading edge. It is believed to be caused by the sensitivity of the FID to nitrogen. For consistency throughout the experimental program, only 1% propane in air was used and reported.

3.3.5 Release Durations

Three release durations were chosen for each of the locations and wind speed combinations. A 120-second release duration was chosen across all the locations and wind speeds providing a release in which steady-state concentration levels were observed based on comparison with 10-minute release durations. The 120, 60, and 30-second releases were performed at all release locations and wind speeds finalizing the test matrix.

3.3.6 Ensemble Averages

In the atmosphere, there are large variations in turbulence and wind direction resulting in concentration fluctuations. Ensemble averages are the average of multiple tests under the same conditions to determine release concentrations averaged over a function of time. To see the average of non-rare events with a 95% confidence interval, 28 individual tests need to be performed, according to Wilson[61]. A starting point of 35 individual tests was performed to see how the data collapsed. Increased variations were observed at distances closest to the area source, while decreased variations were observed at distances farthest from the area source. To keep testing consistent across all tests, 65 individual tests were performed for all variations in test conditions. This quantity allowed for a collapse of data to be within 1% of the total average with respect to fluctuations and a standard deviation of 0.05 for all concentration profiles. If a test did not visually collapse as well as other tests, additional trials were performed up to 100 tests or more in the ensemble average. With ensemble averages, a clearer picture of cloud characteristics can be observed.

3.3.7 Summary of Test Conditions

A total of 18 sets of test conditions, with 65 ensemble averages each, are included in the test matrix to encompass all parameters shown below in Table 31.

Table 31. Test conditions performed for finite-duration releases

test	Source C_3H_8 (%)	U (m/s)	U_{1cm} (m/s)	u_* (m/s)	distance (m)	release duration (s)
6	1	0.71	0.224	0.036	1.37 (4ft)	120
5	1	0.71	0.224	0.036	1.37 (4ft)	60
8	1	0.71	0.224	0.036	1.37 (4ft)	30
9	1	0.71	0.224	0.036	2.59 (8ft)	120
10	1	0.71	0.224	0.036	2.59 (8ft)	60
12	1	0.71	0.224	0.036	2.59 (8ft)	30
30	1	0.71	0.224	0.036	3.81 (12ft)	120
31	1	0.71	0.224	0.036	3.81 (12ft)	60
33	1	0.71	0.224	0.036	3.81 (12ft)	30
17	1	0.35	0.102	0.015	0.8 (2ft)	120
18	1	0.35	0.102	0.015	0.8 (2ft)	60
19	1	0.35	0.102	0.015	0.8 (2ft)	30
21	1	0.35	0.102	0.015	1.37 (4ft)	120
22	1	0.35	0.102	0.015	1.37 (4ft)	60
23	1	0.35	0.102	0.015	1.37 (4ft)	30
25	1	0.35	0.102	0.015	2.59 (8ft)	120
27	1	0.35	0.102	0.015	2.59 (8ft)	60
28	1	0.35	0.102	0.015	2.59 (8ft)	30

With the ensemble averages of 65 individual tests or more performed for each set of test conditions, over 2,000 tests were performed. From the varying test conditions, appropriate relationships between the different parameters can be found in order to determine an along-wind dispersion coefficient.

3.4 Discussion of Analysis of Results

The analysis performed in this experimental program takes into consideration past methods performed for data analysis of experimental releases. Some methods applied in the analysis are new, but of higher caliber due to the quantity of releases which allows for ensemble averages to be performed. The ensemble averages, background concentration, time of arrival, time of departure, steady-state, time averaging, effective wind speed, and determination of the distribution constants are all discussed in this section with respect to prior experimental programs.

3.4.1 Ensemble Averages:

A sample rate of 100 Hz was used to record measurements with the fastFID. Ensemble averages were then performed across tests in an ensemble for each individual sample time (with increments of 0.01 seconds). All figures show the final ensemble average for each of the tests unless otherwise stated.

3.4.2 Background Concentration:

With the wind tunnel operating within a closed room, the background concentration increased as a function of time. To account for the background concentration, the first 100 data points, or 1 second, were averaged from the beginning of the release and subtracted from the overall concentration profile for each test. A similar method was performed by Hall[62] in 1996 with the first 20 samples (0.2 seconds) to provide a “sensor zero” for each test. For tests of longer release durations, venting the wind tunnel was required before or during tests. Repeated venting was performed when the background concentration exceeded 0.020V as indicated by the FID when measuring concentration between cloud releases.

3.4.3 Time of Arrival (TOA)

Time of arrival (TOA) is determined when the cloud has arrived at the concentration sensor. The exact concentration value where background concentration (or noise) is exceeded by the cloud concentration has been quantified by different methods in the past. In denser-than-air gases released in a wind tunnel, Hall[62] determined when the background concentration exceeded 0.1% of the source, time of arrival was achieved. For the 0.1% of the source concentration, the reliability of this method varies due to lower concentrations at increased downwind distances. For distances closer to the source, using a 0.1% criteria of the source concentration was easily found when <1% of the maximum measured concentration was 1%. For distances further downwind, 0.1% of the source concentration was not easily found because maximum concentration was only about 1% of the source. The 3% of the maximum concentration was a consistent method for determination of the TOA for each cloud. While this method is consistent for all concentrations, the 3% level seemed high and disregarded a large amount of the leading edge of the cloud. Choosing a value based on the maximum concentration for each profile was preferred due to variation in distances to keep the methods consistent across multiple distances. The TOA was determined when the ensemble average exceeded 1% of the maximum concentration of the ensemble. The TOA so determined was consistent with the wind speed measured at the fastFID sample height.

3.4.4 Time of Departure (TOD)

Time of departure is determined when the cloud has fully passed, or departed, from the concentration sensor. Depending on the time delay in the concentration measurement apparatus, the concentration can still be lingering in the signal from the machine when the cloud has fully passed. The fastFID response time was measured to be 10mS. Hall measured similar response time for a similar instrument[63]. The accuracy of the cloud departure was not in question due to the response time of the fastFID for this experimental program. For data analysis of prior field tests with concentration sensors with longer response times due to equipment response times, a different approach must be used to determine an appropriate time of departure. A 0.1% of the source concentration has never been used in past data analysis, presumably due to the response time of the instrument used. A 3% of the maximum concentration has been used in past analysis [62]. Similar conservation of mass issues seen with the 3% max with the TOA is seen with the TOD. As with the TOA, the TOD was determined when the ensemble average fell below 1% of the maximum ensemble concentration.

3.4.5 Time Averaging

No time averaging was applied to the tests performed in the wind tunnel. Wilson[64] believes in wind tunnels meandering is suppressed due to sidewalls constraining the flow, resulting in time averaging needing to be 1-5 minutes. This relationship is shown below in Figure 61.

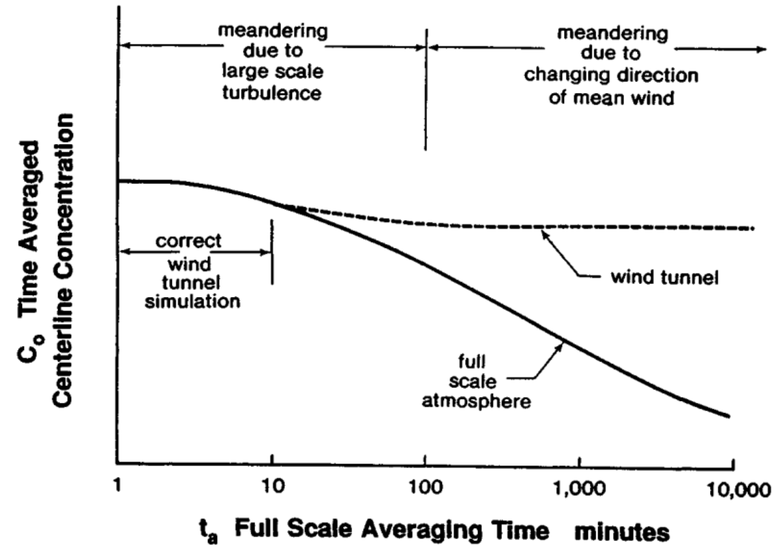

Figure 61. Figure 4.2 (book). Wind tunnel limitations for simulating averaging time effects on plume dispersion in a steady long-established release.

With the short duration of the releases performed, all 2 minutes or less, no time averaging was applicable with the prior definition by Wilson. Time averaging is used in individual releases to capture the span of the entire path of the cloud due to meander and more accurate modeling of the centerline concentration. The area source results in the cloud being present across the centerline for all downwind distances. With ensemble averages, time averaging is not required. After ensemble averages were captured, binning was investigated, but not used. Times of 0.05, 0.1, 0.5, and 1 second were looked into with binning or grouping of the data. Binning minimized the fluctuations in concentrations during steady-state periods.

3.4.6 Time of Steady-State or Peak Arrival and Departure

Due to fluctuations in the concentration over time, there was no set period in which the steady-state or peak concentration was exceeded and held constant. A method for determining the time in which steady-state was achieved was difficult to determine due to these fluctuations. A moving average was applied to the ensemble averages for a smoother transition and easier determination of when steady-state or the peak concentration was achieved. Moving averages of 2-10 seconds were applied to the different test conditions to determine when steady-state was achieved. This method provided a useful measure of time of steady-state or peak arrival (TOPa) when the average concentration achieved a maximum value through quantification of the derivative of the moving average equal to essentially zero (<0.001). Depending on the release duration, steady-state may or may not have been achieved. Steady-state was achieved for the 60- and 120-second releases whereas the 30-second releases never reached steady-state, but this duration did have a clear peak in concentration. For the 60- and 120-second releases, TOPa and time of steady-state or peak departure (TOPd) were quantified as two separate values whereas the 30-second releases only had one value, solely for the peak. While the moving average method was able to smooth out the fluctuations in concentration to determine when the average concentration reached steady-state for the leading edge, the moving average distorted the tail end of the cloud, which is characterized by the quick drop off in concentration. This distortion occurred due to the decreased upwind dispersion compared to the larger downwind dispersion that was not affected by the moving average. Time of steady-state or peak departure was determined when the concentration was last at steady-state before dropping off with the trailing edge of the cloud.

3.4.7 Steady-State Concentration

For this analysis, the steady-state concentration was determined when the moving average across the period in which steady-state was achieved covered 50% of the release duration and the moving average across 25% of the cloud varied less than 0.1%. These criteria were consistent with the visual interpretation of the data in the 120-second release data. For shorter duration releases, 30-

and 60-seconds, the concentration was determined to reach steady-state if the concentration reached the steady-state that was achieved at the 120-second release duration. The 30-second releases never reached steady-state for any set of test conditions whereas all 60-second releases achieved steady-state.

3.4.8 Temperature and Pressure Correction in Flow Rates

Gases are delivered through an MKS Mass Flow Controller, static mixer, and dead space discussed previously. The MFCs are calibrated by the manufacturer at standard temperature and pressure. Adjustments were made for the temperature and pressure each day based on previous measurements and using the ideal gas law. The standard condition flow rate ranged between 65.4 and 72.4 LPM. For tests of the same downwind distances and wind speeds, all tests were performed on the same day or span of days, resulting in similar temperatures and pressures and therefore release rates. For some tests, all release durations were unable to be performed in the same time period due to issues with the tunnel fans. This resulted in one or two of the test conditions for the same distance and wind speed to have a different standard condition release rate for the different temperature and pressure. An example of this is shown below for the 0.71 m/s wind speed and distance of 4ft. This effect is thought to explain the difference between experiments seen in Figure 62.

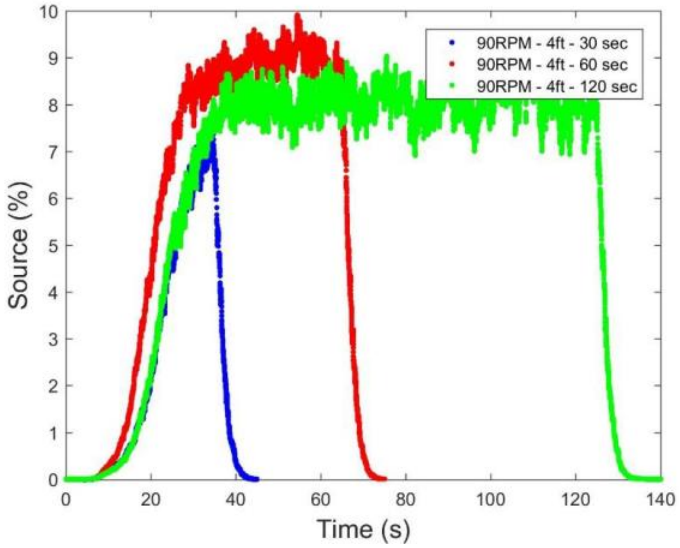

Figure 62. Comparison of concentrations at 0.71 m/s, 4 ft, and all release durations

The 120-second and 30-second releases were performed within 2 days of each other. The 60-second release had only 35 tests performed in the 2 day period. An additional 65 tests were performed about 20 days later to meet the 65 test ensemble average standardization. The 60-second release rate was slightly larger than the other two release rates due to pressure and temperature that day. This resulted in the concentration for 60-seconds to be slightly larger, about 1%, than the steady-state of the 120-second release duration. A correction for the concentration can be applied to the clouds based on release rates resulting in similar steady-state values. This correction is shown below in Figure 63.

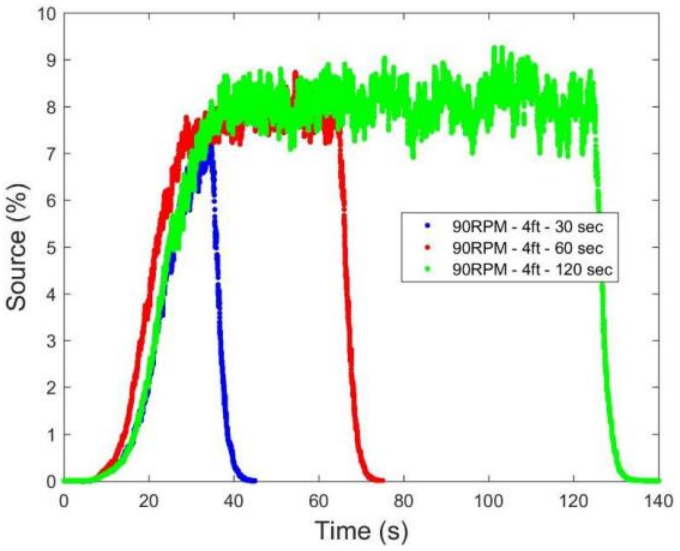

Figure 63. Comparison of concentrations at 0.71 m/s, 4 ft, and all release durations

From Figure 63, the steady-state concentrations are equivalent, which is expected due to the correction. However, a correction could not be applied for the acceleration of the cloud. The increased release rate resulted in the cloud accelerating at a slightly faster rate than the slower release durations. The 60-second release reaches the concentration sensor slightly faster than the other two releases seen in the space between the leading edges of the plot in Figure 63 resulting in slight shifts in both the TOA and TOPa. This shift had no effect on the time distribution coefficient which is very similar with values of 9.70 for the 120-second release and 9.97 for the 60-second release.

While the release rates were corrected for the daily temperature and pressure, there were only 4 tests out of all tests that were slightly different from the steady-state conditions due to release rates. It was noted that for these tests, the day in which they were taken did not have the same temperature and pressure as the other tests. For tests taken in the same few days, no adjustment was needed.

Atmospheric pressure can be measured with an electronic sensor and mercury barometer. When the electric sensor was new, it’s readings agreed with the barometer’s readings but a discrepancy was found in the two instruments after the test program was complete. Calibration of the mercury barometer is planned since it should be more stable than the electronic sensor which requires more frequent calibration.

3.4.9 Moments (Skewness and Kurtosis)

To determine how Gaussian the distributions are over the ensemble averages for individual test conditions, moments were investigated. The 1st and 2nd moments resulted in mean and variance which were determined for the overall ensemble averages as well as for the steady-state periods. Additional moments were investigated to determine the skewness and kurtosis of the ensemble averages. A sample of the skewness and kurtosis for the 60-second release at 4ft downwind and 0.71m/s wind speed is shown below.

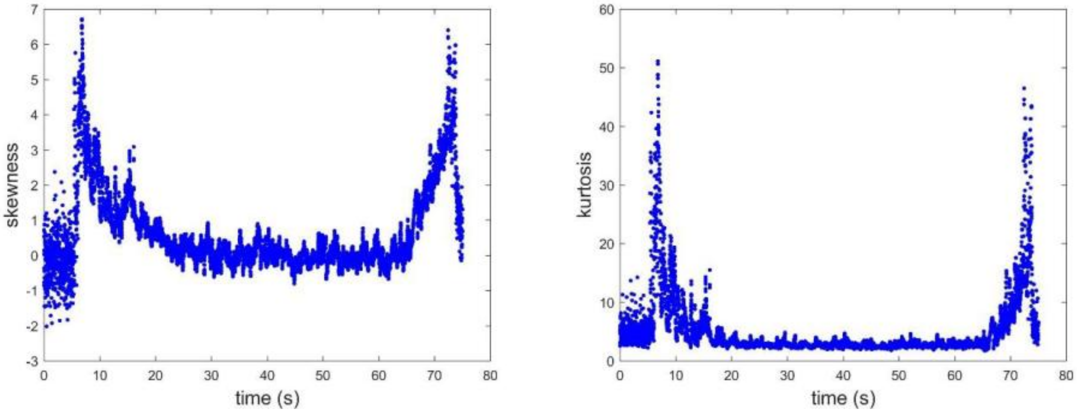

Figure 64. Skewness (left) and kurtosis (right) for test 5 at 0.71 m/s, 4 ft and 60-sec release

The optimal skewness and kurtosis values are 0 and 3 for a Gaussian distribution. For the periods of “steady-state,” Gaussian distributions are visually achieved. From both figures, peaks are shown to be at similar locations corresponding with the time of arrival and time of departure. The peaks of the moments were not consistent across all test conditions to use to quantify the time of arrival or departure consistently. While the moment's method did not determine the time of arrival or time of departure, the ensemble averages did show that a Gaussian distribution was observed.

3.4.10 Determination of Effective Wind Speed, Ue

The effective wind speed is commonly used in dispersion modeling the speed at which the cloud is traveling through the atmosphere. Effective wind speeds are commonly derived from the distance traveled divided by the travel time. For the finite-duration releases performed, the distance was measured from the trailing edge of the area source to the concentration sensor. For travel times, the value was not as clear as the distance. The TOA, TOPa, and TOD were all used for the determination of the effective wind speeds. The time of arrival was found to be most consistent with the measured wind speeds at 1 cm elevation shown in Table 32.

Table 32. Results of effective wind speeds using time of arrival (TOA) for time

test	U (m/s)	U_{1cm} (m/s)	Dist. (m)	Dur. (s)	TOA (s)	Ue (m/s)
6	0.71	0.224	1.37 (4ft)	120	8.86	0.15
5	0.71	0.224	1.37 (4ft)	60	8.24	0.17
8	0.71	0.224	1.37 (4ft)	30	8.53	0.16
9	0.71	0.224	2.59 (8ft)	120	11.28	0.23
10	0.71	0.224	2.59 (8ft)	60	13.53	0.19
12	0.71	0.224	2.59 (8ft)	30	12.38	0.21
30	0.71	0.224	3.81 (12ft)	120	15.17	0.25
31	0.71	0.224	3.81 (12ft)	60	15.07	0.25
33	0.71	0.224	3.81 (12ft)	30	14.73	0.26
17	0.35	0.102	0.8 (2ft)	120	10.67	0.07
18	0.35	0.102	0.8 (2ft)	60	10.76	0.07
19	0.35	0.102	0.8 (2ft)	30	8.38	0.09
21	0.35	0.102	1.37 (4ft)	120	12.71	0.11
22	0.35	0.102	1.37 (4ft)	60	11.59	0.12
23	0.35	0.102	1.37 (4ft)	30	11.00	0.12
25	0.35	0.102	2.59 (8ft)	120	16.55	0.16
27	0.35	0.102	2.59 (8ft)	60	16.98	0.15
28	0.35	0.102	2.59 (8ft)	30	16.72	0.15

While the effective wind speeds are similar to the measured wind speeds at the same vertical distance, they are not equivalent at all distances. As the cloud travels downwind, the effective wind speed becomes larger. These effects can be attributed to the effect of vertical dispersion on the cloud. Initially, the cloud has no momentum in the x-direction when releasing from the area source. As the cloud begins to accelerate due to the tunnel flow, the effective wind speed will be less than the wind speed at the measured height (1 cm). As the cloud travels downwind, higher speed tunnel flow will be entrained at the leading edge of the cloud which will ultimately cause the effective wind speed to be larger than the wind speed measured at 1 cm. Similar effects have been observed in other experimental programs from ground level releases[65]. The effective wind speed reaches or exceeds the measured wind speed at the same height for the 2nd and 3rd downwind distances for each wind speed observed.

3.4.11 Previous Determination of Time Distribution Coefficient, σ_t

Analysis of experimental data to determine σ_x is typically based on analysis of concentration-time histories to determine the time-based distribution coefficient, σ_t. With the effective wind speed, σ_x is estimated by $\sigma_t u_e$. One approach used in the previous analysis of experimental programs to determine σ_t was based on a Gaussian distribution

$$\boldsymbol{\sigma_t = \frac{\Delta T - T_{dur}}{4.3}} \tag{76}$$

where ΔT is the total cloud time and T_{dur} is the duration of the release[66]. As depicted in Figure 65, this approach assumes that there are Gaussian tails on both ends of a constant concentration region of the same duration as the source.

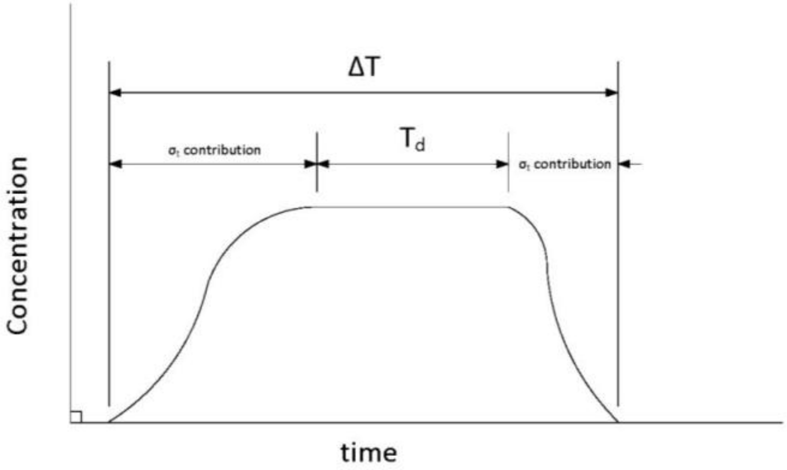

Figure 65. Hypothetical concentration-time history by Hanna and Chang to determine σ_t[66]

With this approach, the effects of σ_t and σ_x only act on the leading and trailing edges of the cloud and not on the steady-state period. This approach was taken to determine σ_x from single realization data sets and was largely unquestioned because of the lack of data. Figure 66 shows the ensemble concentration-time history of a 30-second release at the 4ft location.

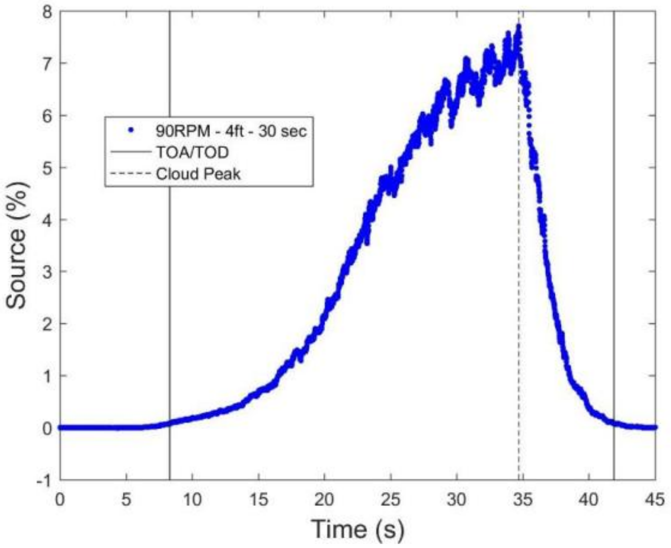

Figure 66. Concentration-time history for 30-second release in 0.71 m/s at 4 ft downwind

In this case, the TOA and TOD difference is not much larger than the release duration T_{dur}. With equation (76), the estimate of σ_t is around 1.2 s. By contrast, consider Figure 67 which is the ensemble concentration-time history for a 120-second release for the same location.

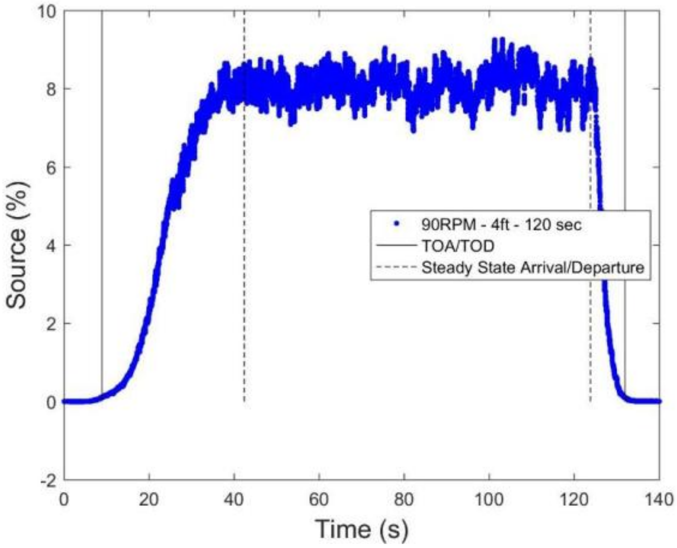

Figure 67. Concentration-time history for 120-second release in 0.71 m/s at 4 ft downwind

This release shows characteristics more like Figure 65, but the duration of constant concentration is much less than 120-seconds. These ensemble concentration-time histories are representative of these experiments. The leading edge of the cloud (earliest concentration measurements) shows an increase in concentration that is much slower than the trailing edge which rapidly decreases. For longer releases, there is a period of constant concentration that is the same as that of a steady-state release, but the duration of this period is significantly less than the release duration. For shorter release durations, the observed maximum concentration is less than the steady-state maximum concentration.

3.4.12 Determination of σ_t through Individual Test Results

In field tests, ensemble averages are impractical due to cost and repeatability with varying test conditions such as wind speed, direction, and stability class. Concentration-time histories captured in a field test would be similar to a single wind tunnel test. An example of a single test in comparison to the ensemble of 100 tests is shown in Figure 68.

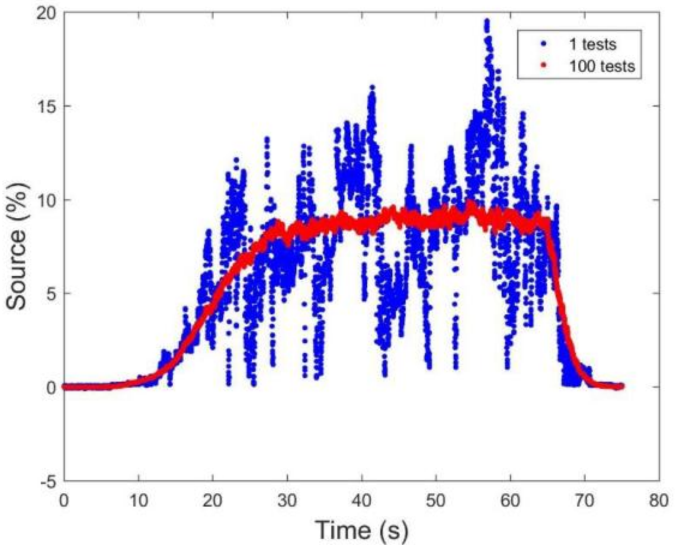

Figure 68. Concentration-time history for 120-second release in 0.71 m/s at 4 ft downwind for both 1 individual test (blue) and 100 ensemble averages (red)

From individual tests, the time of arrival and time of departure can be measured, but determination of any constant concentration period would be difficult. The ensemble averaged behavior provides a much clearer picture of the cloud behavior.

3.4.13 Determination of σ_t

The concentration-time histories were analyzed to determine appropriate estimated of σ_t by taking into account the period of constant (steady-state) concentration. Denoting the time of peak arrival and time of peak departure as TOPa and TOPd, respectively, the time period representing along-wind dispersion at the leading edge would be TOPa – TOA and at the trailing edge would be TOD-TOPd. These times are shown in the concentration-time history in Figure 67.

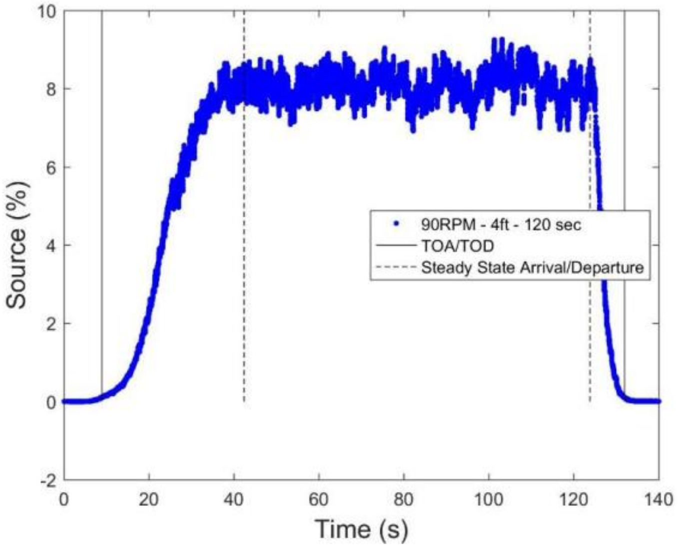

Figure 67. Concentration-time history for 120-second release in 0.71 m/s at 4 ft downwind

At long distances from the source, the distinction between leading and trailing edges are expected to disappear so determination of σ_t taking into account the both the leading and trailing edges would be advantageous. Consequently, σ_t was evaluated as:

$$\boldsymbol{\sigma_t = \frac{leading\ edge + trailing\ edge}{4.3} = \frac{(TOPa - TOA) + (TOD - TOPd)}{4.3}} \qquad \textbf{(77)}$$

This approach can be applied to all measurements here. For shorter release durations, the TOPa and TOPd are the same values.

3.5 Results and Discussion

Results of the finite-duration release experiments are analyzed in the following section. All ensembles classified by distance and release duration are located in the appendix. Ensembles with their TOA, TOD, TOPa, and TOPd are also located in the appendix. An overall recommendation for the time distribution constant and along-wind dispersion constant is achieved from these finite-duration releases.

3.5.1 Concentration-Time Histories

For the 120- and 60-second releases, the steady-state maximum concentration was measured. For the 60-second releases, the maximum measured concentration is significantly shorter for the same test conditions compared to the 120-second releases and is effectively zero for the low wind speed tests. For the 30-second releases, the maximum concentration (peak) did not always reach the maximum steady-state concentration for the same downwind distance and wind speed. All trends can be observed in the ensemble concentration-time histories plotted as a function of the downwind distance and wind speed shown in Figure 69.

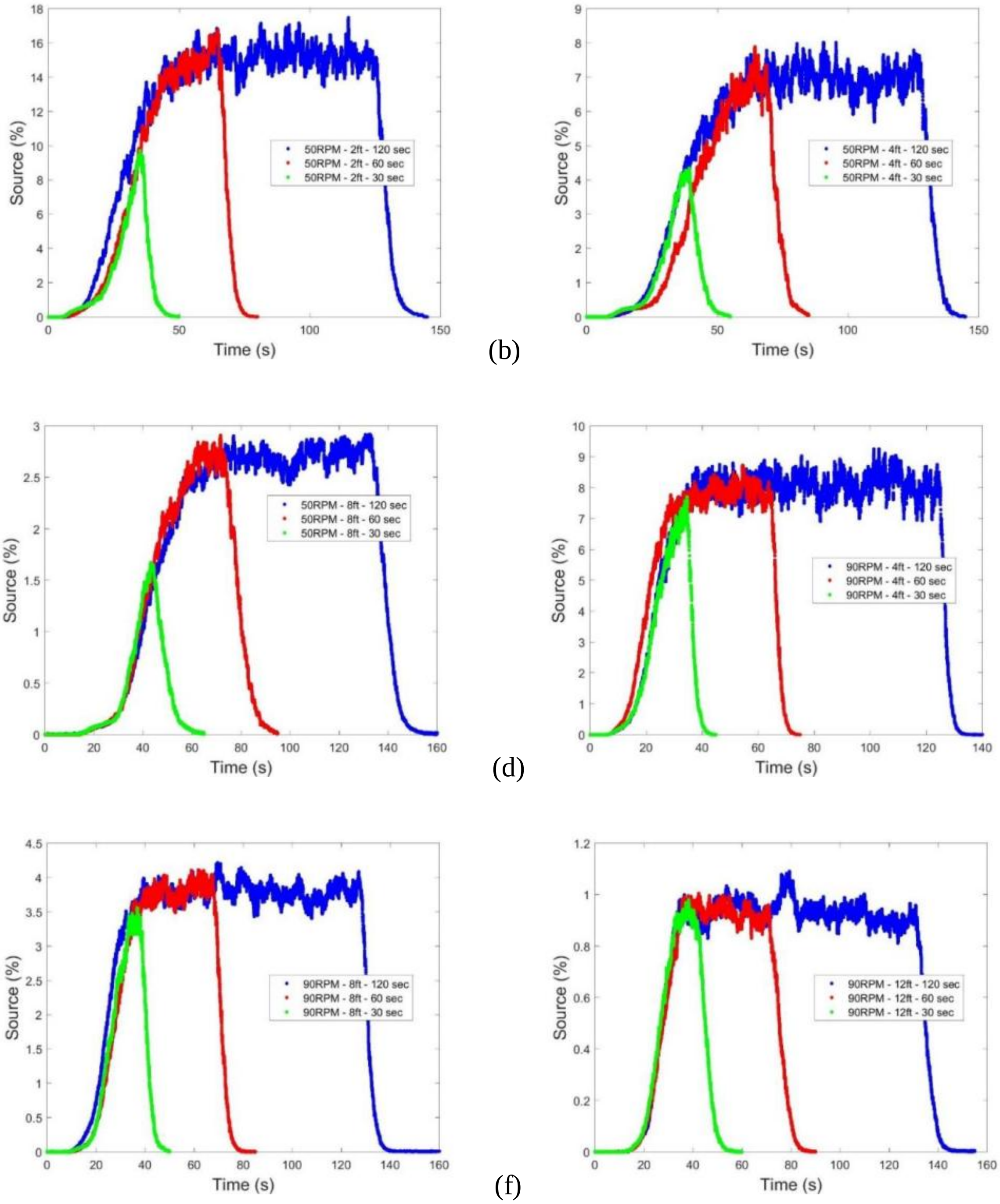

(a) (b)

(c) (d)

(e) (f)

Figure 69. All finite-release durations at downwind distances of 2 ft (a), 4 ft (b), and 8 ft (c) for 0.35 m/s and 4 ft (d), 8 ft (e), and 12 ft (f) for 0.71 m/s

As expected, the effect of along-wind dispersion increases with downwind travel (in distance and time). For both the 60- and 120-second releases, the impact of along-wind dispersion at the leading edge and trailing edge are very comparable. For the 30-second releases, the impact of along-wind dispersion on the leading edge doesn't see the full effects as compared to the longer release durations. The 30-second releases do not always reach the steady-state maximum concentration due to the transfer of mass from the steady-state concentration to the leading and trailing edges, thus decreasing the steady-state duration and maximum concentration achieved. Additional graphs for the experiments by the release durations are included in the appendix.

3.5.2 TOA, TOD, TOPa, and TOPd

The time of arrival (TOA) and time of departure (TOD) as well as the time peak arrival (TOPa) and departure (TOPd) were determined for each ensemble. Plots of the ensemble concentration-time histories showing the TOA, TOD, TOPa, and TOPd are shown in the appendix and summarized in Table 33. To determine σ_t for the leading edge, a Gaussian distribution was assumed for that portion of the time history and calculated as

$$\boldsymbol{\sigma_{ta} = \frac{leading\ edge}{2.15} = \frac{(TOPa - TOA)}{2.15}} \tag{78}$$

with a similar approach for the trailing edge, σ_{td}. As expected, $\sigma_{ta} > \sigma_{td}$. Using the previous approach for estimating σ_t, results in $\sigma_t = {}^{(\sigma_{ta} + \sigma_{td})}/_{2}$. From this relationship, the along-wind dispersion coefficient can be estimated with $\sigma_x = \sigma_t u_e$. Values of each of these parameters are summarized in Table 33.

Table 33. Summary of analyzed data from experimental test program

test	U (m/s)	U_{1cm} (m/s)	u_* (m/s)	Dist. (m)	Dur. (s)	TOA (s)	TOD (s)	TOPa (s)	TOPd (s)	Ue (m/s)	σ_{ta} (s)	σ_{td} (s)	σ_t (s)	σ_x (m)
6	0.71	0.224	0.036	1.37	120	8.86	132.01	42.45	123.90	0.155	15.62	3.77	9.70	1.50
5	0.71	0.224	0.036	1.37	60	8.24	71.71	44.40	65.00	0.166	16.82	3.12	9.97	1.66
8	0.71	0.224	0.036	1.37	30	8.53	41.76	34.70	34.70	0.161	12.17	3.28	7.73	1.24
9	0.71	0.224	0.036	2.59	120	11.28	138.46	45.43	128.40	0.230	15.88	4.68	10.28	2.36
10	0.71	0.224	0.036	2.59	60	13.53	77.88	43.96	67.80	0.191	14.15	4.69	9.42	1.80
12	0.71	0.224	0.036	2.59	30	12.38	47.70	36.90	36.90	0.209	11.40	5.02	8.21	1.72
30	0.71	0.224	0.036	3.81	120	15.17	144.23	52.19	131.50	0.251	17.22	5.92	11.57	2.91
31	0.71	0.224	0.036	3.81	60	15.07	84.49	52.24	71.37	0.253	17.29	6.10	11.70	2.96
33	0.71	0.224	0.036	3.81	30	14.73	53.37	38.26	38.26	0.259	10.94	7.03	8.99	2.32
17	0.35	0.102	0.015	0.76	120	10.67	141.67	58.50	126.40	0.071	22.25	7.10	14.67	1.05
18	0.35	0.102	0.015	0.76	60	10.76	75.05	57.31	64.90	0.071	21.65	4.72	13.19	0.93
19	0.35	0.102	0.015	0.76	30	8.38	44.56	35.10	35.10	0.091	12.43	4.40	8.41	0.77
21	0.35	0.102	0.015	1.37	120	12.71	141.65	66.20	128.00	0.108	24.88	6.35	15.61	1.68
22	0.35	0.102	0.015	1.37	60	11.59	83.73	63.25	68.80	0.118	24.03	6.94	15.49	1.83
23	0.35	0.102	0.015	1.37	30	11.00	51.13	39.40	39.40	0.125	13.21	5.46	9.33	1.16
25	0.35	0.102	0.015	2.59	120	16.55	151.96	74.47	133.30	0.157	26.94	8.68	17.81	2.79
27	0.35	0.102	0.015	2.59	60	16.98	93.37	63.34	74.00	0.153	21.56	9.01	15.29	2.33
28	0.35	0.102	0.015	2.59	30	16.72	61.14	43.30	43.30	0.155	12.36	8.30	10.33	1.60

For each set of test locations at the same wind speed and varying release durations, the TOA is similar, but not identical. Note that at shorter distances downwind, the TOA shows more variation than at the longest distance for each test. In fact, it seems this variation in the TOA become negligible as the time after the release increases (the longest distances have TOA values greater than about 15 s). TOD clearly depends on the release duration. For the same release durations, the TOD increases as the distance increases, as expected. For TOPa, 60- and 120-second release duration tests have similar values, also as expected. Estimated TOPa values for tests 30 and 31 seem to be a bit large when compared with the 30-second test at the same conditions in Figure 69(f). This seems to be an artifact of how TOPa is determined with the moving average method and these tests having a bit more fluctuations in concentrations. Table 34 summarizes ratios of σ_t non-dimensionalized with TOA, TOD, TOPa, and TOPd.

Table 34. Summary of $^{\sigma_t}/_{t}$ for different times and $^{\sigma_x}/_{x}$ for the only distance

test	U (m/s)	Distance (m)	Duration (s)	σ_t/TOA	σ_t/TOD	σ_t/TOPa	σ_t/TOPd	σ_x/x
6	0.71	1.37	120	1.09	0.07	0.23	0.08	1.09
5	0.71	1.37	60	1.21	0.14	0.22	0.15	1.21
8	0.71	1.37	30	0.91	0.19	0.22	0.22	0.91
9	0.71	2.59	120	0.91	0.07	0.23	0.08	0.91
10	0.71	2.59	60	0.70	0.12	0.21	0.14	0.70
12	0.71	2.59	30	0.66	0.17	0.22	0.22	0.66
30	0.71	3.81	120	0.76	0.08	0.22	0.09	0.76
31	0.71	3.81	60	0.78	0.14	0.22	0.16	0.78
33	0.71	3.81	30	0.61	0.17	0.23	0.23	0.61
13	0.71	5.03	120	0.99	0.12	0.24	0.13	0.99
14	0.71	5.03	60	0.96	0.19	0.23	0.22	0.96
15	0.71	5.03	30	0.53	0.16	0.22	0.22	0.53
17	0.35	0.76	120	1.38	0.10	0.25	0.12	1.38
18	0.35	0.76	60	1.23	0.18	0.23	0.20	1.23
19	0.35	0.76	30	1.00	0.19	0.24	0.24	1.00
21	0.35	1.37	120	1.23	0.11	0.24	0.12	1.23
22	0.35	1.37	60	1.34	0.18	0.24	0.23	1.34
23	0.35	1.37	30	0.85	0.18	0.24	0.24	0.85
25	0.35	2.59	120	1.08	0.12	0.24	0.13	1.08
27	0.35	2.59	60	0.90	0.16	0.24	0.21	0.90
28	0.35	2.59	30	0.90	0.25	0.24	0.35	0.90

As expected,

$$\frac{\boldsymbol{\sigma_x}}{\boldsymbol{x}} = \frac{\boldsymbol{\sigma_t}}{\boldsymbol{TOA}} \tag{79}$$

because u_e was taken to be $^{x}/_{TOA}$. It is interesting to note that $^{\sigma_t}/_{TOPa}$ is essentially constant over all test conditions.

3.5.3 Comparison of σ_t and σ_x with previous data

Past field and wind tunnel data were analyzed in the second section of the dissertation. The results from this experimental program are added to the previous data in Figure 70 using the TOPa as the time scale.

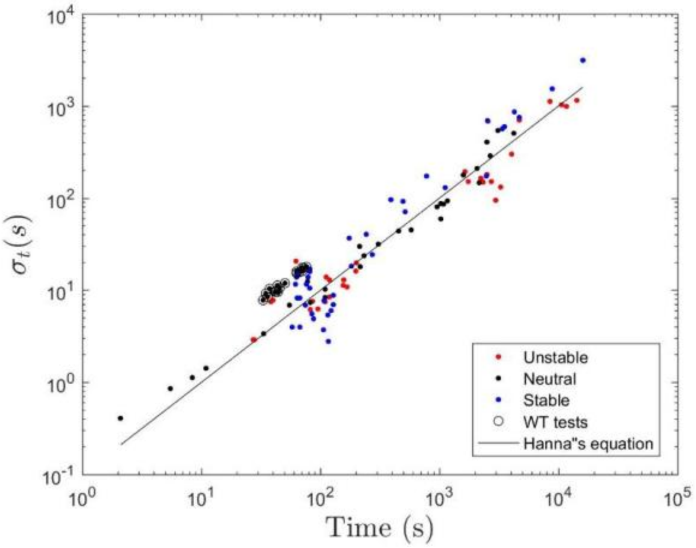

Figure 70. σ_t vs. time for all previous experiments, Hanna's equation, and the new finite-duration releases plotted as a function of stable, unstable, or neutral stability

As expected, the values of σ_t estimated in this program are larger since previous values of σ_t had been estimated using $\sigma_t = (\Delta T - T_{dur})/4.3$. Clearly, the use of ensemble average measurements provide a different perspective on this problem that cannot be obtained from field scale data.

Following the previous discussion, Figure 71 includes data from this experimental program along with previous data. As with Figure 70, the time scale used to represent the data in this work is TOPa.

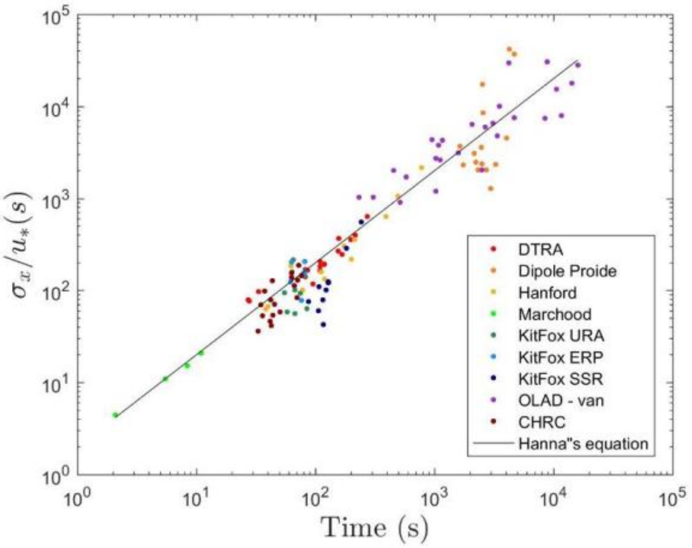

Figure 71. σ_x/u_* vs. time for all previous experiments by tests, Hanna's equation, and the new finite-duration releases (CHRC)

When compared in this fashion, the parameters estimated here are in agreement with past data. It should be noted that none of the CHRC finite-duration data are scaled. Using the Froude number, scaled version of the data from this work compared with previous data are shown in Figure 72.

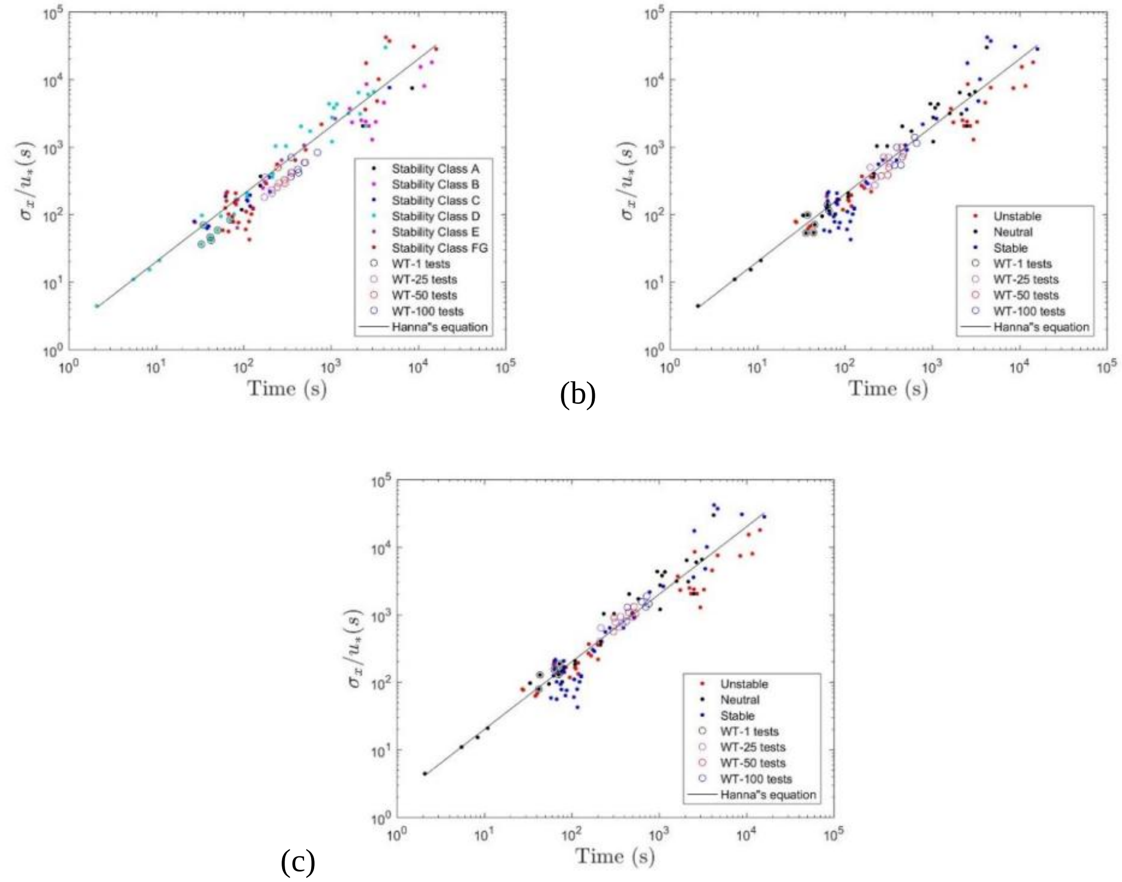

(a) (b)

(c)

Figure 72. σ_x/u_* vs. time for all previous experiments, Hanna's equation, and the new finite-duration releases scaled for 1:1, 1:25, 1:50, and 1:100 ratio by stability class for "near" distances at 2ft and 4ft (a), "middle" distances at 4ft and 8ft (b), and "far" distances at 8ft and 12ft (c) unscaled for 0.35m/s and 0.71m/s respectively

As can be seen in Figure 72, σ_x/u_* values at the "near" measurement locations are less than other σ_x/u_* values reported here. This is likely due to the decrease in the effective wind speed near the source.

3.5.4 Modeling Applications

The ensemble averaged experiments reported here offer the ability to describe along-wind dispersion that cannot be done with previous experimental results. From a modeling perspective, concentration-time histories need to be predicted, not measured. Relationships to predict the time distribution coefficients are discussed for the trailing edge, leading edge, impact of release duration on the leading edge, and total time distribution coefficient.

3.5.4.1 Modeling σ_{td}

In the data, the trailing edge, σ_{td}, was relatively constant for all release durations at the same downwind distance and wind speed. Using the wind speed at the sensor height, u_{1cm}, the trailing edge can be predicted by

$$\boldsymbol{\sigma_{td} = 1.47(\frac{\mathrm{x}}{u_{1cm}})^{0.539}} \tag{80}$$

With this relationship for the trailing edge time distribution coefficient, MG VG values are 0.985 and 1.027, respectively.

3.5.4.2 Modeling σ_{ta} at steady-state

Similar to the trailing edge, there was a trend identified in σ_{ta} for releases that had a maximum concentration consistent with a steady-state release. The σ_{ta} values were relatively constant for all distances downwind for the same wind speeds. For releases reaching steady-state conditions, σ_{ta} can be predicted using

$$\boldsymbol{\sigma_{ta}(SS) = -60.21u_{1cm} + 29.4} \tag{81}$$

The constant -60.21 has units of s^2/m and 29.4 has units of seconds to result in the units of seconds for σ_{ta}. This equation results in MG VG values of 1.002 and 1.005, respectively.

3.5.4.3 Modeling σ_{ta} not at steady-state

Additional short duration tests were performed to determine the impact of release duration on σ_{ta} values when steady-state is not achieved as summarized in Figure 73.

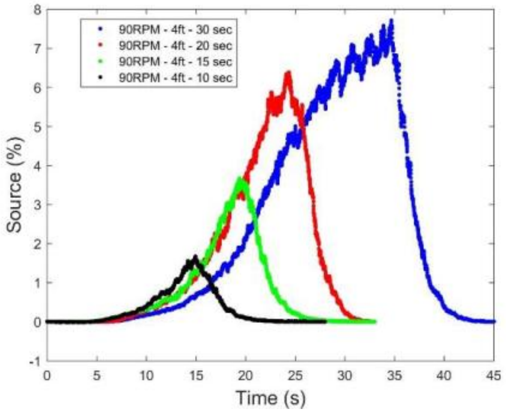

Figure 73. Shortened release durations at 0.71 m/s and 4ft downwind

Figure 73 shows that the release duration importantly influences σ_{ta} values. The 30-second releases and shorter release durations show that as the cloud travels downwind, the leading and trailing edges come together more quickly reducing the maximum (peak) observed concentration. These values are observed in Table 35.

Table 35. Summary of σ_t values for shorter release durations

test	U (m/s)	U_{1cm} (m/s)	u_* (m/s)	Dist. (m)	Dur. (s)	σ_{ta} (s)	σ_{td} (s)	σ_t – total (s)
6	0.71	0.224	0.036	1.37	120	15.58	3.77	9.67
5	0.71	0.224	0.036	1.37	60	16.82	3.12	9.97
8	0.71	0.224	0.036	1.37	30	12.27	3.34	7.81
35	0.71	0.224	0.036	1.37	20	7.70	2.98	5.34
36	0.71	0.224	0.036	1.37	15	6.00	3.08	4.54
34	0.71	0.224	0.036	1.37	10	3.84	2.34	3.09

Expanding on the table are comparisons of the $\sigma_{ta}/\sigma_{ta}\ (SS)$ ratios shown in Figure 74 for short duration releases.

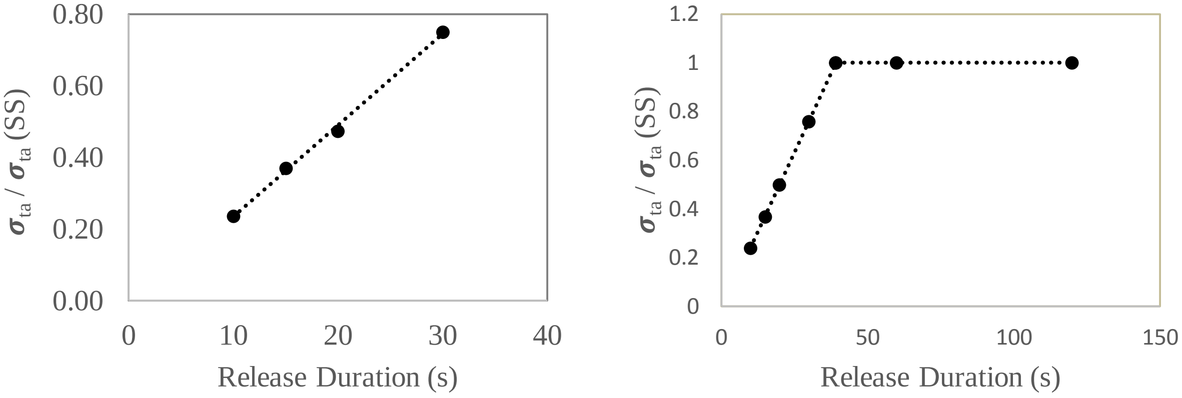

Figure 74. $\sigma_{ta}/\sigma_{ta}\ (SS)$ vs. release duration for shortened tests at 4ft and 0.71 m/s (left) and individual values for $\sigma_{ta}/\sigma_{ta}\ (SS)$ with both models (right)

To model the experimental results for shorter release durations, σ_{ta} can be modeled using

$$\frac{\sigma_{ta}}{\sigma_{ta}(SS)} = 0.0225 * T_{dur} - 0.0201 \qquad T_{dur} < T(SS) \qquad (82)$$

$$\frac{\sigma_{ta}}{\sigma_{ta}(SS)} = 1 \qquad T_{dur} \geq T(SS) \qquad (83)$$

Where $T_{dur}$is the release duration in seconds, *T(SS)* is the duration required to reach steady-state concentrations, and 0.0225 in units of 1/s to non-dimensionalized the equation. While this equation was developed based on a limited number of experiments, it seems to work effectively for the other conditions tested here.

3.5.4.4 Total σ_t

The models for σ_{ta} and σ_{td} can be combined assuming a single Gaussian distribution as would be expected for long travel time or distance.

$$\boldsymbol{\sigma_t = \frac{(\sigma_{ta} + \sigma_{td})}{2}} \tag{84}$$

Where values of σ_{ta} and σ_{td} are found using equations (80), (81), and (82). Figure 75 shows a parity plot of predicted values compared with observed values.

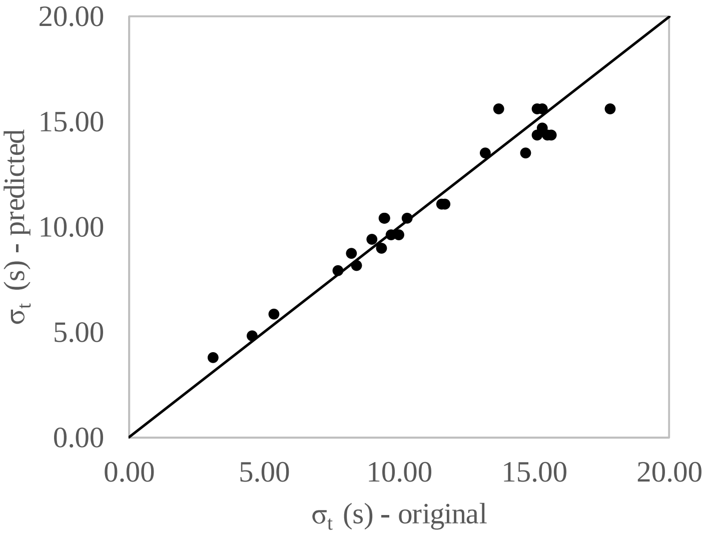

Figure 75. Parity plot of predicted σ_t values in comparison with data

For all release durations including the non-steady-state releases, MG VG values were 1.000 and 1.005 respectively.

3.5.4.5 Relation of Wind Tunnel Tests to Field Tests

While the experimental program was performed in a wind tunnel, the results and relationships are directly applicable to field tests. From the additional tests performed, the shorter the finite-duration release results in a decreased concentration, TOPa, and smaller time distribution coefficient. The same effect would be expected for field scale tests. This observation is seen with advanced similarity models. The two main relationships that can be used when scaling are the $\sigma_t = 0.23 * TOPa$ and $TOPa = C_1 * {T_{dur}}^p * (\frac{u_e}{u})^q$. The other relationships developed for the time distribution coefficient can also be scaled to be applied for appropriate wind speeds with Froude number scaling.

3.6 Conclusions

Finite-duration releases were performed in an ultra-low speed wind tunnel at the Chemical Hazards Research Center. The majority of the test program focused on area source release with durations of 30-, 60-, and 120-seconds. Tests were conducted at wind speeds of 0.35 m/s and 0.71 m/s (at freestream) at downwind distances of (nominally) 2 ft, 4 ft, 8ft, and 12 ft. Ensemble averages of at least 65 tests were performed for each set of test conditions. Previous assumptions for determining the time distribution coefficient from field data may be open to question. Across all wind speeds, distances, and release durations, $\sigma_t = 0.23 * TOPa$. From a modeling perspective, the time distribution coefficient can be reasonably predicted for finite-duration releases that both reach steady-state and for release durations that do not. For the along-wind dispersion coefficient, the experimental results did not provide a simple relationship but can be determined from the total time distribution coefficient and effective wind speed. Overall, throughout the course of the Ph.D.: 1) true finite-duration releases from a purpose-built area source were accomplished, 2) quality data to be used in validation of models under multiple test conditions were established, 3) a method to predict overall σ_t and impact of release durations was determined and 5) an accurate prediction for σ_x from σ_t was accomplished which was the main goal of the Ph.D.

Appendicies

Appendix A. Velocity Profiles – 90RPM (1 layer of spires)

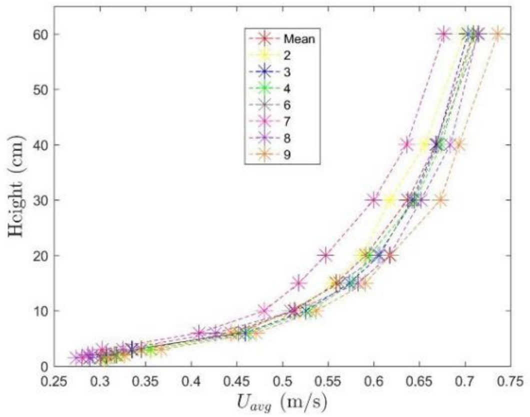

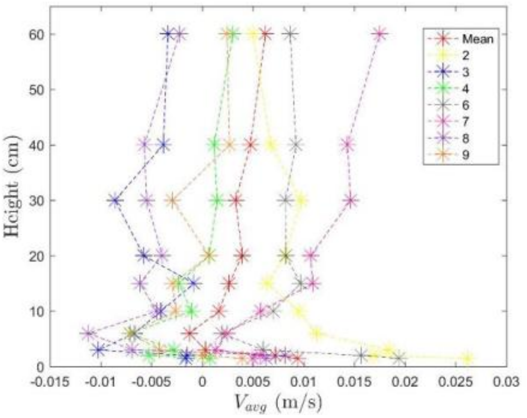

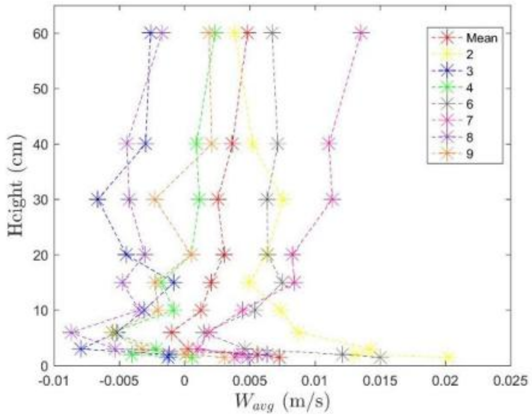

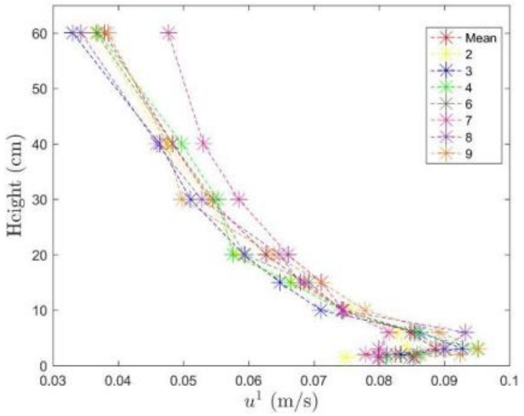

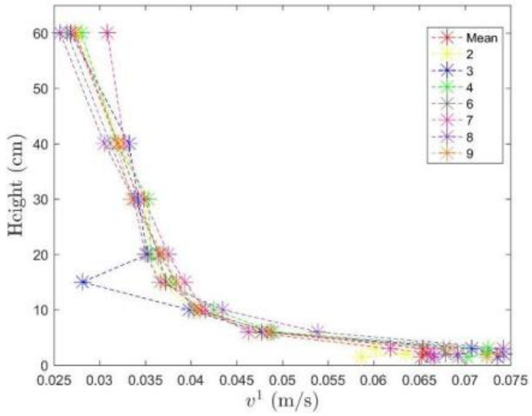

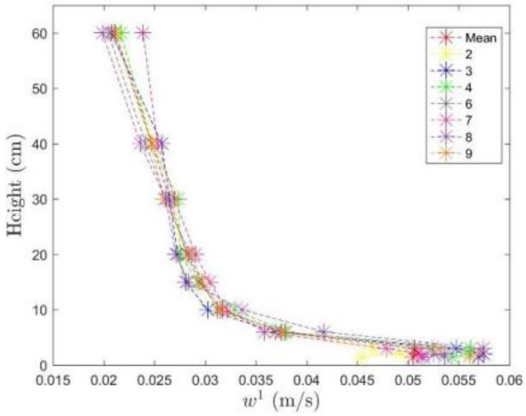

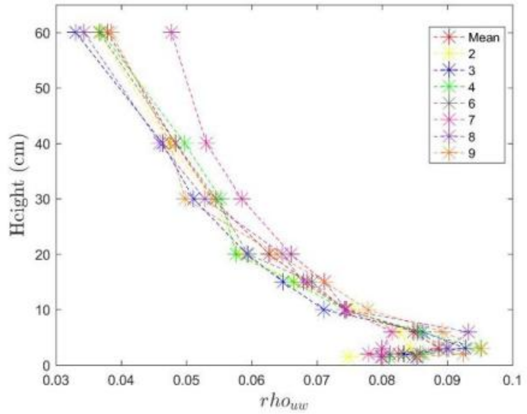
Height (cm)
0
10
20
30
40
50
60
0.03
0.04
0.05
0.06
0.07
0.08
0.09
0.1
rho_{uw}
Mean
2
3
4
6
7
8
9

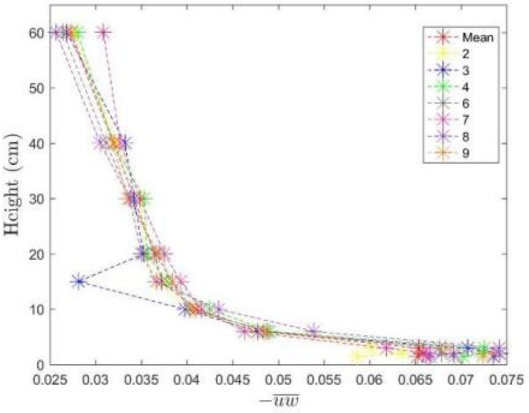
Height (cm)
0
10
20
30
40
50
60
0.025
0.03
0.035
0.04
0.045
0.05
0.055
0.06
0.065
0.07
0.075
$-\overline{uw}$
Mean
2
3
4
6
7
8
9

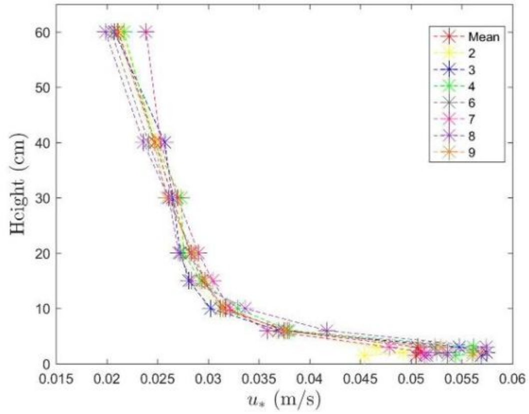
Height (cm)
0
10
20
30
40
50
60
0.015
0.02
0.025
0.03
0.035
0.04
0.045
0.05
0.055
0.06
u_* (m/s)
Mean
2
3
4
6
7
8
9

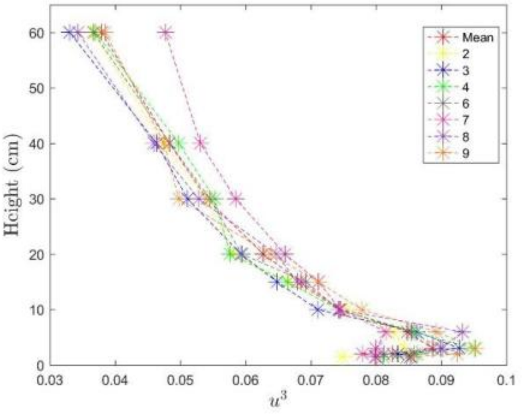
Height (cm)
0
10
20
30
40
50
60
0.03
0.04
0.05
0.06
0.07
0.08
0.09
0.1
u^3
Mean
2
3
4
6
7
8
9

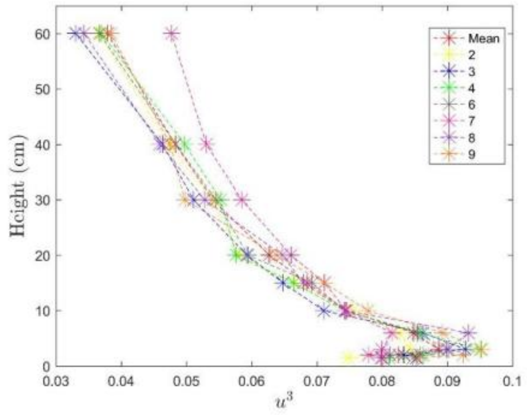
Height (cm)
0
10
20
30
40
50
60
0.03
0.04
0.05
0.06
0.07
0.08
0.09
0.1
u^3
Mean
2
3
4
6
7
8
9

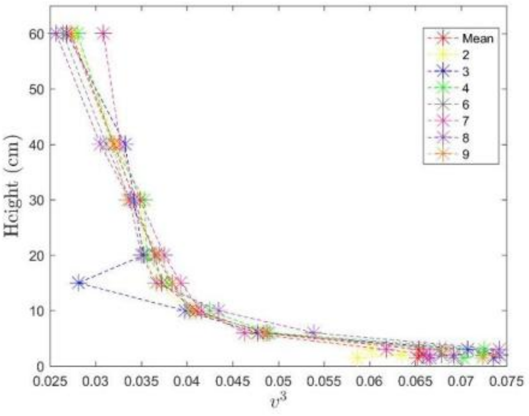
Height (cm)
0
10
20
30
40
50
60
0.025
0.03
0.035
0.04
0.045
0.05
0.055
0.06
0.065
0.07
0.075
v^3
Mean
2
3
4
6
7
8
9

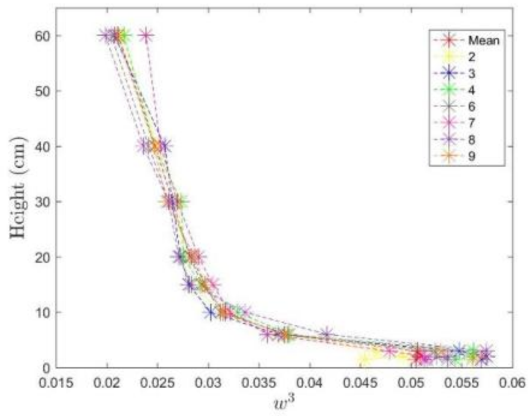

Height (cm)
0
10
20
30
40
50
60
0.015
0.02
0.025
0.03
0.035
0.04
0.045
0.05
0.055
0.06
w^3
Mean
2
3
4
6
7
8
9

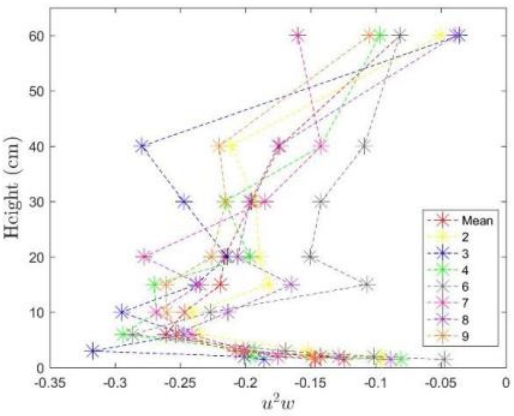

Height (cm)
0
10
20
30
40
50
60
-0.35
-0.3
-0.25
-0.2
-0.15
-0.1
-0.05
0
u^2w
Mean
2
3
4
6
7
8
9

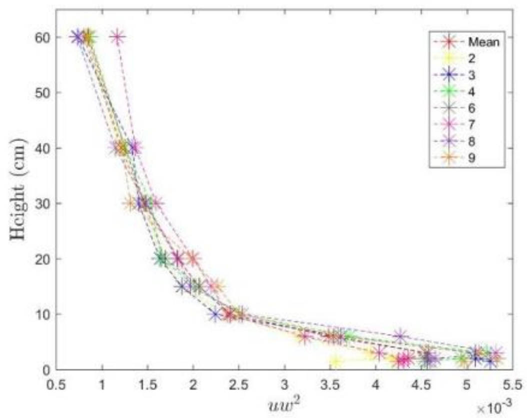

Height (cm)
0
10
20
30
40
50
60
0.5
1
1.5
2
2.5
3
3.5
4
4.5
5
5.5
$\times 10^{-3}$
uw^2
Mean
2
3
4
6
7
8
9

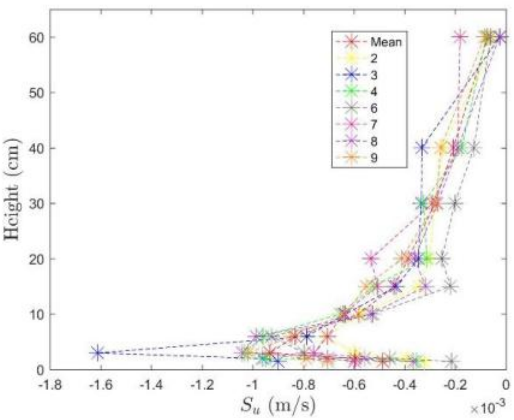

Height (cm)
0
10
20
30
40
50
60
-1.8
-1.6
-1.4
-1.2
-1
-0.8
-0.6
-0.4
-0.2
0
$\times 10^{-3}$
S_u (m/s)
Mean
2
3
4
6
7
8
9

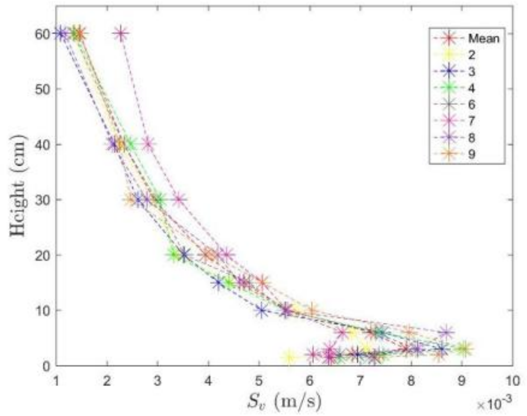

Height (cm)
0
10
20
30
40
50
60
1
2
3
4
5
6
7
8
9
10
$\times 10^{-3}$
S_v (m/s)
Mean
2
3
4
6
7
8
9

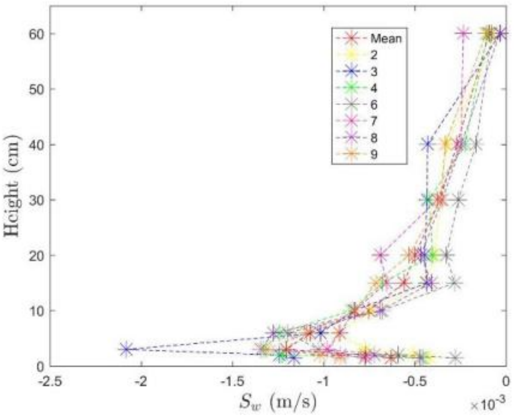

Height (cm)
0
10
20
30
40
50
60
-2.5
-2
-1.5
-1
-0.5
0
$\times 10^{-3}$
S_w (m/s)
Mean
2
3
4
6
7
8
9

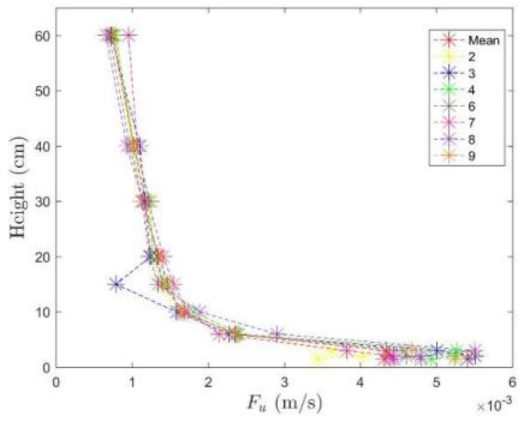
Height (cm)
0
10
20
30
40
50
60
0
1
2
3
4
5
6
$\times 10^{-3}$
F_u (m/s)
Mean
2
3
4
6
7
8
9

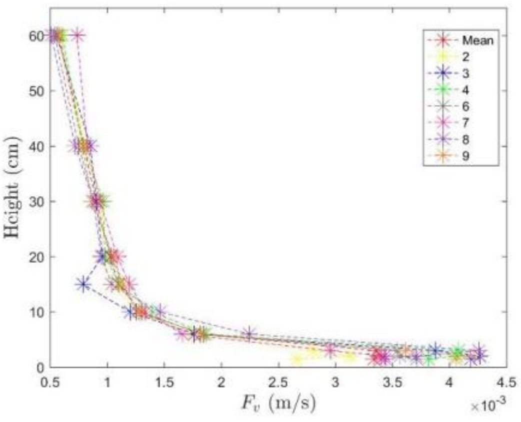
Height (cm)
0
10
20
30
40
50
60
0.5
1
1.5
2
2.5
3
3.5
4
4.5
$\times 10^{-3}$
F_v (m/s)
Mean
2
3
4
6
7
8
9

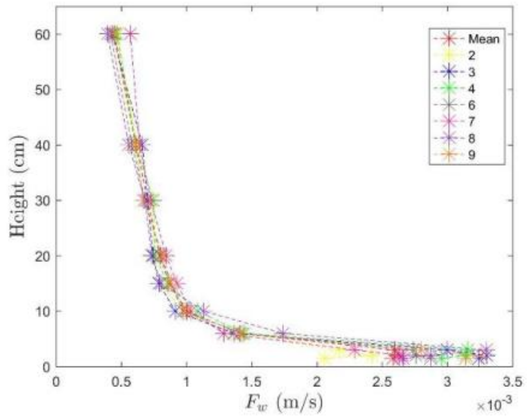
Height (cm)
0
10
20
30
40
50
60
0
0.5
1
1.5
2
2.5
3
3.5
$\times 10^{-3}$
F_w (m/s)
Mean
2
3
4
6
7
8
9

Appendix B. Velocity Profiles – 50RPM – 0.35m/s (2 layers of spires and roughness)

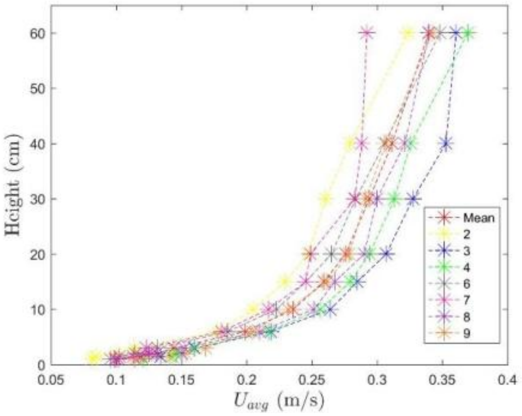

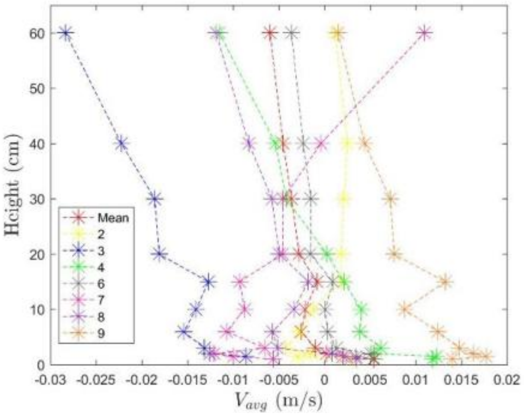

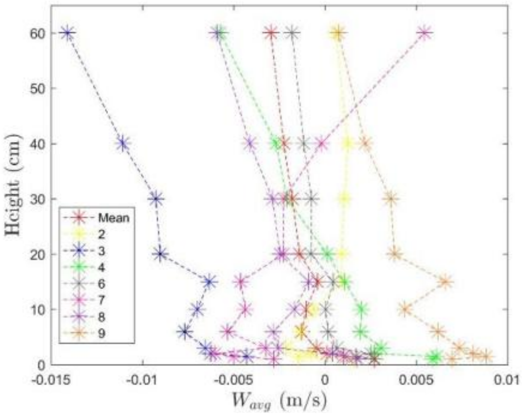

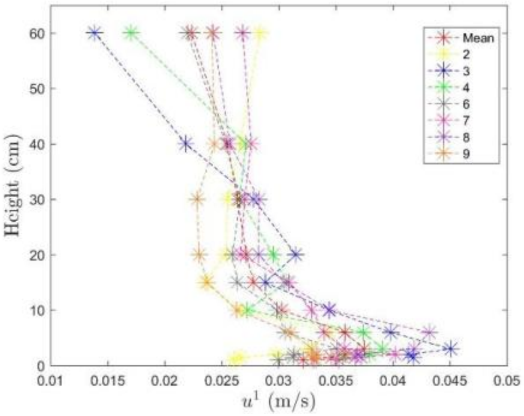

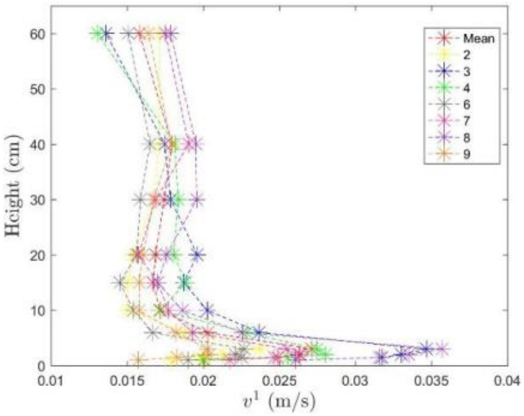

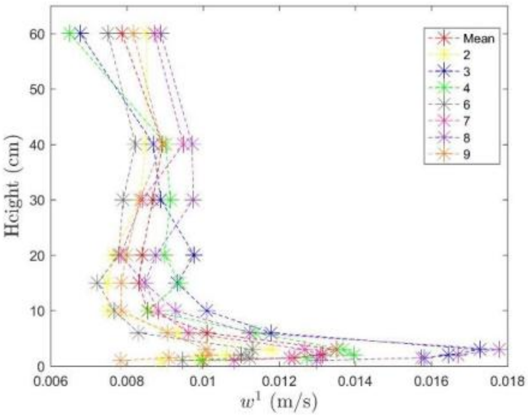

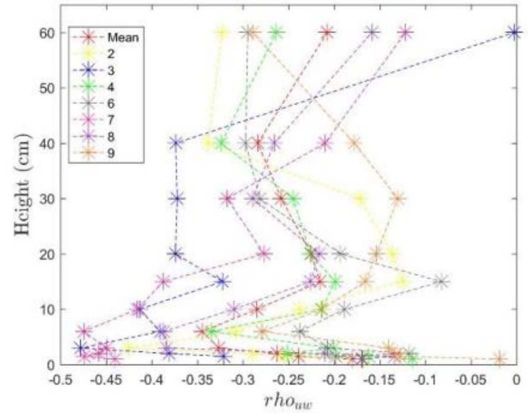
Mean
2
3
4
6
7
8
9
Height (cm)
rho_{uw}
-0.5 -0.45 -0.4 -0.35 -0.3 -0.25 -0.2 -0.15 -0.1 -0.05 0
0 10 20 30 40 50 60

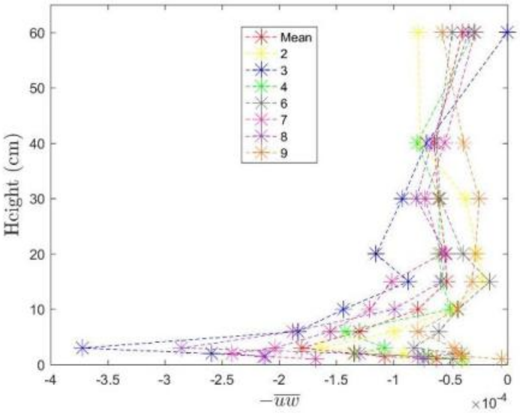
Mean
2
3
4
6
7
8
9
Height (cm)
$-\overline{uw}$
-4 -3.5 -3 -2.5 -2 -1.5 -1 -0.5 0
$\times 10^{-4}$
0 10 20 30 40 50 60

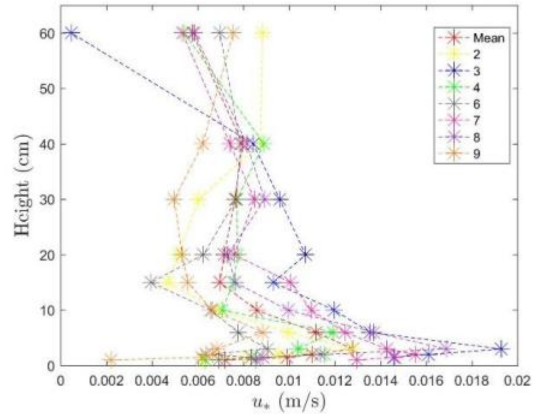
Mean
2
3
4
6
7
8
9
Height (cm)
u_* (m/s)
0 0.002 0.004 0.006 0.008 0.01 0.012 0.014 0.016 0.018 0.02
0 10 20 30 40 50 60

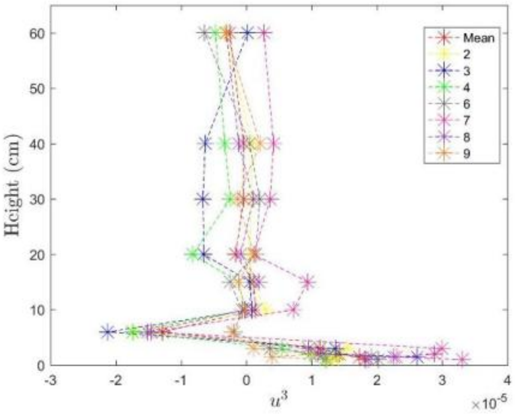
Mean
2
3
4
6
7
8
9
Height (cm)
u^3
-3 -2 -1 0 1 2 3 4
$\times 10^{-5}$
0 10 20 30 40 50 60

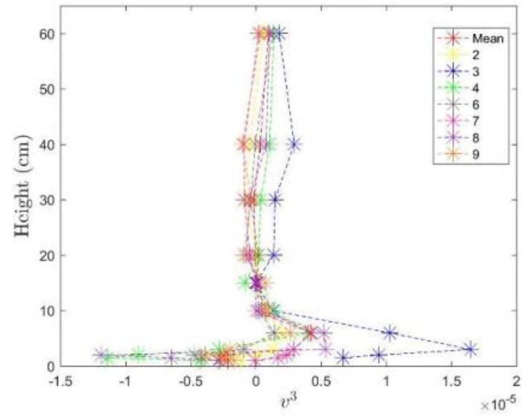
Mean
2
3
4
6
7
8
9
Height (cm)
v^3
-1.5 -1 -0.5 0 0.5 1 1.5 2
$\times 10^{-5}$
0 10 20 30 40 50 60

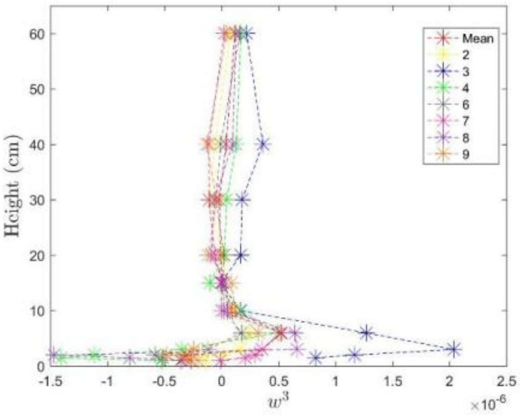
Mean
2
3
4
6
7
8
9
Height (cm)
w^3
-1.5 -1 -0.5 0 0.5 1 1.5 2 2.5
$\times 10^{-6}$
0 10 20 30 40 50 60

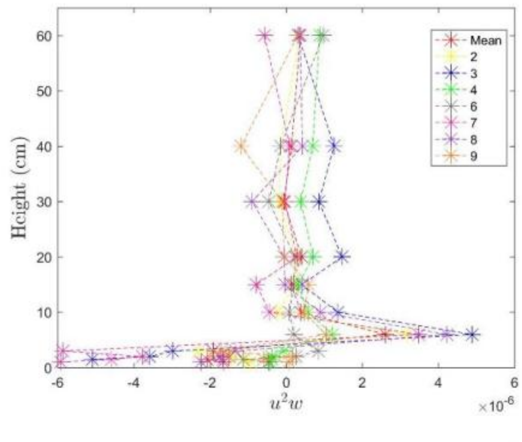
Height (cm)
u^2w
$\times 10^{-6}$
Mean
2
3
4
6
7
8
9

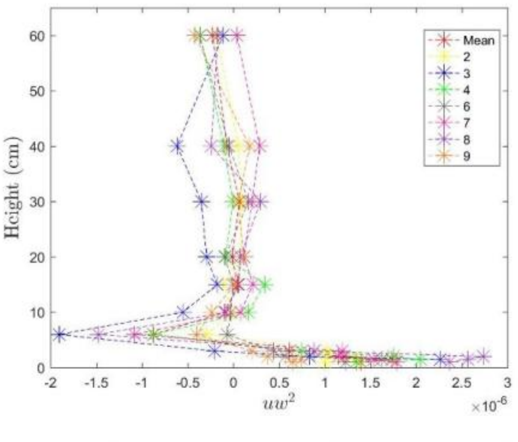
Height (cm)
uw^2
$\times 10^{-6}$
Mean
2
3
4
6
7
8
9

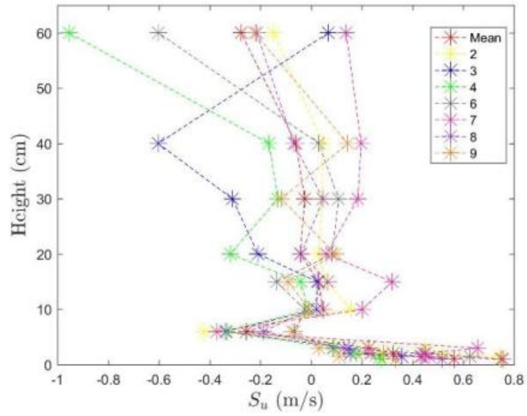
Height (cm)
S_u (m/s)
Mean
2
3
4
6
7
8
9

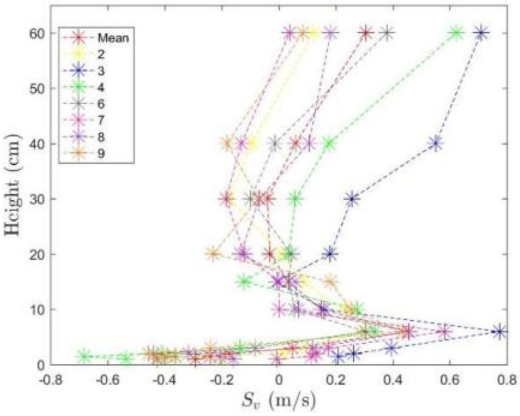
Height (cm)
S_v (m/s)
Mean
2
3
4
6
7
8
9

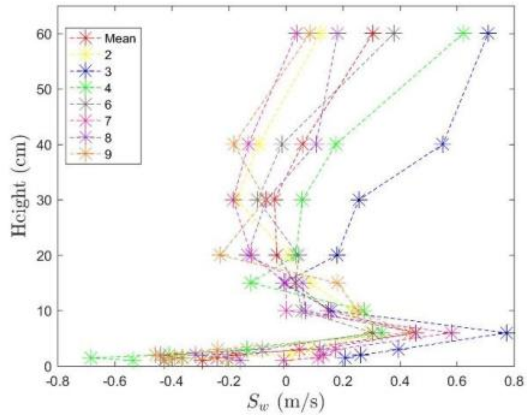
Height (cm)
S_w (m/s)
Mean
2
3
4
6
7
8
9

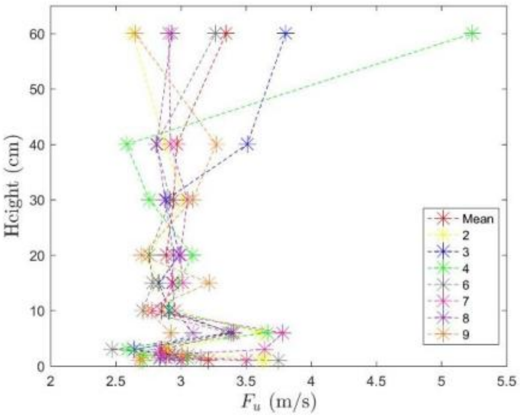
Height (cm)
F_u (m/s)
Mean
2
3
4
6
7
8
9

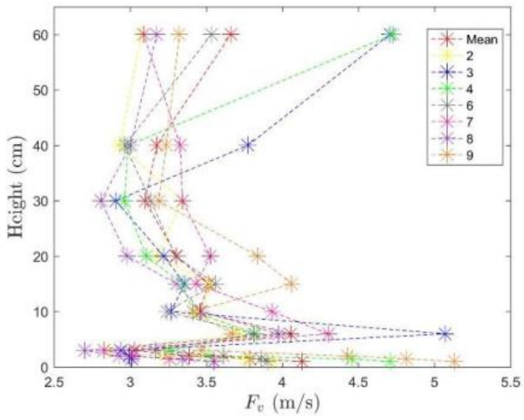
Height (cm)
0
10
20
30
40
50
60
2.5
3
3.5
4
4.5
5
5.5
F_v (m/s)
Mean
2
3
4
6
7
8
9

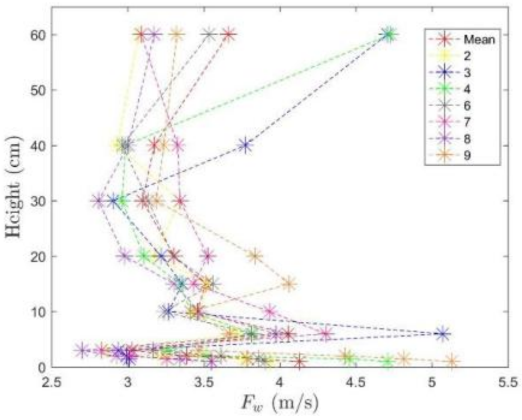
Height (cm)
0
10
20
30
40
50
60
2.5
3
3.5
4
4.5
5
5.5
F_w (m/s)
Mean
2
3
4
6
7
8
9

Appendix C. Individual Tests

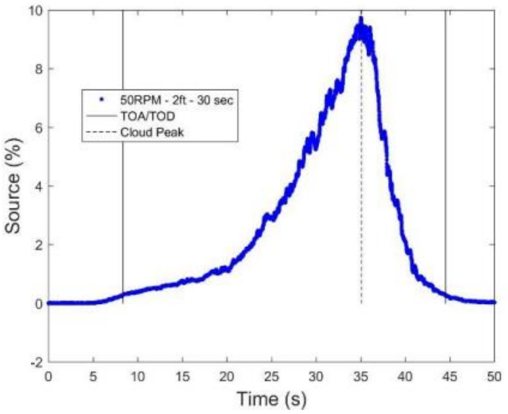

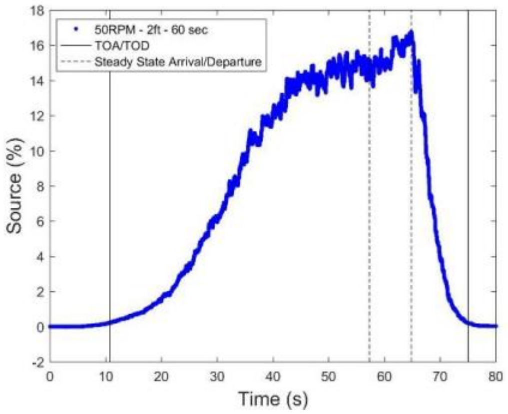

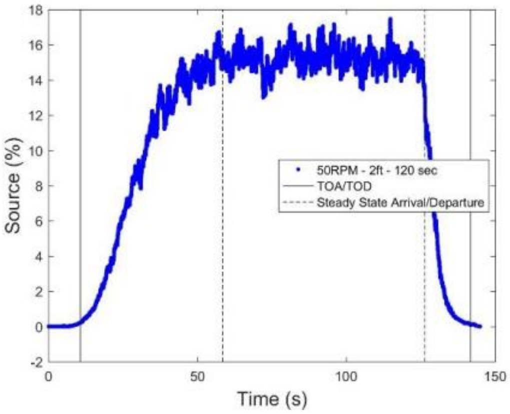

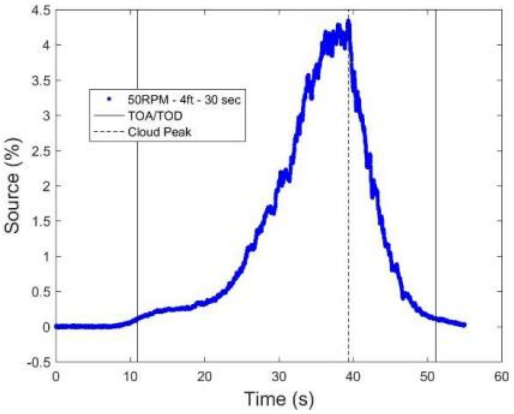

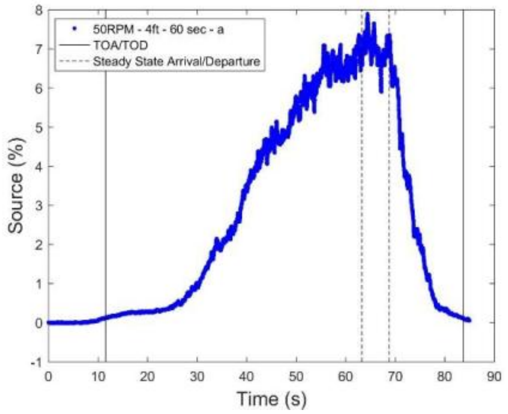

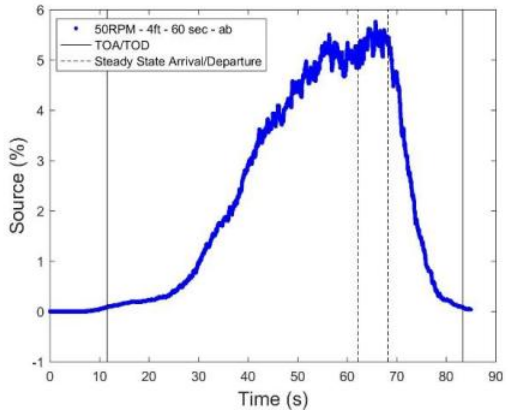

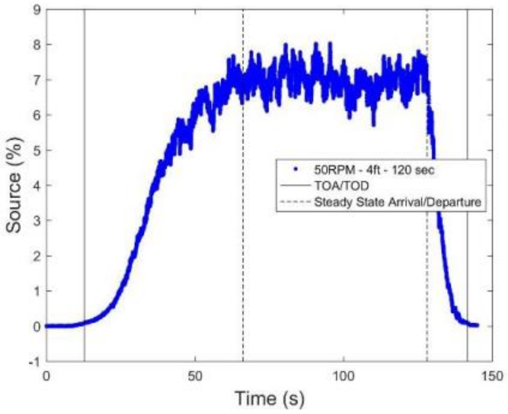
50RPM - 4ft - 120 sec
TOA/TOD
Steady State Arrival/Departure
Source (%)
Time (s)
-1
0
1
2
3
4
5
6
7
8
9
0
50
100
150

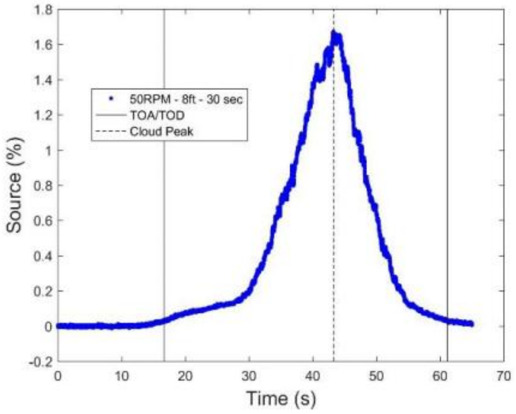
50RPM - 8ft - 30 sec
TOA/TOD
Cloud Peak
Source (%)
Time (s)
-0.2
0
0.2
0.4
0.6
0.8
1
1.2
1.4
1.6
1.8
0
10
20
30
40
50
60
70

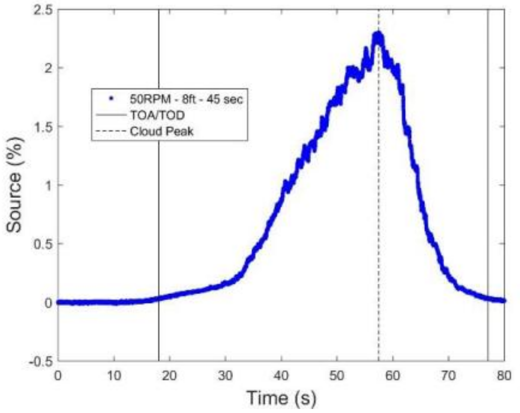
50RPM - 8ft - 45 sec
TOA/TOD
Cloud Peak
Source (%)
Time (s)
-0.5
0
0.5
1
1.5
2
2.5
0
10
20
30
40
50
60
70
80

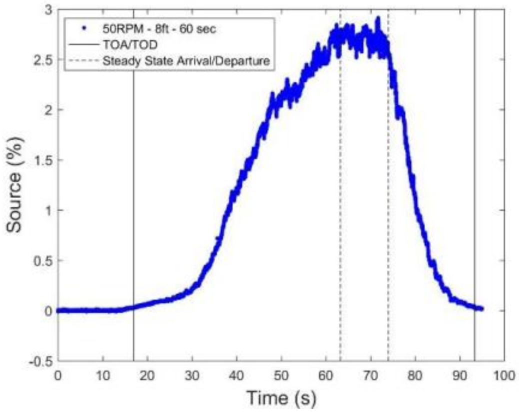
50RPM - 8ft - 60 sec
TOA/TOD
Steady State Arrival/Departure
Source (%)
Time (s)
-0.5
0
0.5
1
1.5
2
2.5
3
0
10
20
30
40
50
60
70
80
90
100

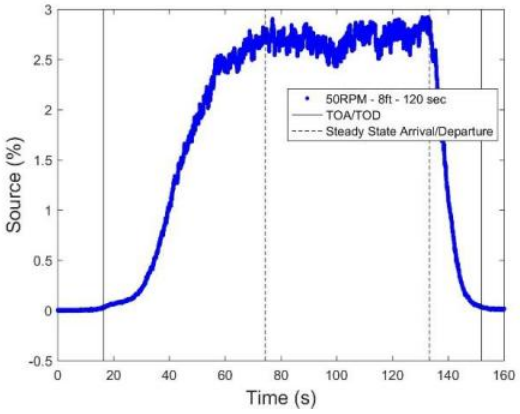
50RPM - 8ft - 120 sec
TOA/TOD
Steady State Arrival/Departure
Source (%)
Time (s)
-0.5
0
0.5
1
1.5
2
2.5
3
0
20
40
60
80
100
120
140
160

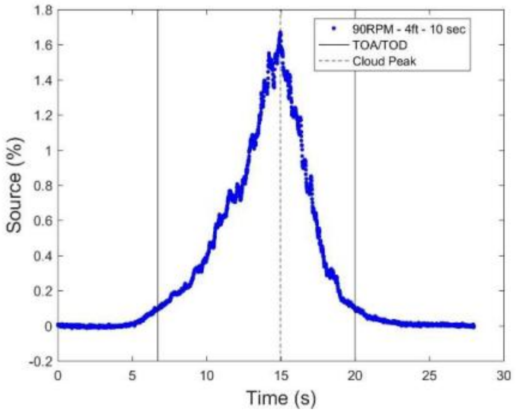
90RPM - 4ft - 10 sec
TOA/TOD
Cloud Peak
Source (%)
Time (s)
-0.2
0
0.2
0.4
0.6
0.8
1
1.2
1.4
1.6
1.8
0
5
10
15
20
25
30

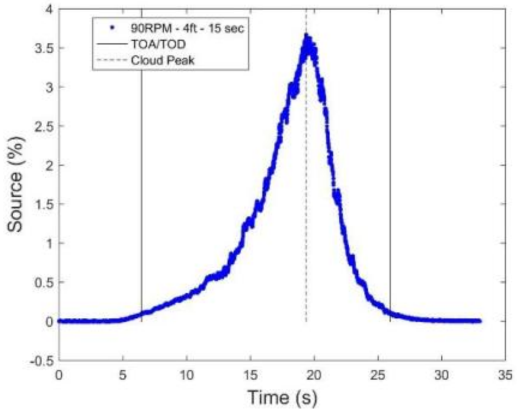
90RPM - 4ft - 15 sec
TOA/TOD
Cloud Peak
Source (%)
Time (s)
-0.5
0
0.5
1
1.5
2
2.5
3
3.5
4
0
5
10
15
20
25
30
35

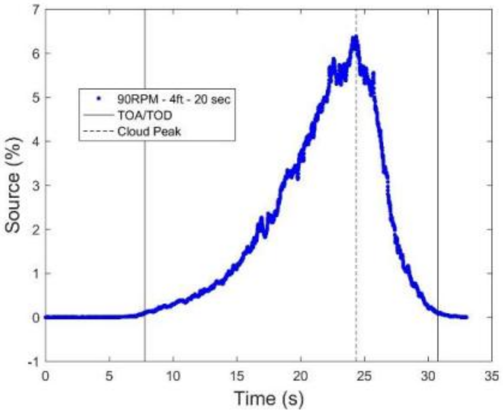
90RPM - 4ft - 20 sec
TOA/TOD
Cloud Peak
Source (%)
Time (s)
-1
0
1
2
3
4
5
6
7
0
5
10
15
20
25
30
35

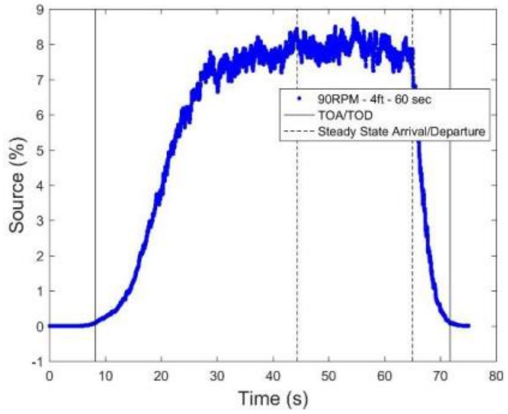
90RPM - 4ft - 60 sec
TOA/TOD
Steady State Arrival/Departure
Source (%)
Time (s)
-1
0
1
2
3
4
5
6
7
8
9
0
10
20
30
40
50
60
70
80

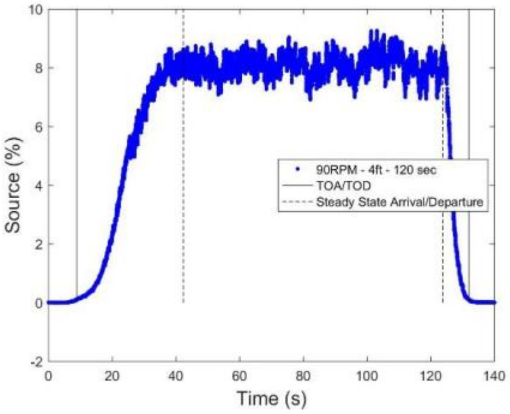
90RPM - 4ft - 120 sec
TOA/TOD
Steady State Arrival/Departure
Source (%)
Time (s)
-2
0
2
4
6
8
10
0
20
40
60
80
100
120
140

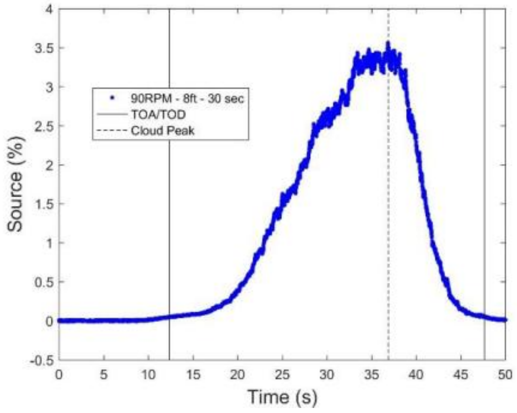
90RPM - 8ft - 30 sec
TOA/TOD
Cloud Peak
Source (%)
Time (s)
-0.5
0
0.5
1
1.5
2
2.5
3
3.5
4
0
5
10
15
20
25
30
35
40
45
50

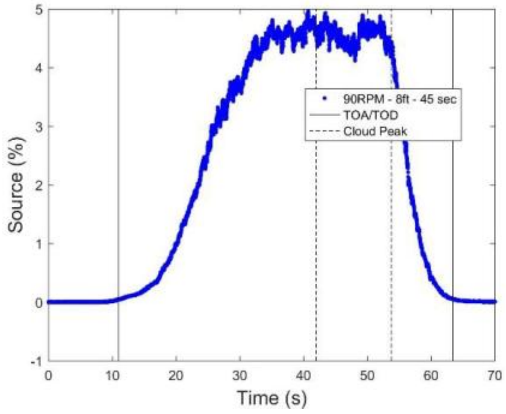
90RPM - 8ft - 45 sec
TOA/TOD
Cloud Peak
Source (%)
Time (s)
-1
0
1
2
3
4
5
0
10
20
30
40
50
60
70

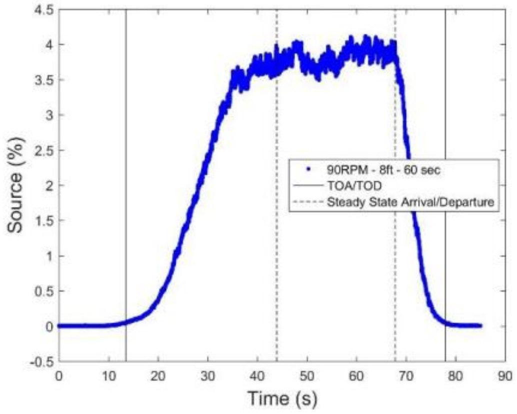
90RPM - 8ft - 60 sec
TOA/TOD
Steady State Arrival/Departure
Source (%)
Time (s)
-0.5
0
0.5
1
1.5
2
2.5
3
3.5
4
4.5
0
10
20
30
40
50
60
70
80
90

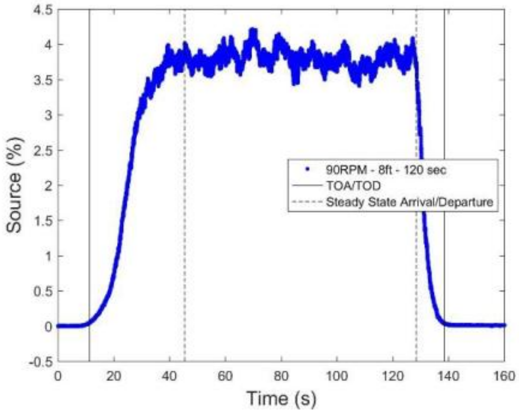
90RPM - 8ft - 120 sec
TOA/TOD
Steady State Arrival/Departure
Source (%)
Time (s)
-0.5
0
0.5
1
1.5
2
2.5
3
3.5
4
4.5
0
20
40
60
80
100
120
140
160

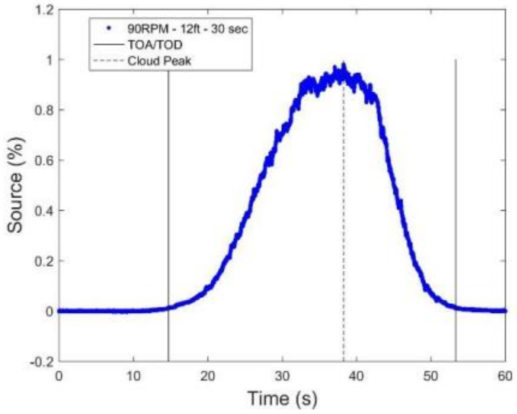
90RPM - 12ft - 30 sec
TOA/TOD
Cloud Peak
Source (%)
Time (s)
-0.2
0
0.2
0.4
0.6
0.8
1
1.2
0
10
20
30
40
50
60

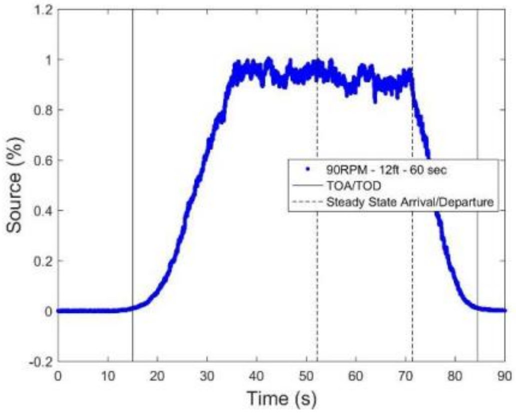
90RPM - 12ft - 60 sec
TOA/TOD
Steady State Arrival/Departure
Source (%)
Time (s)
-0.2
0
0.2
0.4
0.6
0.8
1
1.2
0
10
20
30
40
50
60
70
80
90

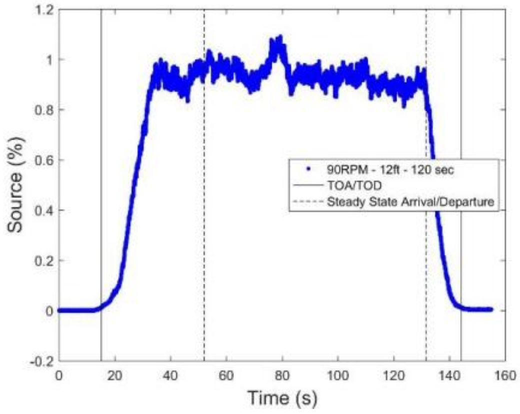
90RPM - 12ft - 120 sec
TOA/TOD
Steady State Arrival/Departure
Source (%)
Time (s)
-0.2
0
0.2
0.4
0.6
0.8
1
1.2
0
20
40
60
80
100
120
140
160

Appendix D. Finite-Duration Releases grouped by Distance

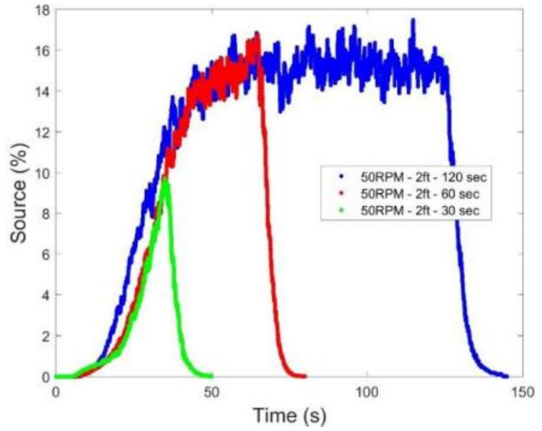

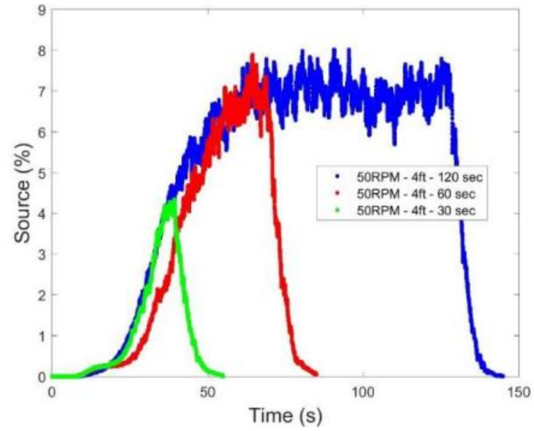

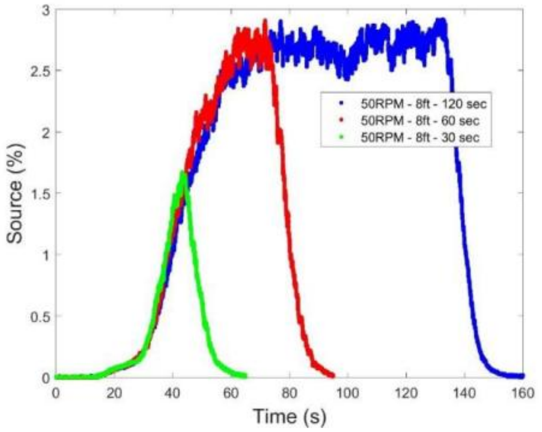

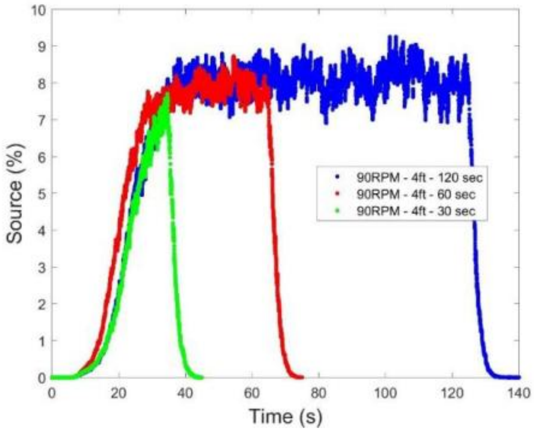

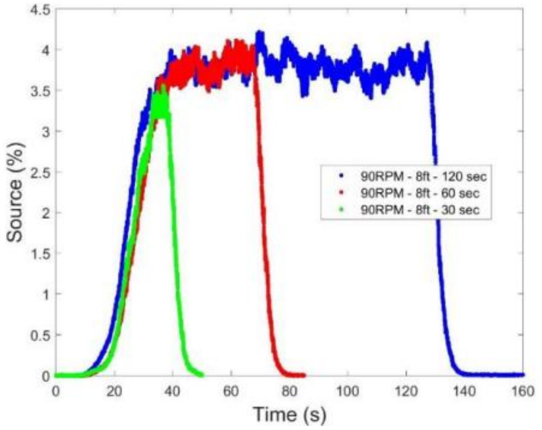

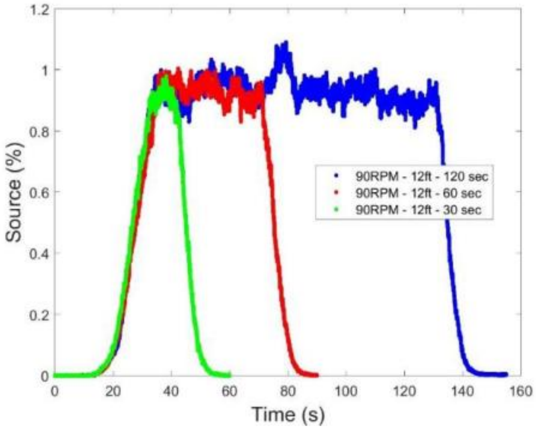

Appendix E.   Finite-Duration Releases grouped by Release Duration

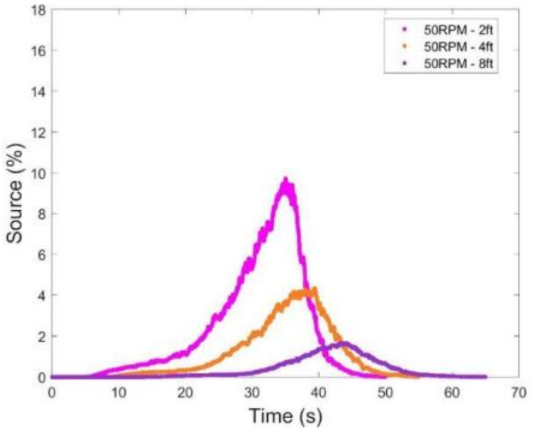

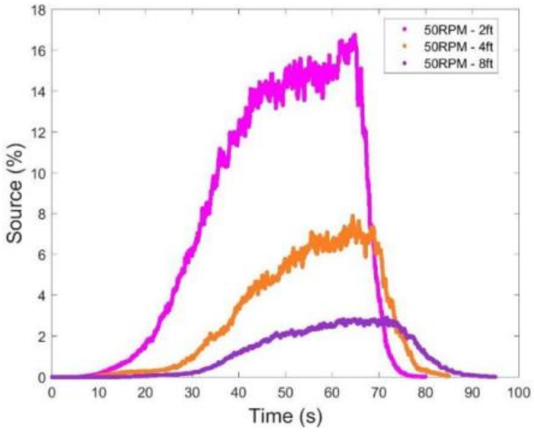

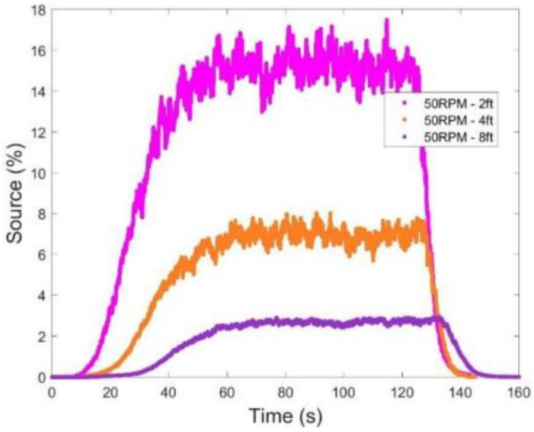

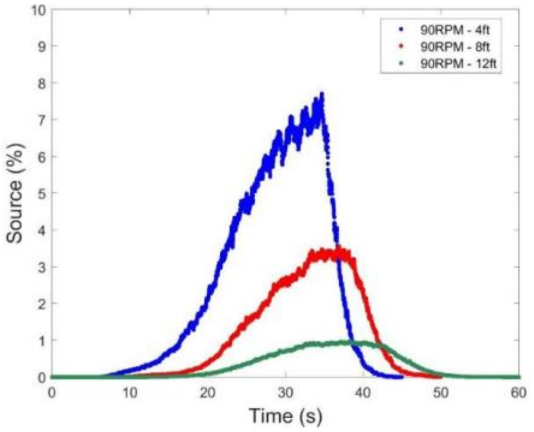

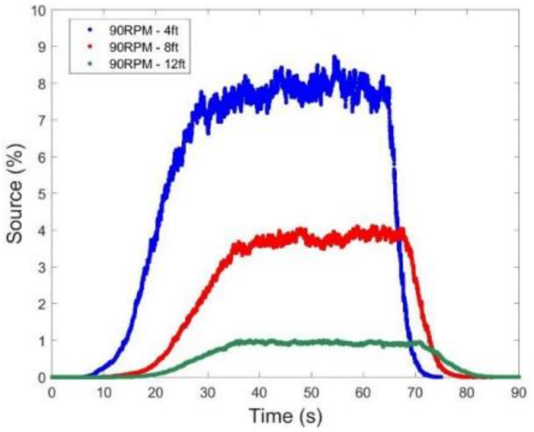

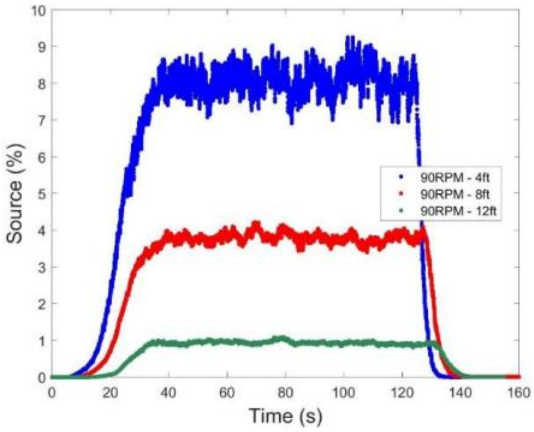

References

---

[1] Boybeyi, Zafer, Sethu Raman, and Paolo Zannetti. "Numerical investigation of possible role of local meteorology in Bhopal gas accident." *Atmospheric Environment* 29.4 (1995): 479-496.

[2] Høiset, S., et al. "Flixborough revisited—an explosion simulation approach." *Journal of hazardous materials* 77.1 (2000): 1-9.

[3] De Marchi, Bruna, Silvio Funtowicz, and Jerome Ravetz. "Seveso: A paradoxical classic disaster." *The long road to recovery: Community responses to industrial disaster* (1996): 86-120.

[4] Sheesley, D. et al. 1998. Chemical Dispersion Modeling Project, 1995 Kit Fox Field Demonstration DOE Nevada Hazardous Spill Center. Volume I – Experiment Description and Data Processing.

[5] King, S. Bruce. 1999. The Kit Fox Field Demonstration Project and Data Set. *International Conference and Workshop on Modeling the Consequences of Accidental Releases of Hazardous Materials.*

[6] Parker, Roger J. “The Flixborough Disaster. Report of the Court of Inquiry.” Department of Employment. Her Majesty’s Stationary Office, London (1975).

[7] Zhang, Wei, et al. "Effects of wall suction/blowing on two-dimensional flow past a confined square cylinder." *SpringerPlus* 5.1 (2016): 985.

[8] Hanna, S.R., and Chang, J.C., “Analysis of dispersion of finite-duration releases of dense gases and recommended revisions to HEGADAS, Earth Tech Report 1411, 196 Baker Ave, Concord, MA01742, 196 Baker Ave, Concord, MA01742, prepared for Exxon Research and Engineering, 180 Park Ave, Florham Park, NJ07932 (1995)

[9] Petersen, R.L., Wind tunnel and HEGADAS simulations of finite duration releases for a specific refinery with uniform roughness, CPP Report 91-9782, 1992

[10] Taylor, Geoffrey. "Dispersion of soluble matter in solvent flowing slowly through a tube." *Proceedings of the Royal Society of London A: Mathematical, Physical and Engineering Sciences*. Vol. 219. No. 1137. The Royal Society, 1953.

[11] Csanady, G. T. "Diffusion in an Ekman layer." *Journal of the Atmospheric Sciences* 26.3 (1969): 414-426.

[12] Saffman, P. G. "The effect of wind shear on horizontal spread from an instantaneous ground source." *Quarterly Journal of the Royal Meteorological Society* 88.378 (1962): 382-393.

[13] Batchelor, G. K. "Diffusion from sources in a turbulent boundary layer." *Arch. Mech. Stosow* 3.6 (1964): 661-670.

---

[14] Chatwin, P. C. "The dispersion of a puff of passive contaminant in the constant stress region." *Quarterly Journal of the Royal Meteorological Society* 94.401 (1968): 350-360.

[15] Wilson, D. J. "Along-wind diffusion of source transients." *Atmospheric Environment (1967)* 15.4 (1981): 489-495.

[16] Smith, F. B. "The role of wind shear in horizontal diffusion of ambient particles." *Quarterly Journal of the Royal Meteorological Society* 91.389 (1965): 318-329.

[17] Ermak. D. L., "Unpublished notes on downwind spreading formulation in finite-duration release version of SLAB", Lawrence Livermore National Laboratory, California (1986).

[18] McMullen, Robert W. "The change of concentration standard deviations with distance." *Journal of the Air Pollution Control Association* 25.10 (1975): 1057-1058.

[19] Van Ulden, A. P. "A surface-layer similarity model for the dispersion of a skewed passive puff near the ground." *Atmospheric Environment. Part A. General Topics* 26.4 (1992): 681-692.

[20] Hanna, Steven R., and Pasquale Franzese. "Alongwind Dispersion-A Simple Similarity Formula Compared with Observations at 11 Field Sites and in One Wind Tunnel." *Journal of Applied Meteorology* 39.10 (2000): 1700-1714.

[21] Drivas, Peter J., and Fredrick H. Shair. "Dispersion of an instantaneous cross-wind line source of tracer released from an urban highway." *Atmospheric Environment (1967)* 8.5 (1974): 475-485.

[22] Draxler, R. R. "Some observations of the along-wind dispersion parameter." *Symposium on Turbulence, Diffusion, and Air Pollution, 4th, Reno, Nev, Preprints, Research supported by the U. S. Department of Energy*. Vol. 15. No. 18. 1979.

[23] Smith, F. B., and J. S. Hay. "The expansion of clusters of particles in the atmosphere." *Quarterly Journal of the Royal Meteorological Society* 87.371 (1961): 82-101.

[24] Sato, J., 1995: An analytical study on longitudinal diffusion in the atmospheric boundary layer. *Geophys. Mag. Ser. 2,*1, 105–15

[25] Robins, A. G., and J. E. Fackrell. "An experimental study of the dispersion of short duration emissions in a turbulent boundary layer." *WIT Transactions on Ecology and the Environment* 28 (1970).

[26] Biltoft, C., Phase I of DSWA transport and dispersion model validation study. DPG-FR-97-058, (1997): 156.

[27] Biltoft, C., Dipole Pride 26: Phase II of DSWA transport and dispersion model validation study. DPG-FR-98-001, (1998): 130.

---

[28] Watson, T. B, R. E. Keislar, B. Reese, D. H. George, and C. A. Biltoft, The DSWA Dipole Pride 26 field experiment. NOAA Tech. Memo. ERL ARL-225, (1998): 99.

[29] King, S. Bruce. The Kit Fox Field Demonstration Project and Data Set. *International Conference and Workshop on Modeling the Consequences of Accidental Releases of Hazardous Materials.* (1999).

[30] Spicer, T. and Havens, J. Description and Analysis of Atmospheric Dispersion Tests Conducted by EPA. *International Conference and Workshop on Modeling the Consequences of Accidental Releases of Hazardous Materials.* (1999).

[31] Sheesley, D. et al.. Chemical Dispersion Modeling Project, 1995 Kit Fox Field Demonstration DOE Nevada Hazardous Spill Center. Volume I – Experiment Description and Data Processing. (1998).

[32] Hanna, S. R., and K. W. Steinberg, Studies of dense gas dispersion from short-duration transient releases over rough surfaces during stable conditions. *Air Pollution Modeling and Its Applications XI,*Plenum Press, (1996): 481–490.

[33] Nickola, P. W., J. D. Ludwick, and J. V. Ramsdell Jr., An inert gas tracer system for monitoring the real-time history of a diffusing plume or puff. *J. Appl. Meteor.,*9, (1970): 621–626.

[34] Bowers, J. F., G. E. Start, R. G. Carter, T. B. Watson, K. L. Clawson, and T. L. Crawford, Experimental design and results for the Long-Range Overwater Diffusion (LROD) Experiment. DPG/JCP-94/012, (1994): 531.

[35] Biltoft, C., S. D. Turley, T. B. Watson, G. H. Crescenti, and R. G. Carter, Over-Land Atmospheric Dispersion (OLAD) test summary and analysis. WDTC Doc. WDTC/JCP-99/048, (1999): 38.

[36] Smith, and B. L. Niemann, Shoreline diffusion program, Oceanside, CA. Vols. I and II. MRI-64-FR-860, (1969): 230 and 456.

[37] Hilst, G. R., and N. E. Bowne, A study of the diffusion of aerosols released from aerial line sources upwind of an urban complex. Vols. I and II. Rep. DA-42-007-AMC-38®, (1966): 231 and 583.

[38] Sato, J., F. Kimura, and T. Yoshikawa, The longitudinal spread of puff in the short range diffusion experiment. *Pap. Meteor. Geophys.,*32, (1981): 155–162.

[39] Golder, Donald. "Relations among stability parameters in the surface layer." *Boundary-Layer Meteorology* 3.1 (1972): 47-58.

[40] Davis, Richard A. “Practical Numerical Methods for Chemical Engineers: Using Excel with VBA”. Lexington, KY, (2015).

---

[41] Draper, Norman Richard, Harry Smith, and Elizabeth Pownell. *Applied regression analysis*. Vol. 3. New York: Wiley, (1966).

[42] Conover, William Jay, and William Jay Conover. "Practical nonparametric statistics." (1980).

[43] Hanna, S. R., J. C. Chang, and D. G. Strimaitis. "Hazardous gas model evaluation with field observations." *Atmospheric Environment. Part A. General Topics* 27.15 (1993): 2265-2285.

[44] DNV GL. DNV GL Theory Manual for Unified Dispersion Model. London UK 2015.

[45] Wilson, David J. *Concentration fluctuations and averaging time in vapor clouds*. John Wiley & Sons, 2010.

[46] Havens, J., and T. Spicer. "Vapor dispersion and thermal hazard modelling." *Final topical report to Gas Technology Institute under sub-contract K* 100029184 (2006).

[47] Walker, H., and J. Havens. "Comparison of hot wire and laser Doppler anemometry measurements of the turbulence structure of an ultra low speed wind tunnel boundary layer." *Data report, Chemical Hazards Research Center,* University of Arkansas, Fayetteville, AR 72701 (1998).

[48] Irwin, H. P. A. H. "The design of spires for wind simulation." *Journal of Wind Engineering and Industrial Aerodynamics*7.3 (1981): 361-366.

[49] Cambustion. "Fast FID Principles." Exhaust Gas Recirculation (EGR), NOx and Particulate Measurement | Cambustion, 2018, www.cambustion.com/products/hfr500/fast-fid-principles.

[50] GadgetReview. " An illustration of a VOC meter detecting pollutants in the surrounding air" How do VOC Meters Work? | GadgetReview, 2018, http://www.gadgetreview.com/what-is-voc-Meter

[51] Koflo. "KD-981" Koflo, 2018, https://www.koflo.com/drawings/pdf/kd-981.pdf

[52] "Weber Number" Engineering Toolbox, 2018, https://www.engineeringtoolbox.com/weber-number-d_583.html

[53] Havens, Jerry, Heather Walker, and Thomas O. Spicer. "Wind tunnel study of air entrainment into two-dimensional dense gas plumes at the Chemical Hazards Research Center." *Atmospheric Environment* 35.13 (2001): 2305-2317.

[54] Wieslander, Gunillla, D. Norback, and Torsten Lindgren. "Experimental exposure to propylene glycol mist in aviation emergency training: acute oculat and respiratory effects." *Occupational and Environmental* Medicine 58.19 (2001): 649-655.

[55] TSI. (2005). Phase Doppler Particle Analyzer (PDPA) / Laser Dopppler Velocimeter (LDV) Operations Manual. *Shoreview, MN.*

---

[56] Mathieu J., Scott J., 2000. An Introduction to Turbulent Flow. Cambridge University Press, Cambridge, UK.

[57] C. G. Lomas, Fundamentals of Hot Wire Anemometry. Cambridge University Press, 2011.

[58] "Measurement Techniques for Instantaneous Velocity", Emaze – amazing presentations. [Online]. Available: https://www.emaze.com/@ALORRLQI/TP-PRESENTATiON

[59] Stull, B. R., 1988. An Introduction to Boundary Layer Meterology. Boston: Kluwer Academic Publishers.

[60] C. V. Mashuga and D. A. Crowl, "Application of the Flammability Diagram for Evaluation of Fire and Explosion Hazards of Flammable Vapors," *Process Safety Progress* (1998), 17(3): 176.

[61] Wilson, David J. Concentration fluctuations and averaging time in vapor clouds. John Wiley & Sons, 2010. Pg 42.

[62] Hall, D. J., et al. "The Effect of Release Time on the Dispersion of a Fixed Inventory of Heavy Gas – A Wind Tunnel Model Study." Physmod 2007.

[63] Hall, D., R. Waters, and G. Marsland, Repeat variability in instantaneously release heavy gas clouds – some wind tunnel model experiments. 1991.

[64] Wilson, David J. Concentration fluctuations and averaging time in vapor clouds. John Wiley & Sons, 2010. Pg 43.

[65] Hanna, Steven R., and Joseph C. Chang. "Use of the Kit Fox field data to analyze dense gas dispersion modeling dispersion modeling issues." *Atmospheric Environment.* 35.13 (2001): 2231-2242.

[66] Hanna, S.R., Chang, J.C., 1995. Analysis of dispersion of finite duration releases of dense gases and recommended revisions to HEGADAS. Earth Tech. Report No. 1411, prepared for Exxon Research and Engineering, 180 Park Ave., Florham Park, NJ 07932.